Doctoral Dissertation
Doctoral Program in Materials Science and Technology (35rd Cycle)

Development of AlSi10Mg based alloys for Additive Manufacturing Processes

By

Fabrizio Marinucci

****

Supervisor(s):
Prof. F. Bondioli, Supervisor
Prof. D. Manfredi, Co-Supervisor

Doctoral Examination Committee:
Dr. Herranz G. , Referee, University of Castilla-La Mancha
Dr. Lupoi R. , Referee, University of Dublin - Trinity College

Politecnico di Torino 2022

Declaration

I hereby declare that, the contents and organization of this dissertation constitute my own original work and does not compromise in any way the rights of third parties, including those relating to the security of personal data.

Fabrizio Marinucci

2022

* This dissertation is presented in partial fulfillment of the requirements for **Ph.D. degree** in the Graduate School of Politecnico di Torino (ScuDo).

Acknowledgement

I would like to acknowledge my supervisor Prof. Federica Bondioli and my co-supervisor Prof. Diego Manfredi for giving me the excellent opportunity to work in such an innovative field. I will always remember their guidance, patience and support.

I would also like to express my gratitude to Prof. Mariangela Lombardi and Dr. Alberta Aversa. With their advice and help, I could grow as a student and researcher during these years, building the skills that will help me in my future career.

A special thanks go to Christian Wissing Kruse and Dr. Mandanà Moshiri for hosting me in the LEGO group. The knowledge I acquired during the months spent in the MAM team were highly precious to my job experience.

I am really grateful for this journey in Politecnico as a PhD student because it allowed me to meet the most important person in my life, my girlfriend, Hanieh. I want to thank her for all the time she spent with me, cheering me up in the difficult moments and enjoying with me the happy ones.

And finally, I want to acknowledge my family and friends, that constantly supported me during this journey. I am fortunate to have them in my life.

Abstract

Additive manufacturing (AM) technology has been rapidly widespread in research and industrial fields during the last decade. The success of this technology is the possibility to produce complex shaped components starting from a 3D model, avoiding successive machining steps, in opposition to the traditional subtractive techniques.

The AM technology includes several production processes divided by specific characteristics of the technique used, kind of material and kind of feedstock. In particular, considering the metal as raw material, the most common feedstock is in powder form, which can be used in different AM processes. The powders must have specific characteristics to satisfy the requirements of AM techniques, such as spherical shape, controlled particle size distribution (PSD) and low impurities.

In order to produce a powder that fulfils the AM requirements, the most common process is atomization. Between the various atomization technologies, the market is led by gas atomization. The gas atomization technique ensures powers with a spherical shape, a correct PSD and reasonable control of the contaminant, with a relatively low price compared with other techniques. Mass production costs are significantly decreased since a considerable amount of powders can be produced during a single atomization. However, a massive powder batch can be costly for research purposes such as the study of new compositions. For this reason, the use of laboratory-scale gas atomizers represents the best choice since it allows to produce smaller batches of powders with complete freedom in the design of the final composition of the alloy. In addition, reduced-scale atomization can allow better control in the process with consequent benefits in the powders characteristics.

After powder production, one of the most common AM techniques to produce bulk components is Laser Powder Bed Fusion (LPBF). This technique involves different process parameters in building the components, such as laser power, scan speed and hatching distance. Several methods were developed to achieve the optimization of process parameters in order to achieve the best properties of the final components. Among them, the single scan track (SST) method represents a time and material-saving test, which defines the best process parameters window. However, some critical points of this method require improvements. In addition, the final properties,

such as densification, microstructure and mechanical resistance, are tested on the bulk samples.

Finally, after the optimization of the process and the achievement of fully dense components with good mechanical properties, several studies involved the improvement of the characteristics of the samples. The most common way is to define a specific heat treatment route, but some alternative ways are rapidly catching on, involving the modification of the initial composition of the alloy.

This PhD thesis focuses on a specific alloy for LPBF production, which is AlSi10Mg. This alloy has been demonstrated to be a perfect candidate for AM due to its high processability, good mechanical properties, and corrosion resistance of the final components.

This thesis covers the entire AM process, starting from powder production with a laboratory-scale gas atomizer and comparing the self-produced powder with a commercial-grade counterpart. It follows a description of process parameters optimization, where the main focus is posed on the SST technique, proposing a new method to improve this kind of analysis and solve the critical points. After that, the comparison between the powders is extended to the bulk sample properties produced by LPBF. Finally, new compositions of AlSi10Mg with modifying elements are proposed to improve the mechanical properties in the as-built state.

Contents

List of Figures

List of Tables

Overview and Preface

The development of new technologies is the main engine towards new frontiers and discoveries. In the human history the technology upgraded the man's life, opening the door to new possibilities and opportunities. Often a new technology requires new materials, switching from the traditional sources to the need to purchase new sources, which were unknown or not used yet. This happened several times in the human history. For instance, the transition from stone age, where all the tools were made smashing and refining rocks, to the bronze age, where the metallurgy was born, caused a sudden need to extract metals in substitution of the stone. The discovery of the gunpowder, which switched the need of the war industry from the wood used to fabricate bows and arrows, to this new terrible compound, able to destroy the huge city walls which were inviolable before. More recently, the industrial revolution and the rise of the fuel oil based, substituted progressively the vapor engines and machines, making the transport easier and faster. These are all examples of technological discoveries, where materials played a key role.

The metallurgy improved significantly from the already cited bronze age, when the alloying of the metals was only based on the experience and empirical considerations. Nowadays, many disparate techniques to transform metals and to produce every kind of components exist. The techniques can be very different based on the metal's physical and chemical properties. Casting, joining, injection molding, plastic deformation are only some examples of the so called "conventional processes" to produce metallic components.

New needs, such as the limitation of the wastes and the possibility to avoid different steps of production, leaded to the development of 3D printing processes. These technologies, applied to different family of materials including metals, allow to produce component starting from a 3D model, without the need of post-processing step. Basically, it is the technology of the future which allow to reduce the long sequence of industrial scale traditional processes to few steps of production, applicable to small scale machines, entering in the daily life of everyone. In addition, a technology which allows to avoid several refining steps is able also to contain the waste of raw material, since in the starting design no additional material for production process constraint is required.

3D printing is now better known as Additive Manufacturing (AM), since it is distinguished from the traditional subtractive technique. The world of AM includes several techniques for each material family. The interest around metal Additive Manufacturing is rapidly increasing due to the possibility to apply it in several fields such as aerospace, biomedical, automotive etc. As happened in the past, the new technology requires new materials. In fact, the portfolio of materials available for AM is still not comparable to the one at disposal of traditional technologies. An improvement in this direction is very important to expand the potential of AM in covering the need for every kind of application.

The aim of this thesis is to give a complete overview of a process which belongs to AM family, starting from the production of the raw material, up to the manufacturing of the components. Following each step of the process, a procedure is defined in order to study new alloys and their processability, with the aim of extend the materials available. The thesis is structured as follows:

- **Chapter 1: State of art.** In this chapter an overview of Additive Manufacturing is given with the description of its main characteristics and techniques. The discussion starts with an analysis of the advantages and drawbacks of AM respect the traditional techniques and a classification of all the AM process. It follows a description of the production technology of raw materials, with the focus in gas atomization. Finally, the main AM processes are described with focusing especially on laser powder bed fusion and aluminum alloys, which are the main subject of this thesis.

- **Chapter 2: Materials and methods.** Here are described the materials and the methodologies adopted for the samples characterization, with a description of the process and the instruments used.

- **Chapter 3: Powder production and characterization.** The third chapter is entirely dedicated to the powder production and the powder analysis, in order to understand the main powder characteristics that define a good powder for AM. Here, a complete overview on the gas atomization process and on all the characterization necessary before using the powder in the AM machines is given.

- **Chapter 4: Process parameters optimization.** This chapter represents the last step before the production of the final components. Here the technique used to detect the best AM process parameters are described. These

techniques include the evaluation of the relative density, the microstructure and the mechanical properties.

- **Chapter 5: Modifiers elements in AlSi10Mg.** In the fifth and final chapter some methods to improve the properties of LPBF components, via slight changes in the alloys compositions are proposed. This chapter is a preliminary study aiming to detect the possibility of improving the properties of AlSi10Mg by adjusting its chemical composition.

Chapter 1

State of art

1.1 Additive manufacturing

Additive Manufacturing (AM) technologies include several production techniques based on different starting materials. The main advantage of these technologies is the possibility to produce complex shaped components with a significant freedom of design [1]. AM is a near-net shape technology and therefore further manufacturing steps such as machining and joining can be avoided. Even if AM is a more expensive technology rather than the traditional ones, the potential money saving due to the avoid of post-process shaping steps decreases the final price of the components. That's why the advantage of using AM technology rather than traditional techniques must be evaluated in term of complexity of the final component and manufacturing costs [2](Figure 1).

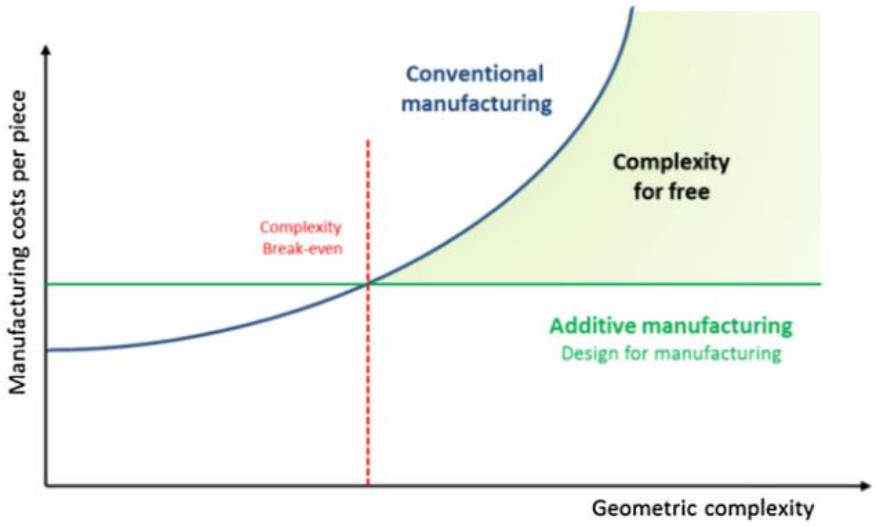

Figure 1: Complexity for free in AM [2] .

The first application of AM processes in the industrial field was prototyping. The success of AM for this purpose is due to the simplicity of production in short-time complex shapes, which is a handy feature in this sense. In fact, in the 1980s, the technology was known as Rapid Prototyping (RP), and it was advantageous for the engineers to produce prototypes starting from a computer-aided design (CAD) model without tooling operation [3]. Nowadays, the tendency is to produce final functional products for end users in small-medium quantities [4].

In general, a complete process of AM can be divided into eight main steps, schematically represented in Figure 2[5]:

- **CAD file creation;** the first step is creating a CAD file of the component to produce. The AM manufacturing techniques need a model to describe the geometry to reproduce fully. It can be done using any professional CAD solid modelling. Reverse engineering techniques, for instance, laser scanning, can also be used to achieve the 3D model of an existing component.

- **Conversion to STL**; the CAD file has to be converted in STL (standard tessellation language), which is the standard format accepted by the AM machines. The STL file is an unordered collection of triangular surfaces. These surfaces have associated an average vector which describes their direction. When the geometry is complex and highly discontinuous, the

result triangles vertices may not align correctly, leading to gaps in the surface. Mostly, these gaps can be bridged automatically when the AM machine processes the file, but in some cases, additional, unwanted material could be included in the final component. Sometimes the automatic correction is not enough, and manual intervention is required.

- **Transfer to AM machine and STL file manipulation;** after the STL file creation and its eventual correction, the file is sent to the AM machine software which has a tool to visualize the STL files and manipulate them. Here the user can choose the parts position on the building platform and their orientation. In this step also supports can be added. The supports are structure built between the platform and the component, which allow to dissipate the heat, enhance the adhesion to the platform and make easier the successive removal operations.

- **Machine Setup;** all machines have at least some setup parameters specific to that machine or process. Depending on the machine the setup parameter can cover the process of few materials or several materials. Some machines give the possibility to freely choose the process parameters and to try all the combination in order to improve the suitability of the process. In general, if the setup of the parameters is chosen incorrectly, the results would not necessarily be the job failure, but the final quality of the component can be compromised. In addition, the operator must check that the material feedstock is enough to cover the entire job.

- **Build;** the initial steps of any AM process are the most critical ones, so manual operations and controls are required. Once the build set-up phase is completed the process switches to a computer-controlled building phase. If no errors are detected during the process the machine will keep going until the component is built.

- **Cleanup and removal;** in general, as the component is built the first operation to perform is to clean it from the raw material residues. After that, the component must be separated from the building platform. Whenever it is possible, the components can be built up with supports at the interface with the building platform. The supports are easy to remove, allowing an easy separation too. To perform the removal operation several techniques may be used such as wire EDM (electro discharging machine), bandsaw or

cutting machines. This operation requires a degree of operator skills since the part can be damaged.

- **Post-Processing;** this step is strongly application and AM process specific. Different AM techniques have in fact different results in terms of geometrical accuracy, and thus the final post-processing operation can involve a machining step to reach the final dimensions. Furthermore, some applications require a certain surface finishing. In these cases post processing steps such as abrasive finishing, polishing or sandpapering can be performed. Moreover, in other cases, the component requires a coating or a heat treatment in order to achieve the final properties.

- **Application;** after the post-processing steps the component is ready to be used. As previously reported, the applications of AM components are several in different fields such as aerospace, medical, automotive etc.

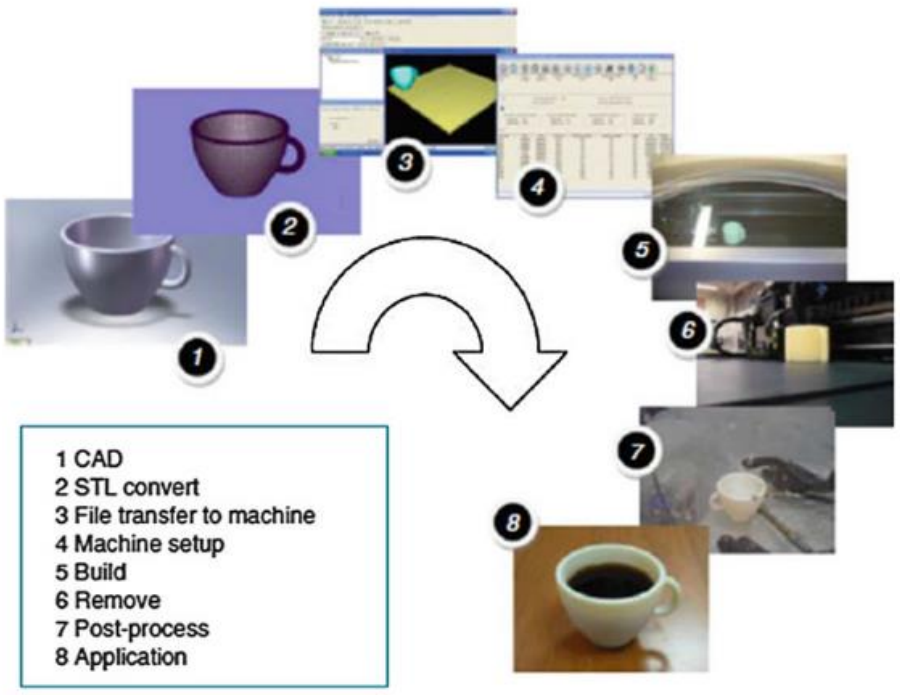

Figure 2: The eight stages of AM processes [5].

The standards to classify the AM techniques were at first established in 2009, by the American Society for Testing and Materials (ASTM). The classification is

based on eight methods according to the ASTM F2792 (2012) [6]. In **Table 1**, the main AM processes are classified and briefly described [7]. Direct energy deposition (DED), powder bed fusion (PBF), binder jetting, sheet lamination and cold spraying are the techniques suitable for the metal production, which is the main focus of this PhD thesis. However, nowadays, only DED and PBF processes are effective enough to manufacture components with high reliability and robustness [8]. The main feedstock of these techniques is metal powder, with strict characteristics. A more detailed description of the AM techniques will take place in the next pages after an overview of the powder production technology.

Table 1: AM techniques classification [7].

3D printing process	Description	Utility in metal AM
Material extrusion	Material is extruded through a heated nozzle	–
Material jetting	Deposition of build material droplets by an inkjet print head	–
Binder jetting	Deposition of liquid bonding agent droplets to a powder bed	✓
Sheet lamination	Sheets of material are bonded to form an object	✓
Vat photopolymerization	Selective curing of liquid photopolymer using light activated polymerization	–
Powder bed fusion (PBF)	Selective thermal fusion of powder bed using a laser or an electron beam	✓
Directed energy deposition (DED)	Wire or powder is extruded from a nozzle and completely melted by an electron beam or a laser	✓
Cold spraying	Powder is blown at high velocity from a nozzle in order to cause adhesion and form an object	✓

1.2 Powder production

The powders required for the AM technologies must respect some strict characteristics such as the spherical morphology linked to good flowability and a controlled particle size distribution (PSD). In addition, also the presence of satellites must be controlled, which are the smaller particles adhering to the larger ones. The powder's morphology can be referred to the particles' shape, size and surface roughness. These properties deeply influence the final properties of the component as they strongly affect the powder flowability and packing density [9]. For instance, in the powder bed AM techniques, the particles morphology can have a serious impact on the powder bed formation, in terms of homogeneity and development of melt pools. An excessive variation in powder characteristics can lead to defects in layering, low bulk density, not optimal mechanical properties and poor surface finishing [10]. The chemistry is important to assure a controlled and homogenous composition of the final component and the microstructure has to be controlled in order to avoid the presence of internal porosity which can lead to a defect creation in the bulk.

The technologies for the production of metal powders are conventionally classified as physical-chemical methods and mechanical methods. The physical-chemical methods are those that involve physical and chemical transformations. Regarding these techniques, the chemical compositions and structure of the final product might result very different from the raw material. The mechanical methods, instead, take advantage from a mechanical force to produce the metal powders. For instance, several types of milling processes belong to this category, but the more important ones in the AM field are the jet dispersion methods, such as water or gas atomization. These methods exploit a high-pressure medium to perform a disintegration (dispersion) of a thin stream of molten metal [11].

1.2.1 Gas atomization

The most used method to produce metallic powders for AM technology is gas atomization (GA). Here, the medium used to perform the melting dispersion is an inert gas.

As a general idea, gas atomizers are usually formed by a furnace for melting the material under vacuum or under protective atmosphere and an atomization chamber. Here there are the gas nozzles with different configurations where the inert gas is jetted to impinge the molten metal dispersing it in several droplets. The droplets fall down inside the atomization chamber which is tall enough to allow their solidification in flight. The droplets so solidified are the metallic particles, which can be collected from the powder collector [11]. A schematic representation of the gas atomization process is shown in Figure 3.

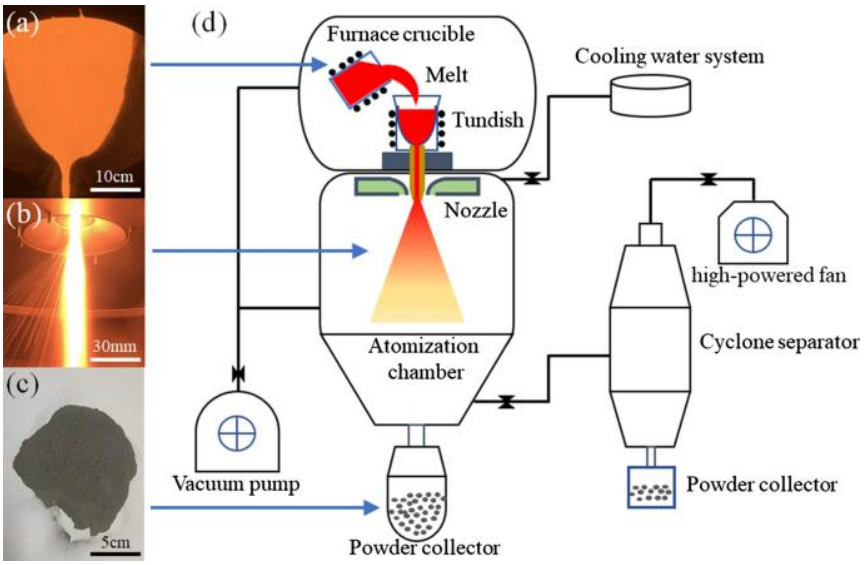

Figure 3: Schematic representation of the gas atomization process. Here is represented the molten metal in the furnace (a), the metal pouring in the atomization phase (b), the metal powder produced (c) and a scheme of the whole process (d) [12].

The advantages of using the inert gas are [13]:

- A better heat exchange between the gas and the particles, which allows a rapid cooling of the particles.
- A minor risk to oxidize the material.
- A higher yield in particle sphericity [14].

In Figure 4 an example of a gas atomized powder is reported.

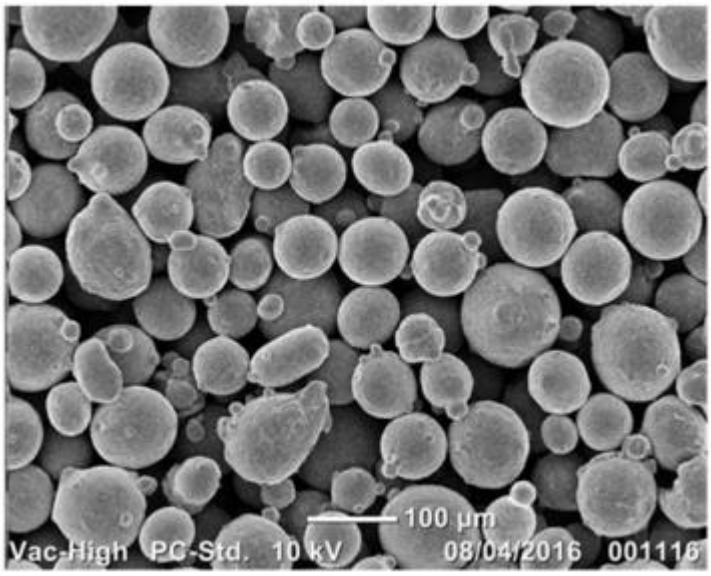

Figure 4: 316L gas atomized powder [15].

Going into details in the description of the process, three phases can be defined: initial phase, working phase and final phase. The start of the initial phase is considered after the material is completely molten. Here, the metal drain valve is opened and, after that, the gas supply valve is opened too. The gas amount is defined according to a precise ratio between the metal and gas flows. The initial phase lasts a few seconds and then the working phase begins. During this phase, the drainage process is stabilized and the ratio of metal and gas consumption in the atomizer is registered. At the end of the working phase the drain of the metal is discontinuous, so the ratio of the metal and gas is disturbed. Then the final phase occurs when the metal is totally drained and the gas valve is closed [13]. The productivity of an atomization process can be improved controlling the working phase, since the powder produced during the initial and the final ones is affected by a transient state of the process. A certain ratio of gas/metal must be kept in order to achieve a qualitative atomization [16].

In general, the parameters to control during the atomization process to assure the best quality characteristics and the required PSD are several:

- Gas atomization pressure
- Melt superheat
- Atomizing gas (usually nitrogen, helium or argon).

- Overpressure applied in the melting chamber.
- Geometry of the gas nozzles.

In general, an increase in the gas atomization pressure decreases the dimensions of the particles [17]. It must be taken into account that the gas pressure can be varied only in a certain range. If the gas pressure is too low the droplets are very coarse and they can reach the collector in the molten state. On the other hand, if the gas pressure is too high the melt can freeze at the tip of the melting tube, causing the clogging of tube and the failure of the atomization [18]. A strict control on the PSD can be obtained correctly adjusting the gas pressure, since each AM production technique requires a specific powder granulometry. Figure 5 shows an example of the effect of the gas pressure on the final product.

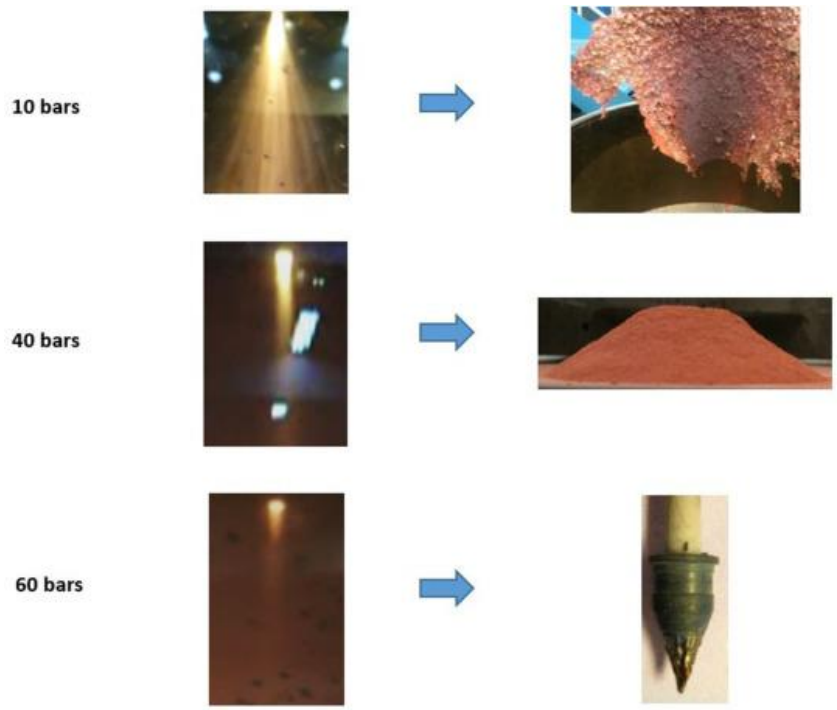

Figure 5: Cu powder atomization with nitrogen at various gas pressures: 10 bars (coarse droplets), 40 bar (powder correctly produced) and 60 bar (melt freezing) [18].

The melt superheating plays an important role on the spheroidization of the powders. The high temperature reduces the surface tension and the viscosity of the molten metal, making the spheroidization easier. In addition, the higher temperature delays the time of solidification and if the spheroidization time is less than the solidification time the final shape of the powders is spherical [18], [19].

The kind of atomization gas influences the dimensions of the powder. In fact, the efficiency of the heat exchange between gas and molten metal depends on the kind of gas used. A more favorable heat exchange leads to a more rapid cool down so to finer powders. In general, using He as atomization gas allows to produce finer powder rather than Ar or N_2 [20], [21]. On the other hand, He is the most expensive than Ar and N_2. The cheapest gas is the N_2, but Ar is the best choice when the material to produce is reactive to the N_2 [22].

The application of an over pressure in the melting chamber is essential to win the counter forces of the molten metal during the pouring phase in the atomization chamber. The main forces are the capillarity and the viscous resistance, which depends on the molten metal chemistry. If the overpressure imposed is not enough to overcome these forces, the metal will stick inside the nozzle provoking the failure of the atomization. This effect is crucial with a very small nozzle diameter. [23]

Regarding the nozzle configurations, two main kinds can be distinguished (Figure 6): the closed or closely-coupled configuration and the free fall configuration [13].

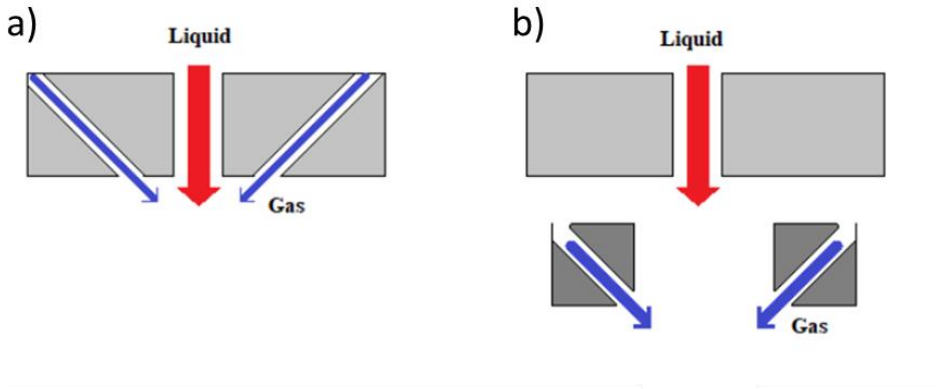

Figure 6: Close coupled configuration (a) and free fall (b) [13].

In the closed coupled configuration, the gas nozzles are very close to the melt stream. This leads to the possibility to produce finer powder due to the favorable energy transfer between gas and melt stream [24].

On the other hand, the melt flow rate is lower than a free-fall configuration, since there is the presence of negative pressure in the melt tube[25]. This effect leads to a very difficult control of the melt flow during the atomization process [26]. In addition, the close-coupled configuration can provoke the freezing of the molten metal tip. In fact, the isentropic expansion of the gas exiting from the nozzle can

strongly lower the gas temperature (even below 0 °C). Since the gas nozzles are very close to the tip of the crucible a sudden decrease of the temperature in this zone can provoke the solidification of the molten metal at the exit and the failure of the atomization [27].

The free fall configuration, instead, consists in the gas nozzles placed far from the melt flow exit. The distance usually can vary from 10 to 30 cm [18]. This configuration leads to the production of coarser powders since the energy of the gas impinging the molten metal is less. An advantage in using this kind of configuration is the absence of melt freezing problem. In fact, the freezing happens especially in the first moment when the molten metal is exiting from the tip. With a free-fall configuration the gas is far away from the tip, so this problem is avoided [13]. In addition, the melt flow control is much easier than in a close-coupled configuration [18].

The main defects which can be detected in gas-atomized (GA) powders are internal pores and satellites.

The porosity inside the powder can be entrapped during the liquid break-. There are different break-up mechanisms and one of the most common stimulated at high gas velocity, is the “bag” break-up. It consists in a melt fragment (or a large droplet) that spreads around the flow, becoming shaped into bag-like plate, due to the too high viscosity. At this point the plate can collapse in small droplets or, if the viscosity rises enough, it can collapse on itself creating a droplet with a pocket of gas trapped inside [28]. The mechanism is represented in Figure 7.

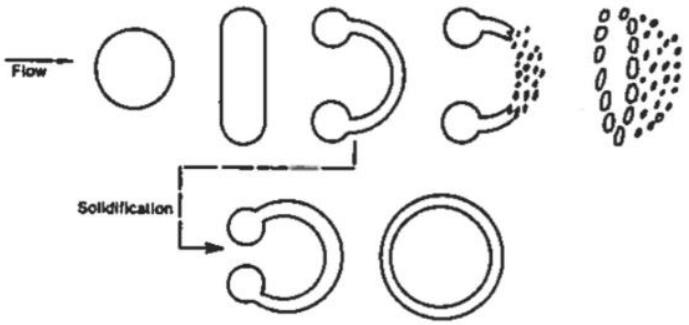

Figure 7: "Bag" break-up mechanism [28].

The satellites formation is a problem which can be detrimental for the flow properties of the powders. This phenomenon occurs due to the encounter between

the finer and coarser particles in flight during the atomization process. The finer particles cool down and solidify before the coarser ones, so the collision happens when the coarser particles are in a semi-molten state. This provokes the welding of the fine and coarse particles which strongly affects the flowability of the final powders, since these particles lost the spherical shape [28].

1.2.2 Water atomization

The water atomization is an established technology for metal powder production for several applications including sintering, welding and metal injection molding [29]. Since the cost of the equipment and of the final powder are lower than gas atomization, coupled with a production rate that is several times higher than the gas atomization technique, there are different studies about the water atomized powder for Additive Manufacturing applications [30], [31]. A schematic representation of the water atomization process is shown in Figure 8. The process consists in melting the metal in a crucible on the top of the plant, then to pour it in the atomization chamber. Here the molten metal free falls in the “Atomization zone”. Depending on the configuration, a variable number of nozzles are symmetrically arranged around the stream of the molten metal and water jets are aimed at the metal stream. Since the pressure of the water jets is very high, the metal stream is divided into several droplets which free fall inside the atomization chamber, through the “Particle Solidification zone”. Here during the flight, the droplets solidify, forming the metal powder. It follows a post process procedure with different steps like dehydration, filtration, classification and packaging of powder [32] .

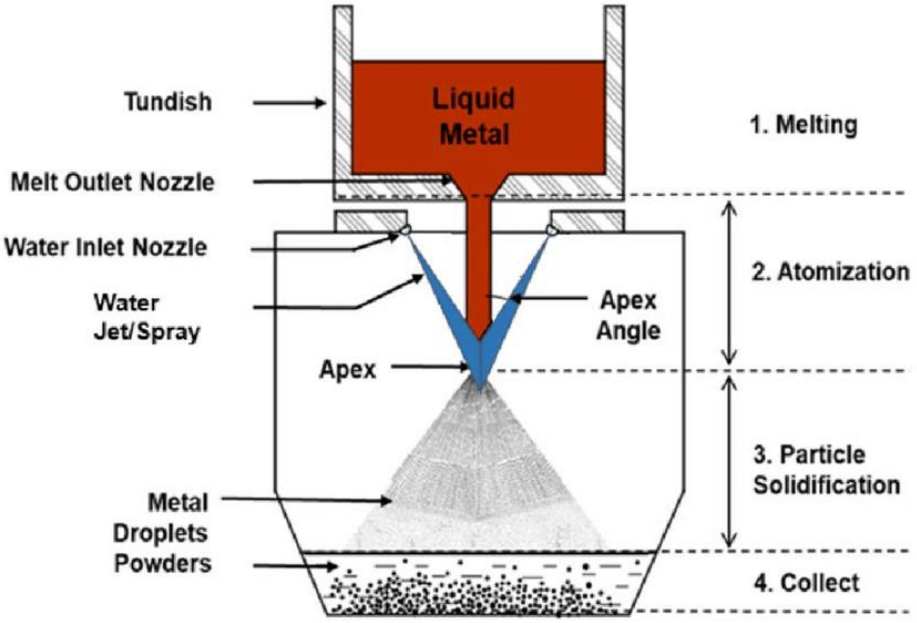

Figure 8: Water atomization process [32]

The Figure 9 shows the morphology of an iron water atomized powder. The main critical point of the application of the water atomized powder in AM processes are:

- Irregular shaped particles
- Oxidation

During water atomization, the cooling is faster than gas atomization, which causes the irregular morphology of the particles. Another possible cause of irregular shaped powders is the collision of droplets before the solidification and the formation of a strong oxide shell [29]. In fact, the oxidation is the second main critical point of the water atomization, which is a problem for the production of materials strongly reactive to the oxygen. [33]

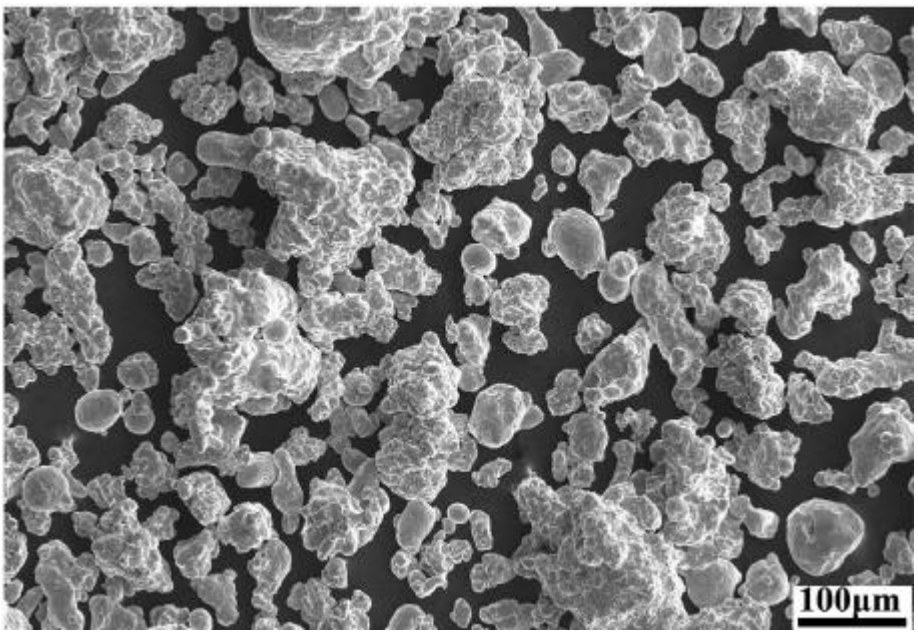

Figure 9: Morphology of water atomized iron powder [33].

1.2.3 Plasma atomization

Plasma atomization is a process developed for the production of high purity powders of high melting point and reactive materials such as tantalum, zirconium, titanium etc. Here the melting phase is different since the material is fed into the atomization chamber in a wire form. A schematic image of the process is represented in Figure 10. Inside the atomization chamber there are plasma torches that directly spread the metal wire into droplets which fall in the chamber, solidifying. The main advantage in using a wire feed stock is the high purity of the final powder, since there is not contact between the metal and cold solid surfaces. In addition, the resulting particle size distribution can be easily controlled by checking the wire speed [11].

In opposition with the gas atomization, here the gas medium is heated by the plasma torches, leading to a higher gas velocity, so to a higher atomizing force. This can allow to use a low gas flow rate. In addition, the use of a hot gas as atomization medium decreases the cooling time, preventing the particles freezing together into irregular shapes. Finally, the use of plasma heating source allows to reach a very high superheat and the consequent cooling assure a complete spheroidization of the powders [34].

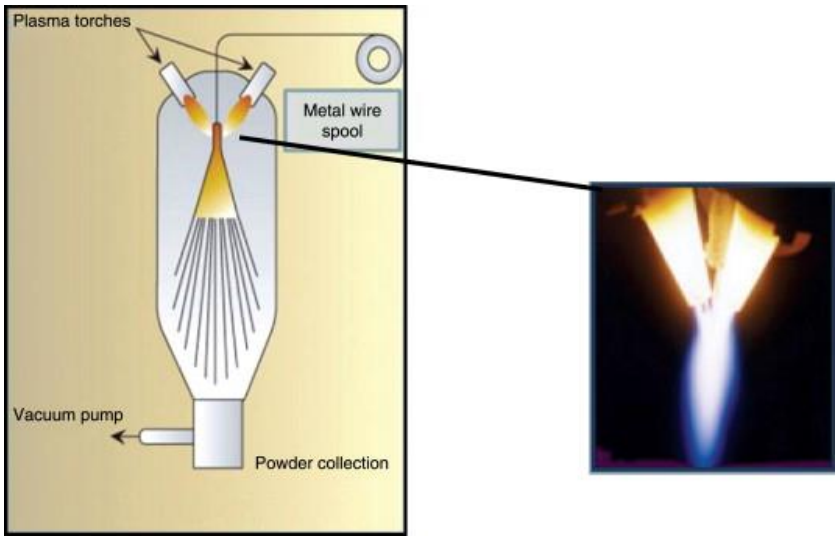

Figure 10: A schematic representation of the plasma atomization process [35] .

The plasma atomization allows to produce spherical powder, satellite free with a narrow particle size distribution [35]. A scanning electron microscope (SEM) images of a plasma atomized powder is showed in Figure 11.

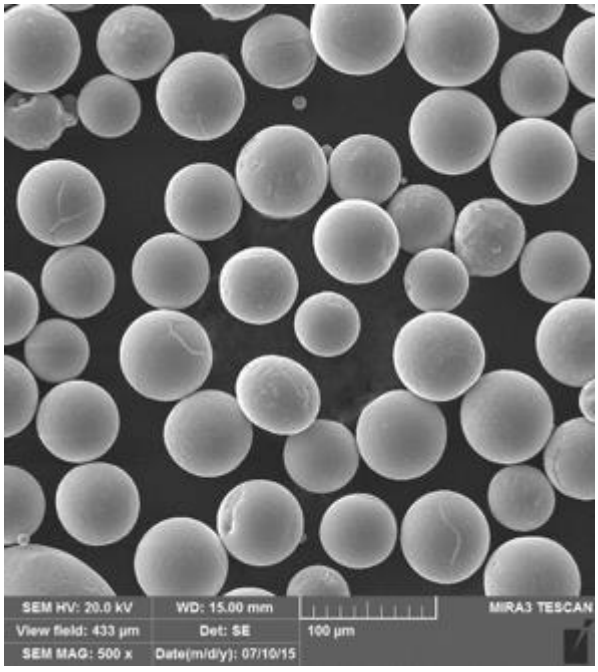

Figure 11: A Ti6-Al-4V powder, produced by plasma atomization [36].

1.2.4 Physical-chemical methods

A rapid overview on the physical-chemical methods is proposed. The first method is the electrolysis which consists in the use of a metal anode as the raw material. It is possible to use pressed and sinter waste metal products to perform the electrolytic deposition in powder form. This technique has the limitation in using only pure metal, but not alloys. Another method is the carbonyl process, which is a chemical method that allows to produce only iron and nickel powders. This technique consists in the reaction of carbon oxide gas under pressure and temperature with the pure metal. This process leads to the formation of carbonyl with is decomposed to metal powder increasing the temperature and decreasing the pressure. Finally, it worth to mention the plasma spheroidization method, which is not a production technique but a sort of "post processing" of the powders. In fact, with this technique irregular shaped powder can be treated in order to achieve an ideal spherical shape. The benefits of this technique are not limited to the shape adjusting of the particles but also include the decrease of internal porosity and the enhanced powder purity [11].

1.3 AM techniques

In general, the metal AM comprises several techniques with different technologies. They can be classified based on the type of feedstock (powder or wire) and on the spreading method. Focusing on the powder feedstock techniques, a first division can be done between Direct Energy Deposition (DED) and Powder Bed Fusion (PBF). These two technologies differ in powders spreading method. In fact, in DED the powder is added and melted at the same time through a nozzle, while in the PBF a powder bed is created before the melting phase. In the next paragraph a deeper analysis of these two technologies is exposed, considering the main two PBF techniques which are the electron beam melting and the laser powder bed fusion. A special attention is given to the laser powder bed fusion since is the subject of this PhD thesis.

1.3.1 Directed Energy Deposition (DED)

DED processes combine a "welding process" with a robotic arm to build up the desired component. The powder is blown out from nozzle through a carrier gas and melted at the same time with a source of energy. The DED heads follow a predefined path to build up the layers of the component [8]. The freedom of movement of the robotic arm allows this technique not only to produce new

components but also to repair existing ones. In general, the deposition rate and the volume density in DED are higher rather than those of the PBF processes, where layer thickness, surface roughness and the minimum feature size of the fabricated part are relatively smaller. The freedom of design of the DED technologies allows to produce also multi-material components since the machines can be equipped with multiple powders hoppers [37].

In DED technologies, the most important parameters to take into account are the laser parameters but also the flow rate of the carrier gas. The nozzle configuration can be coaxial or off axis (Figure 12). In the coaxial configuration the nozzle and the laser beam are mounted on a single head which moves following the geometry of the component to manufacture. In the off-axis configuration, the nozzle and the laser beam are not coaxial, with the nozzle that spreads the powder laterally with respect to the laser beam. The efficiency of the process can be defined as catchment efficiency (ratio of powder supplied to that consolidated). Unfortunately, this value is not so high, in fact it can be less than 50 % in some part configurations. In additions, the over spray powder (the unfused one) represents a problem in terms of cost and contamination of the processing cell. There are significant challenges, including investment in equipment, to capture and classify the overspray powder in order to understand if it is still suitable for being processed (not degraded) [38].

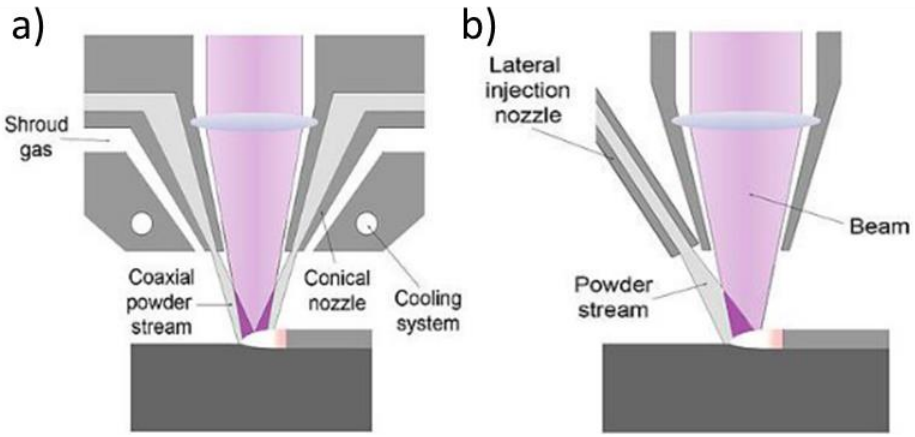

Figure 12: Schematic representation of coaxial (a) and off-axis (b) DED configurations [38].

According to the components final quality in terms of surface roughness, DED generally allows to produce components with Ra between 10 and 25 µm. The dimensional accuracy is around 0.3 mm for 100 mm length. The layer thickness cannot be compared with the PBF techniques, since here it is not a constant value.

In fact, the layer thickness depends on the speed of the nozzle and on the rate of material deposition [39].

1.3.2 Powder Bed Fusion (PBF)

PBF stands for "Powder Bed Fusion" and includes all the AM technologies which imply spreading the powder on a building platform and creating a powder bed through different methods. After that, the powder bed is melted through an energy source. The process is repeated layer by layer until the components are built.

One of the most critical parameters to consider in PBF techniques [40], which is not controllable in DED technology, is the layer thickness, which indicates the thickness of the single layer of powder. Layer thickness is essential to define the final properties of the components but also the productivity since the lower the layer thickness, the faster the process.

The primary division in PBF techniques is based on the energy source supplied to melt the powders. Electron Beam Melting (EBM) uses an electron beam as an energy source. On the other hand, the Laser Powder Bed Fusion (LPBF) uses a laser beam. These two technologies are described in more detail in the next paragraph.

1.3.2.1 Electron Beam Melting (EBM)

The electron beam melting is a technique included in the PBF technologies and it was originally developed by Arcam AB. The first commercial EBM systems were available from 2005, produced by Arcam AB. The EBM technology implies the creation of a powder bed on the building platform by raking or rolling system, fed from the powder containers. An electron beam as energy source melts selectively specific areas of the powder bed based on the geometry of the component. The melting chamber and all the electron equipment are maintained in high vacuum. After the first layer is finished, the building platform is moved down and covered again by new powder. This operation is repeated for every layer until the building is completed. The electron beam is focused on the building platform through electromagnetic lenses and electromagnetically scanned by deflection coils. Initially the electron beam is focused on the building platform in multiple passes at a scan rate of $\sim 10^4$ mm/s with high beam current and a focusing spot of about 1 mm. This operation is called "preheating" and it can raise the temperature of the powder bed up to 0.6-0.7 times the melting temperature. After that, a second step

of scanning is performed with a reduced speed of ~10^2 mm/s and with much lower current and maximally focused [41]. A schematic representation of the EBM technique is shown in Figure 13.

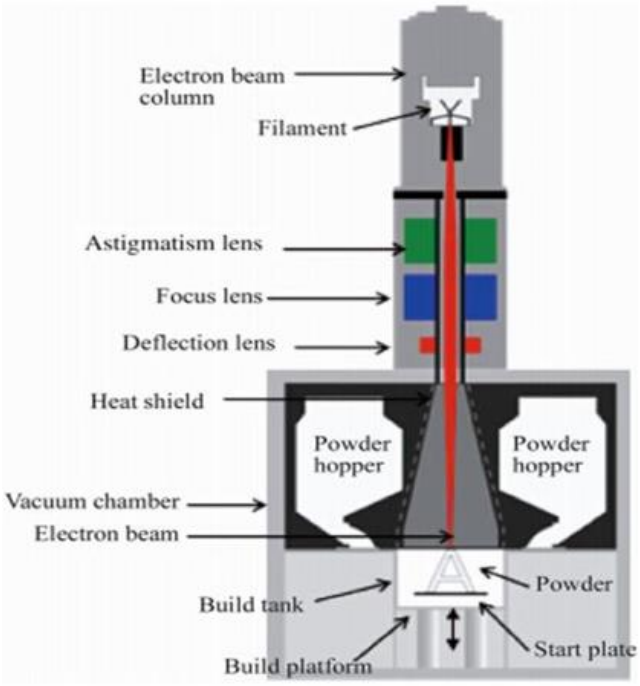

Figure 13: Schematic representation of an EBM process [42].

The reason of the preheating step is due to an effect of explosion or "smoke" effect caused by the interaction of the metal powder and the electrons. Since the electron are "physical" particles, the impact with the powder can move them and affect the homogeneity of the powder bed. This phenomenon is more critical with higher beam current. The preheating step allows to pre-sinter the powder and to constrain the powder to the powder bed [43].

The EBM process is considered a "hot process" because the powder bed temperature is maintained high for the whole building phase. This leads to the possibility to process also brittle materials. In fact, these materials, like intermetallic, present a poor thermal expansion and contraction. Since the cooling rates in the additive processes are very high (up to 10^6 K/s), the transformation from liquid to solid phase is fast and there is not the possibility to accommodate the internal residual stresses, which lead to the formation of cracks. In the EBM process this effect is strongly limited from the high temperature of the powder bed which

allows a release of the residual stresses. On the other hand, the pre-heating phase increase the building time and the chamber becomes very hot during the process, which it may require a lot of time to cool down before the building platform can be removed [44].

The surface roughness (Ra) achievable with EBM is between 25-35 μm. The dimensional quality is around 0.4 mm per 100 mm length. The layer thickness available is in the range 50-200 μm [39].

1.3.2.2 Laser Powder Bed Fusion (LPBF)

The LPBF process is also known as Direct Metal Laser Sintering (DMLS), a process patented by EOS in the 1994 or as Selective Laser Melting (SLM), a term introduced by the Fraunhofer Institute in the 1995 [45]. This technology is the main focus of this PhD thesis since all the bulk samples and the parameters optimization test were performed using an LPBF machine.

Since LPBF belongs to the family of PBF technology, the building phases are similar to ones already described in the EBM section. The working area is enclosed and filled with inert gas in order to prevent oxidation. A roller or rake (also called recoater) spreads the powder on the building platform and a laser melts the particles following the cross-section of the final component. When the operation is completed, the molten areas are solidified, and the building platform is moved down in order to repeat the process. The movement of the platform is defined by the layer thickness [46]. In this case the process does not require a preheating phase since there is not the possibility of "smoke" effect with a laser as energy source. On the other hand, the building platform can be heated up in order to prevent residual stresses in the first layers, which can lead to delamination and bad adhesion of the powders to the platform. A schematic representation of the LPBF process is shown in Figure 14.

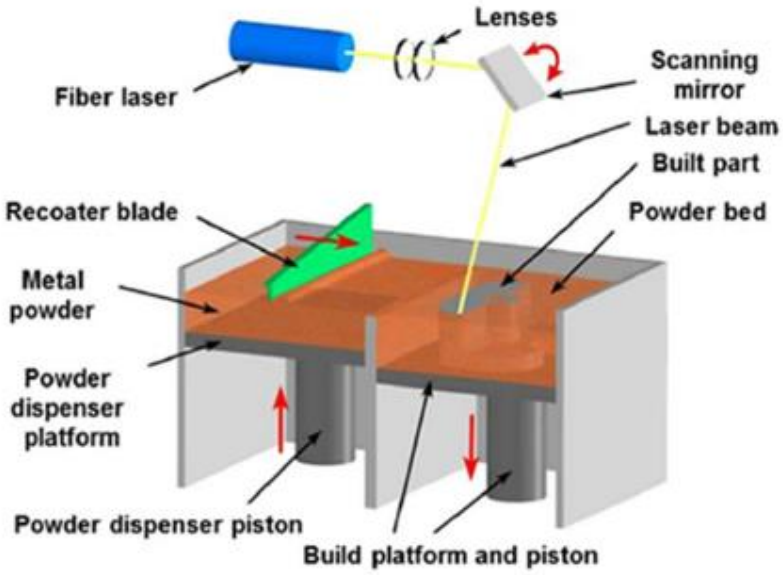

Figure 14: Schematic representation of an LPBF process [47].

During the process the laser selectively melts the powder bed, by focusing the energy in a very small area. The result of this interaction leads to the formation of melt pools. [49]

A melt pool creation scheme is shown in Figure 15. The shape of the melt is arc shaped along the building direction. The energy density is maximum at the center of laser beam, where the consequent melt pool depth is maximum, decreasing gradually up to the edges of the laser beam. Due to the heat transfer in the external part of the melt pool a so-called heat affected zone (HAZ) is created. In general, the width of the melt pool and the HAZ is larger than the laser beam diameter. Optimal building parameters have to create a melt pool whose depth is so to assure that not only the new powder layer is melted but also the underlying solidified parts. This results in an overlapping of melt pools, which assures a good consolidation of the component. For this reason, the melt pool depth has to be greater than the layer thickness, to provide a good bonding between the successive layers of the component [48] .

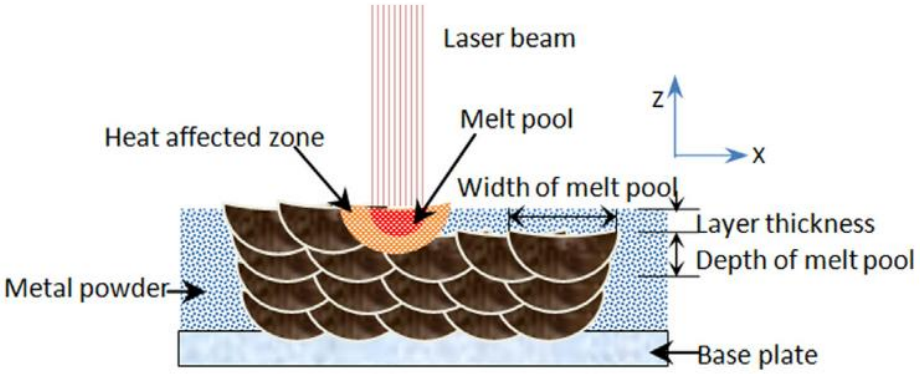

Figure 15: Schematic representation of the melt pools [48].

Different LPBF machines are now available on the market. Almost all the suppliers classify their machine based on the general characteristics such as the number of lasers, build chamber's size and maximum power. Based on these characteristics the LPBF machines can be classified into three main categories. The first one is the category of research machines (small machines). These machines are generally used for small builds in companies and universities. The small machines are especially useful to realize prototypes, which need rapid tests, or samples, to study the LPBF process and optimize it. The chamber size is up to 250x250x250 mm^3 and almost all the small machines have a low laser power (up to 200 W). The advantage in using these kinds of machines is the short set up time, a very good quality surface and part details. The second category is covered by the medium size machines. In this case the chamber size is up to 400x400x400 mm^3, with a laser power that can reach 500 W. These kinds of machine are used in research, as the previous ones, whenever the building of bigger samples or components to test is required. The performances are similar to the industrial machines with the advantage of a shorter building time, lower cost and less maintenance required. The last category includes the heavy industrial machines. In this case the chamber volume is much bigger (up to 18.75x10^6 mm^3) and the laser power can reach 1.5 kW. These are the most expensive ones and there are several types based on the needs of the customer [49]–[51].

The Ra of the components produced by LPBF is around 11 µm. The dimensional accuracy is around 0.2 mm per 100 mm length. The layer thickness available varies from 20 to 100 µm [39]. Based on these final characteristics LPBF is the best choice in terms of dimensional accuracy and surface quality.

1.3.2.2.1 LPBF: process parameters definition and materials available

LPBF is a complex process which requires a lot of optimization and controls. The variables involved in the process are several and only a good combination of all the parameters leads to fully dense final components. The number of process parameters is around 50 [52]. As a result, it is challenging to have a full monitoring of the process physics and to develop an effective process control strategy. In general, the main process parameters are [53]:

- Laser and scanning parameters.
- Powder properties.
- Powder bed and recoat parameters.
- Build environment parameters.

The control of the laser parameters is very important to take into account. This group of process parameters includes the laser power (P), the area where the laser beam is applied (spot size) and the amount of time the energy is applied to that area [54]. This time is defined by the laser scan speed (v). Typical laser scan speed values are between 100 and 1000 mm/s [55]. These parameters can change based on the area of the component being built. For example, different laser power can be applied in the center of the geometry and in its contour. Another difference can be represented in printing the supports where the manufacturing speed and the densification are important but not the surface finishing [53]. The distance between two contiguous laser scans is defined as scan spacing, or, more common, hatching distance (h). Typically, an overlap of the scan tracks is desired, since it promotes a better bonding in the layer, as already explained in the previous paragraph [53]. Another important laser dependent parameter to take into account is the wavelength of the laser, strongly linked to the absorptivity of the material to process [56]. In fact, there are some materials which show a high reflectivity to laser at certain wavelengths. This leads to more energy to supply during the process, to achieve optimal properties in the final component. Nowadays, the most common lasers for LPBF used in industry are the unpolarized IR laser (wavelength ~1.06 μm). The laser can be used in continuous mode or in pulse mode. The continuous mode ones are the standard in industries, but the pulse mode showed some benefits in terms of preventing cracking and controlling the microstructure of the components [57].

The scanning strategy plays an important role, as well. The scanning strategy is the spatial moving pattern covered by the laser beam. In a single layer the scanning strategy varies in terms of scanning direction, scanning sequence, scanning vector rotation angle, scanning vector length, scanning time and hatching distance. The scanning pattern properties affects the final characteristic of the components. For instance, a long scanning line causes an excessive residual stress which has a negative impact on the quality of the part. On the other hand, a rotating pattern promote the overlap of the tracks between the layers, leading to a better consolidation of the powders [58]. The most common scanning strategies are shown in Figure 16.

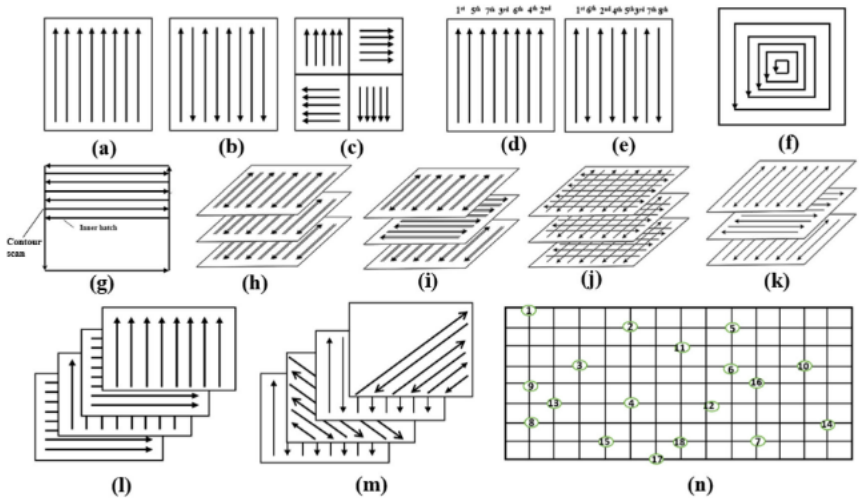

Figure 16: Representation of different scanning strategies: unidirectional (a), zig/zag (b), island (c), variation of scanning sequence based on unidirectional scan (d) and zig/zag (e), helix scan (f), contour scan (g), zig/zag double pass (h), zig/zag-double pass-90° rotation between layers (i), cross scan (j), zig/zag-single pass-90° rotation between layers (k), unidirectional-90° rotation between layers(l), 45° rotation of scan vector (m) and point melting scan (n) [58].

The powder properties were already discussed in the paragraph “Powder Production”. Focusing on the powder bed properties the most important parameter is the layer thickness (t). This value must be wisely chosen in order to have a good re-melting between the layers (to promote a better bonding) and to not increase too much the building time, especially in industrial field. Another important parameter is the powder bed temperature, which can be increased through radiant heaters in the build chamber or heating the walls of the power collector. The powder bed temperature influenced the heat transfer process and the thermal gradient into the process, having a strong impact on the thermal stresses of the final parts [54].

Last but not least the building environment has to be controlled. The melting process has to be conducted in a low oxygen atmosphere to prevent oxidation and general degradation of the powder, which can impact negatively the mechanical properties of the parts. This goal is achieved by a combination of positive pressure of inert gas, such as argon or nitrogen, and in some cases vacuum pumping, to clear the building environment from the air [53].

It is important to highlight that all these parameters interact with each other. The modification of one of them can affect the other ones and so the building process. It is mandatory to keep a general overview on the entire process in order to achieve the best quality possible for the final component, without compromise the time effectiveness of the process, especially in industrial field [5].

The most important process parameters in terms of energy delivered on a single layer of powder are laser (P), scanning speed (v), hatching distance (h) and layer thickness (t). In order to have a general idea on the combination of these process parameters and to design experiments on optimization it was defined a factor called volumetric energy density (VED) [59]:

$$VED = \frac{P}{v \bullet h \bullet t}$$

The energy density is especially useful in design of experiments (DoEs) when an optimization of process parameters is required. As a matter of fact, each material can have a range of energy density to supply which assure good final properties and this range can be used as baseline for further optimizations. Another application can be the manufacturing with a new LPBF machine. To have a reference of the energy to supply makes easier the optimization process.

The most common alloys nowadays available for LPBF include pure titanium, Ti6Al4V, 316L stainless steel, 17-4PH stainless steel, 18Ni300 maraging steel, CoCrMo, nickel-based superalloys such as Inconel 625 and Inconel 718 and aluminum alloys. The range of materials is in constant expansion due to the growing of the demand in different applications. Precious metals such as gold, silver and platinum which currently are also starting to be processed by LPBF. In the next pages an overview on aluminum alloys will be described in more detail, focusing on the material, subject of this PhD thesis.

1.3.2.2.2 Process parameters optimization by Single Scan Tracks

The previous paragraph gave an overview of the main process parameters involved in the LPBF process, highlighting how complex the interaction between them is. Once a suitable powder is produced, it is necessary to find the proper process parameters window. The main goal is to apply the proper process parameters to achieve fully dense samples close to the theoretical density.

In order to study the process parameters, there are different experimental approaches. The "classical approach" consists in building small samples, usually cubes, varying the process parameters in a single Job. After that, the cubes are studied in terms of density to understand the best combination of process parameters linked to the best densification achieved. This method is overly time-consuming and low-performing since each combination of process parameters corresponds to a cube, which must be analyzed singularly [60]. In the literature, it has been demonstrated that the approach of single scan tracks (SSTs) represents a better choice to define the proper value of P and v, with a limited consumption of powder and a rapid applicability [61]. SST consists of single laser tracks previously spread onto a substrate. With this approach, with a single layer of powder (with a fixed layer thickness), P and v can be combined in different modes inside a single job with a significant save in terms of time and powder.

In the literature, many works on SSTs are reported. In most of these studies, SSTs were analyzed looking at their cross-section or evaluating the on-top morphology. In Figure 17 representative SSTs optical microscopy images of both views, cross-section and on-top, are represented.

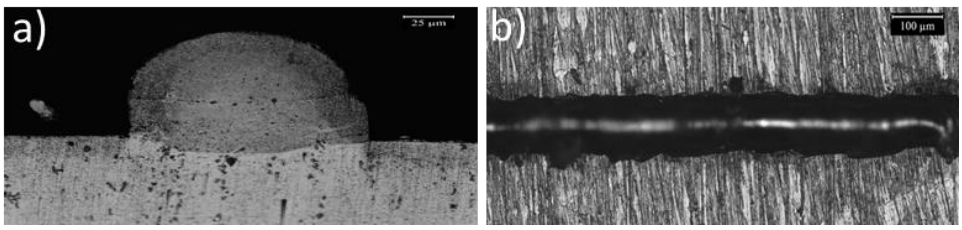

Figure 17: cross-section view (a) and on-top view (b) of an SST.

Regarding the cross-section view, the primary analyses evaluate the geometrical features of SSTs. For instance, Yadroitsev et al. asserted that the width, growth, depth and contact angles of the SST can be correlated to the melting behavior of the power, which is linked to its LPBF processability [62]. Aversa et al. reported that several considerations on the SSTs cross-section morphology can be made. For instance, stable SSTs usually present similar growth and depth values. On the other hand, low depth or contact angles values can be correlated to an incorrect process parameters choice [63].

Moving on to the on-top view, many works in literature followed this approach. For example, Childs et al. and Wei et al. tried to correlate the LPBF parameters to the surface quality of the SSTs in terms of border roughness [61], [64]. In other works, the authors tried to classify the SSTs based on their morphology, even in cases of significant defects linked to insufficient or excessive energy supplied to the powder [63], [65]. In this way, it was possible to define a correct energy range which led to the formation of a “thin and stable” SST [63]. A significant result in SSTs analysis was achieved by Bosio et al. In their work, the authors demonstrated that also the hatching distance could be selected by on-top analysis of SSTs, measuring the width of the tracks. This result allows to calculate and choose the proper overlapping between the laser tracks, which leads to better densification of the samples [66].

This thesis gave particular attention to the SST approach, highlighting the importance of using such a rapid and powder-saving method to define process parameters. A further relevant result on the on-top analysis approach , which will be described in detail at the beginning of Chapter 3, was also achieved.

1.3.2.2.3 Defects in LPBF

As previously described, LPBF is a very complex process with several variables being involved. As already explained, the good choice of process parameter can be a challenge, especially with new materials to process. The bad choice of process parameters leads to defects which can be divided roughly in:

- Porosity.
- Cracking.
- Impurities (slag).
- Geometrical defects.

The formation of pores is characteristic of an unsuitable parameter optimization in LPBF. The kind of pore is linked to the different melting modes which can happen during the process. The most common classification is to divide these modes in balling mode, conduction mode and keyhole mode (Figure 18). In balling mode, the melt is not wetting the substrate and breaks into a ball-like features due to hydrodynamic instabilities. The common causes of this effect could be oxidation which changes the wetting behavior or an insufficient energy to perform the melting and, as a consequence, a poor penetration of the melt pool in the substrate[67]. In conduction mode the melt is wetting the substrate and there is a good penetration of the melt pool in the substrate. The last melting mode is the keyhole mode. It happens when the power is very high, causing the evaporation of the melt. As reaction, the recoil pressure of the melt pool is increased and is high enough to create a depression in the melt. This phenomenon increases the absorptivity of the melt, since the reflected part of the light is trapped inside the depression. As a consequence, the melt pool depth rapidly increases, creating a keyhole shape which gives the name to the melt mode. If this structure is deep enough it will collapse entrapping gas inside and forming a pore [68].

A common cause of porosity in LPBF components is due to gas entrapping during the melting phase. The gas which leads to spherical porosity formation can derive from the gas atomization process (gas entrapped in the powders) [69].

Another common defect in LPBF is “lack of fusion”. It can happen with a conduction mode, mainly due to the gap between the laser tracks or in general insufficient energy to melt the material. It is clear that, generally, the formation of these defects can be reduced with laser tracks closer to each other and so adjusting parameters such as hatching distance, layer thickness and scanning strategy [70]. On the other hand, the balling mode can also lead to lack of fusion since the melt is not penetrating the substrate, which leads to inadequate adhesion between layers and an incorrect balance between melting new layers/re-melting previous layers.

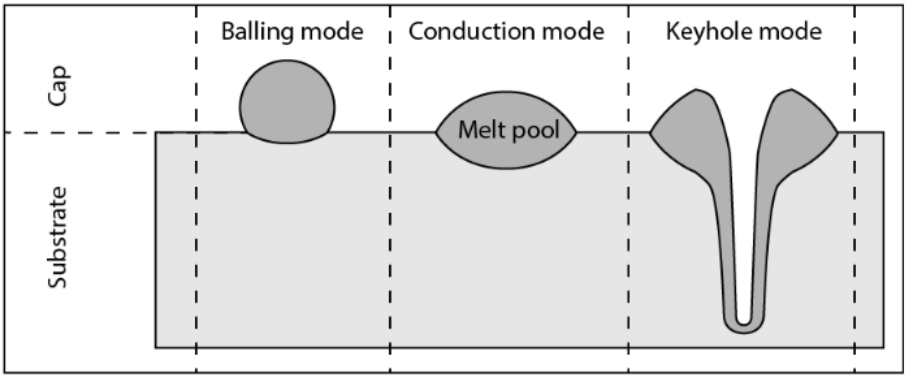

Figure 18: Schematic representations of the melting modes in LPBF [67].

Some materials are subjected to hot cracking, during the LPBF process. These group of materials includes high strength aluminum alloys such as A2024, A6061 and A7075, high carbon steel and some Ni-based superalloys. As described in the literature, hot cracking happens due to the high solidification range. During the solidification (with wide solidification ranges) a thin layer of liquid at the grain boundaries of columnar grains is formed, due to the strong heat gradient. It happens that the film of liquid not always can fill the gap between the grains, leading to the formation of cracks along the building direction [71]. The problem can be avoided increasing the temperature of the powder bed or in some cases the energy density [72]. Another solution to overcome this problem is the use of inoculants, especially when the hot cracking is a consequence of the columnar microstructure, typical of LPBF. The presence of inoculants in the alloy's composition leads to the formation of a finer equiaxed microstructure, decreasing the susceptibility of these systems to solidification cracking [73].

Delamination is another common defect that can happen during LPBF. In fact, the rapid solidification in the LPBF process can create strong residual stresses which can lead to the distortion of the single layers and so delamination [74].

Other defects include warping and spatter. Warping is the bending of the part caused by residual stress. The residual stress induction in the process can be mitigate increasing the temperature of the platform, choosing an optimized scan pattern for the geometry to print or build the components on supports, which can be easily removed in the post processing steps [75]. Finally, the spatters formed during the process can be included on the powder bed, leading to lack of fusions. This problem can be solved by decreasing the percentage of oxygen but also controlling the process parameters, such as laser power and scan speed [76].

1.4 Aluminum alloys

Aluminum alloys are the most widely used metal structural materials, after iron and steel. The main characteristics comprise low density, high specific strength, good electrical and thermal conductivity, easy processability and good corrosion resistance. The fields of application of aluminum alloys are several including aviation, aerospace, automotive, naval and power electronics [77], [78].

A first classification can be done based on the production process, dividing the aluminum alloys in cast alloys and wrought alloys. Aluminum alloys are further classified based on their chemical composition. For instance, the series 2XXX, 6XXX and 7XXX belongs to the heat treatable alloys and 1XXX, 3XXX, 4XXX, 5XXX series are not heat-treatable alloys whose properties are enhanced by solid solution or mechanical deformation [79].

Actually, the majority of the structural parts made by aluminum alloys are produced by traditional methods such as casting, forging, extrusion or powder metallurgy. Despite of the extensive use of aluminum alloys components produced with traditional technique, there are still many problems to solve. First of all, the coarse microstructure obtained from the casting process due to the low cooling rate, can influence the final mechanical properties of the components. Also defects such as shrinkage porosity, slag inclusion and element segregation can be detrimental for the properties and limiting the applications. Another problem is related to the post-processing, since the high-performance aluminum alloys are obtained with a first production process, followed by different post processing steps. This can affect the time effectiveness and the flexibility of the production chain [80]. Finally, the complex shape requirements in application such as light weight and high load carrying capacity, are becoming very common and cannot be easily achieved with traditional processes [81]. For this reason, LPBF represents a valid alternative to overcome the problems derived from the traditional processes.

Compared with iron-, nickel- and titanium-based alloys there are some critical points in processing aluminum alloys via LPBF, to take into account [77], [82], [83]:

- The poor flowability of aluminum powder caused by the low density and tendency to agglomeration can negatively affect the spreading of the powder.

- The laser reflectivity of aluminum reaches 91%. For this reason, a high laser power is needed to achieve dense components, so the power demand of the equipment is higher. The high thermal conductivity is also a problem, since it increases the cooling rate and so the susceptivity to crack formation\s. In addition, lower heat accumulation can lead to the formation of defects such as pores.

- The high reactivity of aluminum with oxygen leads to an easy oxide formation. The presence of oxides films will induce surface passivation of the molten pool changing the melting behavior. This can lead to formation of defects like pores, cracks or lack of fusions.

- The moisture absorption of the aluminum powder is severe. In addition, the solubility of hydrogen in the melt is high leading to hydrogen porosity induced.

- Some aluminum alloys have a high coefficient of thermal expansion and a wide solidification range. In high cooling rates processes these characteristics are linked to the formation of solidification cracks.

- Some aluminum alloys often contain elements such as Mg and low melting point compounds to improve the final properties. With high energy supplied these elements can reach the boiling point changing the final chemical composition of the parts.

The Si is added to the composition to overcome the problems related to the fluidity and the wide solidification range. As it can be noticed from the phase diagram in Figure 19, at 12.6 wt% of Si, the aluminum forms a eutectic where the melting point is the lowest and the solidification arises at a single temperature [33]. The most used Al-Si-Mg alloy is the AlSi10Mg, which has been widely studied in the LPBF processes and it is the main material subject of this PhD thesis. A detailed description of this alloys will be exposed in the next paragraph.

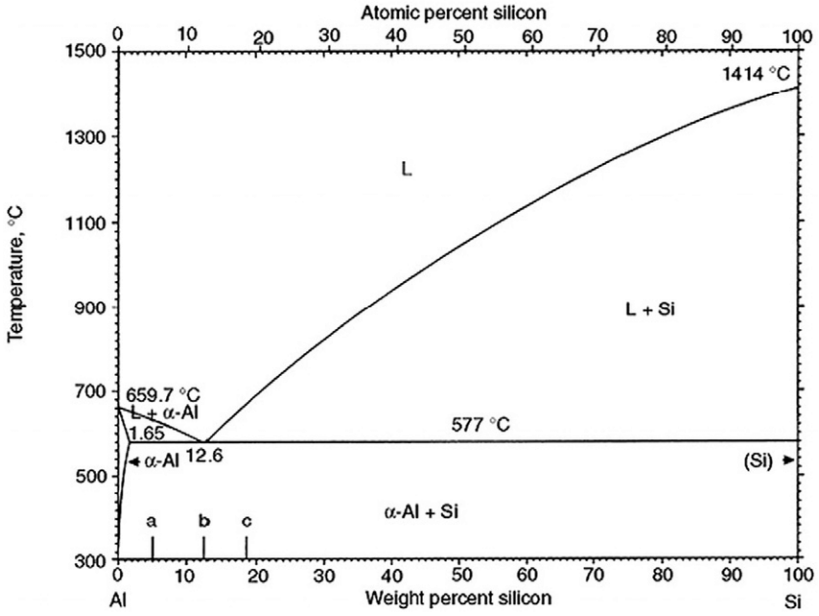

Figure 19: Phase diagram of Al-Si [84].

1.5 AlSi10Mg

AlSi10Mg is one of the most used alloys for LPBF due to the good melt fluidity and ease in manufacturing. The main benefits of this alloy are the low cost, lightweight and high corrosion resistance. In addition, the presence of Mg in the composition includes a hardening factor which improves the mechanical properties [85]. The chemical composition is showed in the **Table 2**[86].

Table 2: AlSi10Mg composition [86].

Element (%)	Si	Fe	Cu	Mn	Mg	Ti	Al
AlSi10Mg	9–11	≤ 0.55	≤ 0.05	≤ 0.45	≤ 0.2–0.45	≤ 0.15	Balance

The AlSi10Mg powder production for LPBF is mainly performed via gas atomization. There are different works in the literature about this topic. Gao et al., for example, studied the production of AlSi10Mg with a self-developed double-nozzle gas atomization. They studied the variation of the atomization parameters in relation to the final characteristics of the powder. The powder dimension decreased with the increase of superheat but increased with the increase of the nozzle diameter and of the gas pressure. The morphology of the powders was spherical with the most of powders produced with a median bluntness (a morphology shape

descriptor) value above 65% [87]. Li et al. studied the role of viscosity and the forces involved during the metal flow in gas atomization. They performed various experiments with aluminum alloys and in particular with AlSi10Mg, varying the nozzle diameter and the overpressure in order to establish a threshold to avoid the nozzle clogging. They noticed that the melt flow resistance (so the tendency to nozzle clogging) increases severely with the decrease of the nozzle diameter. This represents a problem since the decrease in nozzle diameter is translated into finer particles production (Figure 20), i.e. an higher efficiency of the process. They showed that this problem can be overcome applying the right overpressure to the melt, in order to win an eventual high melt flow resistance [88]. Im et al. established that a nozzle diameter of 4 mm for AlSi10Mg powder production is the best in terms of final powder quality. They achieved powder with Hausner ratio of 1.24, showing a good flowability [89].

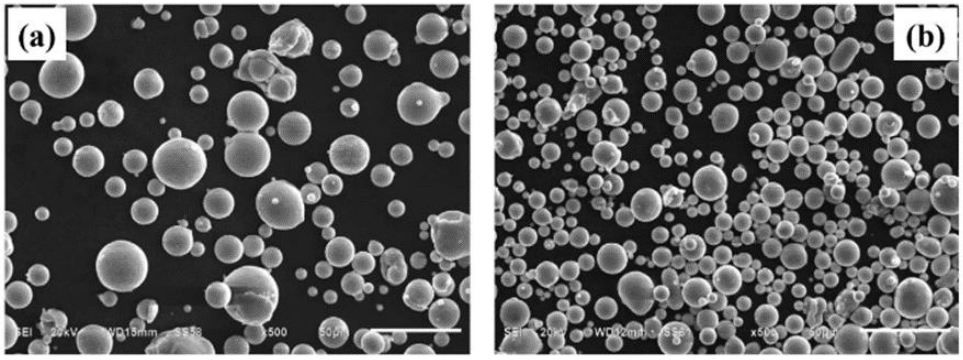

Figure 20: AlSi10Mg powder produced in the same condition but with a melt nozzle of D=3 mm (a) and of D= 1 mm (b)[88].

According to the bulk components' production, it is very important to give an overview of the microstructural changes between the traditional production techniques and LPBF. This is very important since the different microstructure deeply influences the final mechanical properties of the components and, as consequence, its possible applications. In a traditional casting process, from liquid phase, big α-Al grains start to solidify with the Si in solid solution, up to the eutectic point. From the solid solution of Si and Al, during the slow cooling, the silicon precipitates in relatively coarse particles (Figure 21). The result is a continuous eutectic structure of Al and Si, with the Si dispersed along primary α-Al [59].

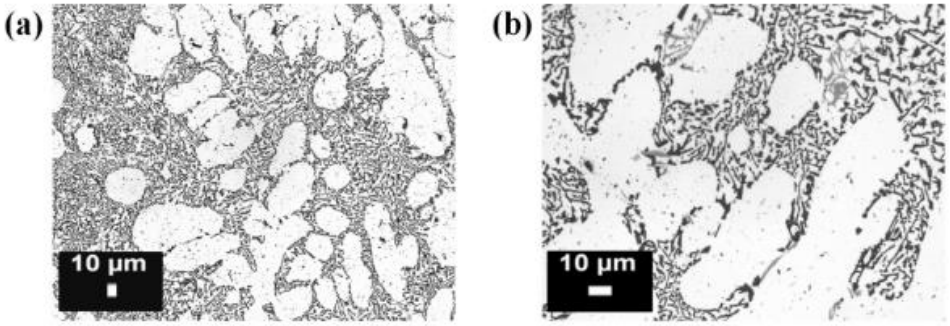

Figure 21: Optical micrographs of an AlSi10Mg alloy microstructure produced by casting at low (a) and high (b) magnification. The white areas are the α-primary grains while the dark ones are composed by α-Al+Si phase [59].

The high cooling rates involved in the LPBF process lead to the formation of a very fine cellular dendritic microstructure. A typical AlSi10Mg microstructure comprises the α-Al cells/dendrites surrounded by a fibrous Si-eutectic network, as showed in Figure 22. The cells of the network present different dimensions due to the heat flux generated by the scans. In the center of the melt pools a very fine cellular dendritic is found while a coarser dendritic structure can be found moving from the center to the edges of the melt pools. Three zones can be detected: a fine dendritic (FD) microstructure in the center, a coarser dendritic (CD) microstructure in the transition zone from the center to the border and a heat affected zone (HAZ) where the remelting of previous layers occurred [86].

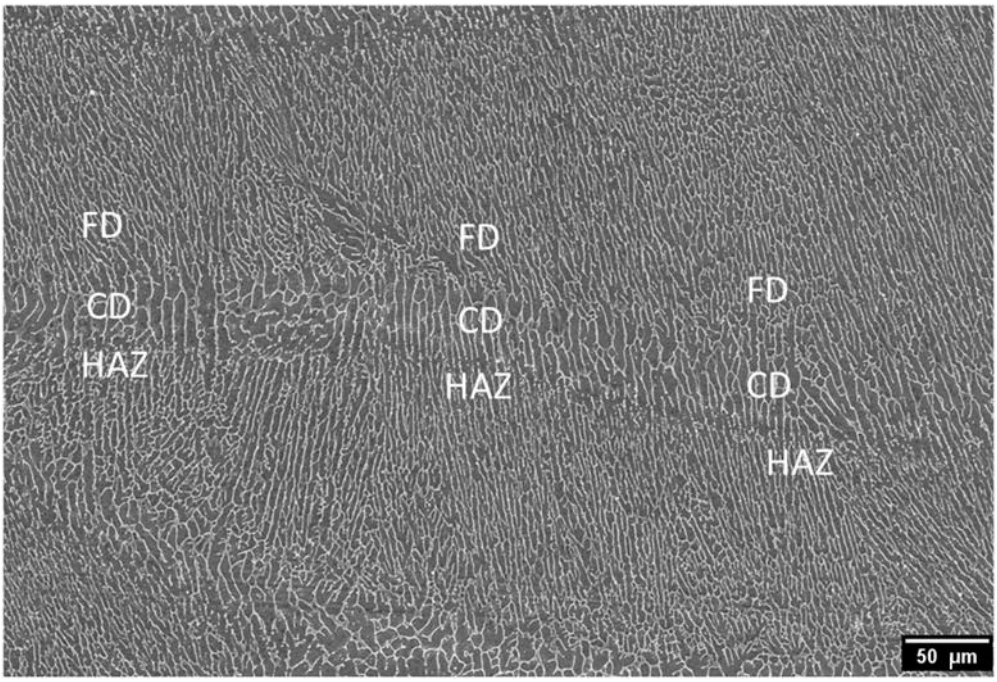

Figure 22: The three zones of as-built AlSi10Mg (building direction) microstructure: fine dendritic (FD), coarse dendritic (CD) and heat affected zone (HAZ).

Rosenthal et. al described the details of the solidification process in AlSi10Mg produced via LPBF[90]. The solidification depends on the thermal gradient (G) and on the growth rate (R). This parameter can be modulated by varying the scan speed and the angle between the direction of laser track and the growth direction of the material. A low R with a constant G is related to a stable planar consolidation front. Increasing R induces the cellular structure formation with dendritic solidification morphology. The product GxR gives the cooling rate of the system: the higher the product the finer the microstructure. Because of this reason, the product GxR is maximum in the middle of the melt pool and decreases gradually reaching the border [90]. In Figure 23 is shown the trend of G and R, related to the microstructure.

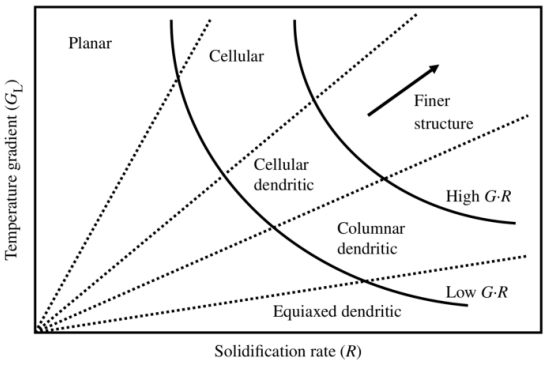

Figure 23: Effect of G and R on the microstructure [91].

AlSi10Mg in the as-built condition is characterized by high mechanical properties. This is due to the rapid solidification, which promotes the formation of a very fine microstructure and the modification of the silicon eutectic phase, as it is described before. As consequence, the ultra-fine microstructure is linked to a high number of cells boundaries which represent an obstacle to the dislocation motion [92]. In addition, during the layer by layer process the alloy is subjected to a "self-quenching" treatment. In fact, the melt pools, surrounded by the previously solidified layers, cool down very quickly. When the next layer is built the laser re-heats the material, a sort of artificial ageing process starts, promoting the precipitation of Mg_2Si [93], [94]. The result is an alloy with high mechanical properties in terms of yield strength (YS) and ultimate tensile strength (UTS), but with a limited elongation.

The mechanical properties of AlSi10Mg can be tailored through post processing heat treatments. Takata et al. studied the microstructure variation and the mechanical properties of AlSi10Mg produced via LPBF, after heat treatment. The first treatment that they performed was an annealing (300 °C for 2 h). Starting from a microstructure as already described in Figure 22, the annealing treatment leaded to an enlarging of the Si phase and a precipitation of Si particles inside the α-Al cells. The second treatment was a solution treatment (530 °C for 6 h) which leaded to a further enlarge of Si particles and a precipitation of intermetallic rod like phase, identified as β-AlFeSi [95]. A schematic representation of the various conditions is showed in Figure 24. The mechanical properties were evaluated for sample built in XY and Z direction. In general, the heat treatments leaded to a decrease in yield strength and ultimate tensile strength but increasing the elongation, the most critical

property in AlSi10Mg. The best compromise was achieved with the annealing treatment as showed in **Table 3**.

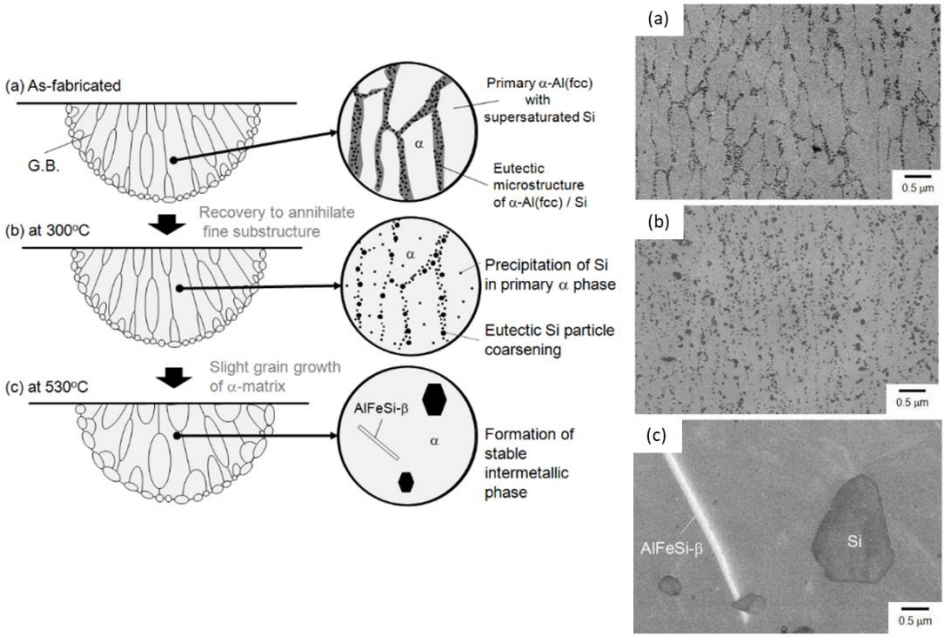

Figure 24: The variation of AlSi10Mg microstructure with the heat treatments (modified from [95]).

Table 3: Mechanical properties variation of AlSi10Mg with different heat treatments [95]

	0.2% proof stress / MPa		Tensile strength / MPa		Total elongation / %	
Tensile direction	X/Y direction	Z direction	X/Y direction	Z direction	X/Y direction	Z direction
As-fabricated	279	220	475	476	7.5	5.5
Annealed at 300°C for 2 h	180	175	285	290	18.6	14.2
Solution treated at 530°C for 6 h	153	139	269	245	18.3	18.1

Girelli et al. also studied various heat treatments on AlSi10Mg produced via LPBF, in comparison with a gravity casted one. They found that the best mechanical performances were obtained with a T6 treatment for both production techniques. The treatment included a solution of 540 °C for 1 hour, water quenching at 65 °C and ageing at 180 °C for 2 hours. In these conditions, the difference in properties

between the building directions was lower and the yield strength was comparable with the samples as-built. Even if the elongation was slightly lower than the as-built samples it was still higher rather than the gravity casting samples [94].

Different conditions were investigated by Li et al. who tried to understand the advantages in artificial ageing treatments for AlSi10Mg produced by LPBF. They heat treated the samples at 450 °C, 500 °C and 550 °C for 2 hours followed by water quenching. Half of the samples were also subjected to artificial ageing treatment at 180 °C for 12 hours followed by quenching. Increasing the solution temperature, the UTS and YS decreased, with respect to the as-built conditions (Figure 25). These results were associated with the rupture of the Si-network. The consequent increase in elongation was associated to the increase of size of Si particles, but also to the release of internal tension. With the artificial ageing the elongation achieved was maintained coupled with an increase in UTS and YS [96].

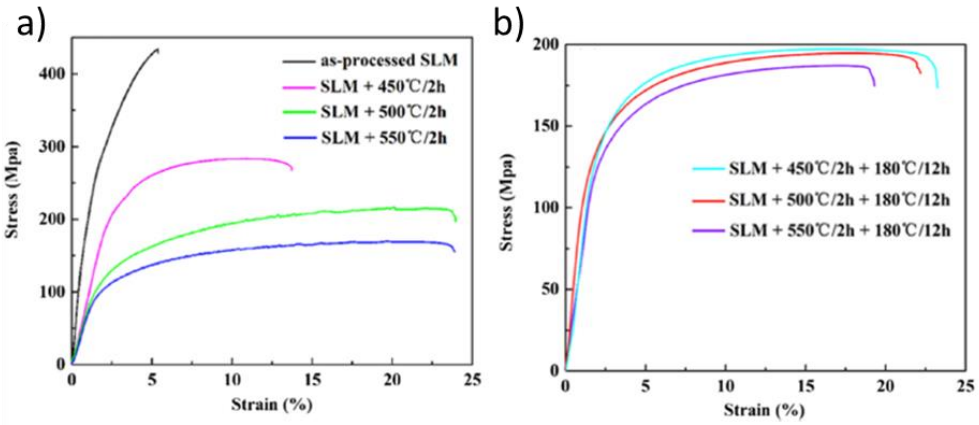

Figure 25: Tensile properties associated with solution treatments (a) and solution treatments + artificial ageing (b) for AlSi10Mg produced via LPBF [96].

1.6 Strengthening mechanism of Al alloys with specific elements

After the LPBF production, the microstructure of the components presents specific features derived from the high velocity of cooling. The post-processing treatments, such as heat treatments, are significant in improving the properties of the final components in terms of control of the microstructure and, consequently, mechanical properties.

A different approach in Al-based alloys improvement is the modification of initial composition introducing transition metals (TM) and rare earth elements (RE) [97],

[98]. In particular, the main advantages in using RE is due to the strong precipitates and stable precipitates that they form with the Al [99]. For example, the use of scandium, zirconium and erbium allows the formation of L12 Al_3X, an ordered structure which is coherent with the aluminum matrix [100]. The most famous example of aluminum alloy modified with scandium is Scalmalloy®, developed by the Airbus Group [100]. The particular microstructure and properties of this alloy was deeply investigated in different works [101].

On the other hand, as told, also the erbium forms coherent precipitates with the aluminum matrix, but the works in literature are limited, especially considering the LPBF process. One reason can be the lower solubility of erbium in aluminum with respect to scandium, leading to the inferior thermal stability of the precipitates. This could provoke the growth of the precipitates during the ageing treatments with the consequent loss of strengthening improvement [99]. For this reason, it could be interesting to investigate the effect of erbium in LPBFed aluminum alloy components in the as-built state. Gianoglio et al. studied the microstructure of Al-Er (Er 3 wt %) produced by melt spinning and LPBF. Focusing on LPBF, they found out that the microstructure resulting contained dispersion of fine intermetallic particles (Figure 26) in the aluminum matrix, which contributed to an increase the hardness [102]. To the best of the author's knowledge, no further works on using erbium as a strengthening element in aluminum alloys produced via LPBF are present in the literature.

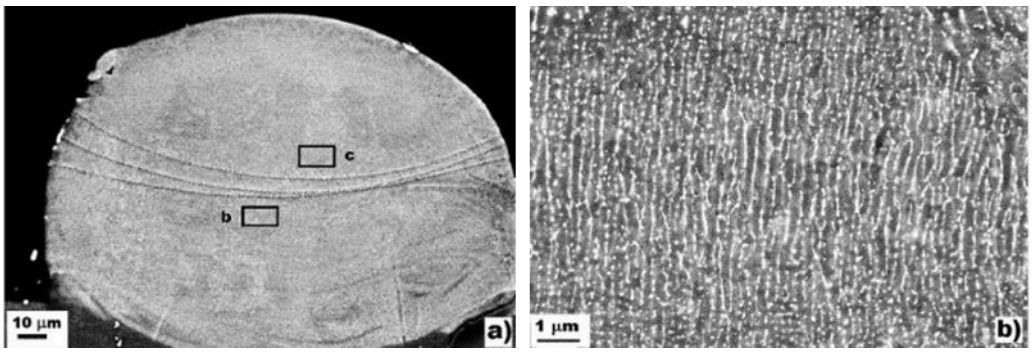

Figure 26: SEM images with backscattered detector of an Al-Er SST. In particular the images show a general overview of the SST (a) and a detail of the microstructure (b) [102].

Another element widely used in the casting process to improve the properties of mechanical alloys is the strontium. In particular, several studies were conducted to determine the effect of the strontium in Al-Si eutectic alloys [103]–[105]. It has been demonstrated that the addition of Sr in the composition of these kinds of alloys refines the eutectic silicon particles and changes the morphology of β-phases, with

a significant increase in tensile strength and ductility of the components [105]. All these works treat the aluminum alloys produced via casting, and to the best of the author's knowledge, there is no investigation of the effect of strontium in components produced via LPBF. For this reason, it would be very interesting to determine the effect of the strontium on the eutectic silicon phase after a rapid cooling process, such as LPBF, since the microstructural features of the final components are different from the ones obtained via casting.

It is clear that the adding of specific elements on the initial composition of the aluminum alloys could represent a particular way to improve their properties, avoiding further steps of heat treatment. This method can be applied to AlSi10Mg produced via LPBF since this topic it is still not investigated. It could lead to significant improvements in this alloy's mechanical properties, which has already been demonstrated to be valid for LPBF production.

1.7 Aim and tasks

All the information gathered in this Chapter points out that literature presents several works covering each step of AM production.

The gas atomization process was deeply studied concerning the different effects of the atomization parameters on the quality of the powders. Also, the process of LPBF, with a particular focus on AlSi10Mg alloy, was deeply investigated in terms of process parameters and post-treatments to obtain the best mechanical properties of the components. Finally, there are different works on modifying the Al-alloy composition with specific elements to improve the initial alloys characteristics.

But it is possible to cover all the steps of an AM process in a single work? It is possible to define and validate a system that allows to study custom alloys compositions in a reliable and fast way?

Well, this thesis aims to find it out, starting from the powder production through a laboratory-scale gas atomizer to the production of the bulk samples via LPBF. It will be demonstrated the robustness of the laboratory-scale gas atomizer with a comparison between a home-made powder and the same powder produced by an industrial supplier. The material chosen was AlSi10Mg alloy, a well-known system already widely used in LPBF. A particular focus will be given to the method of SSTs, which is very useful to define the process parameters window in this situation, thanks to its rapidity and minimal material consumption. After that, a comparison of bulk samples will be carried out to validate the quality of the powders

in terms of final densification and mechanical properties. A last step forward will be proposed to improve the properties of the AlSi10Mg by adding specific strengthening elements.

The advantages of using a laboratory-scale gas atomizer are the cost-effectiveness, since the amount of the powders which is possible to produce is limited, saving raw materials and consumables, and time-saving. A laboratory-scale gas atomizer could represent an essential step forward for developing new materials for AM and the freedom of design to modify the existing alloys to improve specific characteristics.

Chapter 2

Materials and methods

This Chapter presents all the instruments and methods used in this PhD thesis to conduct the analysis. This chapter is divided into two main sub-sections to follow the presentation of the results since Chapter 3 regards powder characterization while Chapters 4 and 5 treat optimization of process parameters and bulk samples. For this reason, the first section is dedicated to powder production and analysis, while the second one is dedicated to process parameters optimization, comprising SSTs and bulk samples production.

2.1 Powder production and characterization

This section will expose all the operative steps to perform successful gas atomization with a laboratory-scale gas atomizer. Then, a description of the main atomization trials performed to produce the AlSi10Mg are reported. Finally, there is a description of all the characterization techniques and instruments used to analyze the metal powder, the object of this PhD thesis.

2.1.1 Gas atomization: operative steps

The State-of-the-Art section gave a general overview of the Gas Atomization process, with a focus on the main steps of the process, the effect of the process parameters and the different kinds of gas atomizers available. In this paragraph, a more detailed description from an operative point of view is exposed since the technical side plays a vital role in this thesis work. The description regards the gas

atomizer used to produce the powder subject of this PhD thesis, the HERMIGA 100/10 VI Gas Atomizer, produced by Phoenix Scientific Industries Ltd – PSI, Figure 27, located in the laboratory of Politecnico di Torino, in Alessandria site.

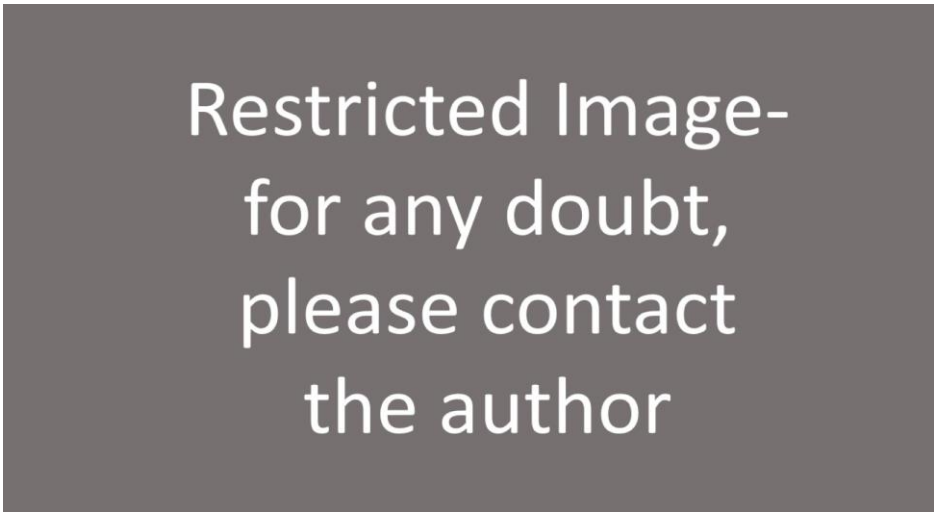

Figure 27: Schematic representation and images of the HERMIGA 100/10 VI gas atomizer in Alessandria.

The atomization process can be split into three phases, namely: **preparation**, **atomization** and **post-atomization**. The details of each step are described below.

2.1.1.1 Preparation phase

In order to better understand all the preparation steps a schematic representation of the melting chamber is proposed in Figure 28. Here all the main gas atomizer components are represented.

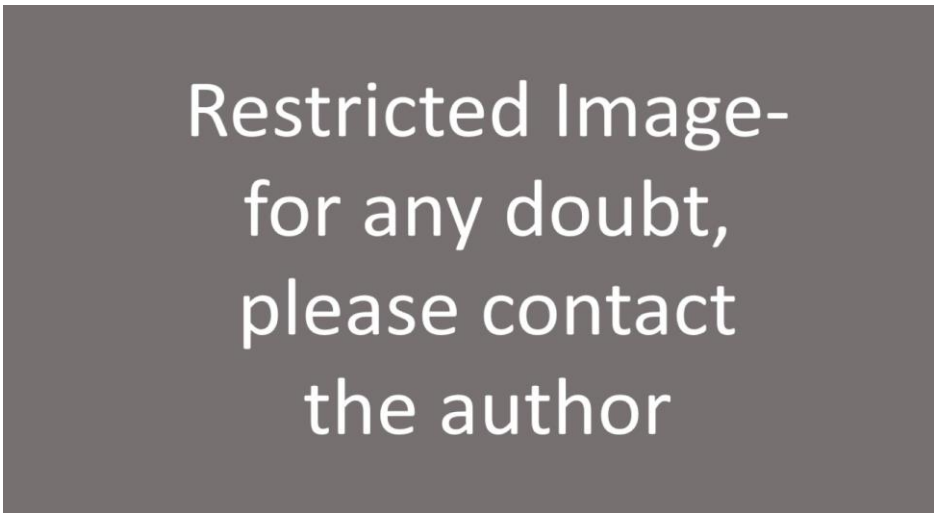

Figure 28: Schematic representation of the melting chamber with all the components.

In the preparation phase, the operators conduct all the operations required to perform the atomization process. Every operation must be carefully done in order to guarantee a successful atomization. The operations are:

- **Crucible preparation:** at first, the material of the crucible where the metal is melted is chosen. Two materials are available: graphite and alumina. In both cases, a plug with a hole (Figure 29-b) at the bottom of the crucible (Figure 29-a) is required. The molten metal will go through this hole during the atomization. In the case of the graphite crucible, the plug has a thread which matches the bottom of the crucible. Before the matching, a special glue is applied to the thread to avoid eventual metal leakages during the melting phase. The alumina crucible requires a different procedure to resist the elevated temperatures reached during the melting phase. First the crucible must be "washed" internally with a solution of sodium silicate, alumina cement and water. The mixture is obtained stirring the component in a becker. The components will separate allowing the operator to use the deposit on the bottom of the becker to glue the plug to the bottom. Afterwards, the crucible is placed in the oven at 80-120 °C for a couple of hours. This operation is due to dry the glue and promote the degassing of the crucible, which helps decrease the time needed to put the entire atomization system under vacuum.

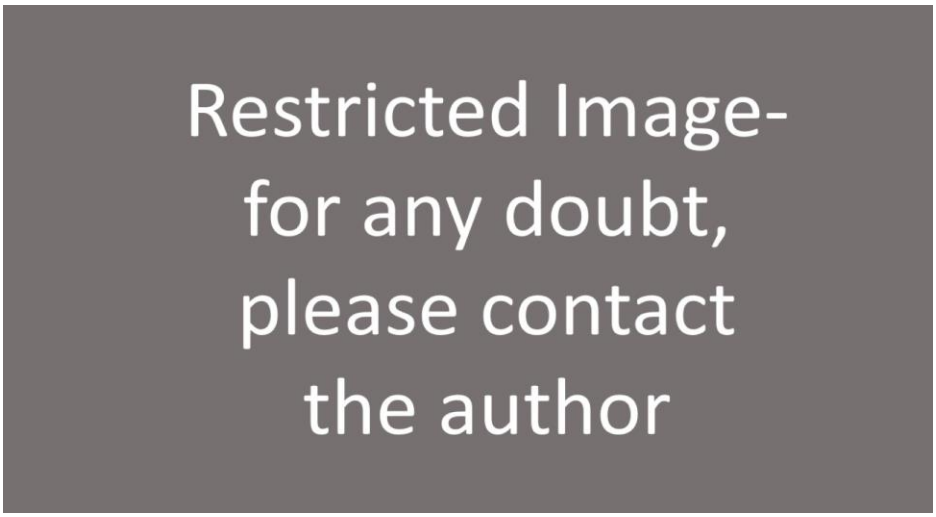

Figure 29: Bottom of alumina crucible with the plug applied (a) and a plug (b).

- **Guide tube assembly preparation:** while the crucible is in the oven (in the case of the alumina crucible), the operator prepares the guide tube (Figure 30-b). The guide tube is the system where the molten metal passes from the melting chamber to the atomization chamber. The system comprises an alumina tube with a specific diameter and a tip, which diameter can vary according to the need for atomization. The tip is made of a ceramic compound mainly composed of boron carbide. The tip is glued to the alumina tube with alumina cement and placed to dry in the same oven as the crucible. When the drying phase is completed, the guide tube is placed in a support called "guide tube assembly". This is a metallic support made of pure Mo, with some internal alumina part, which allows to control the heating of the guide tube before the atomization phase (Figure 30-a). In fact, inside the guide tube assembly, graphite springs are added (Figure 30-b). These springs make an electrical connection between the guide tube tip and the metallic support. In this way, it is possible to connect the guide tube assembly to an electrical circuit that can heat all systems by Joule Effect (Figure 30-c). This step is very important since the temperature difference between the molten metal and a cold guide tube, can provoke a solidification of the metal inside the tube, the clogging of the tip and so the failure of the atomization.

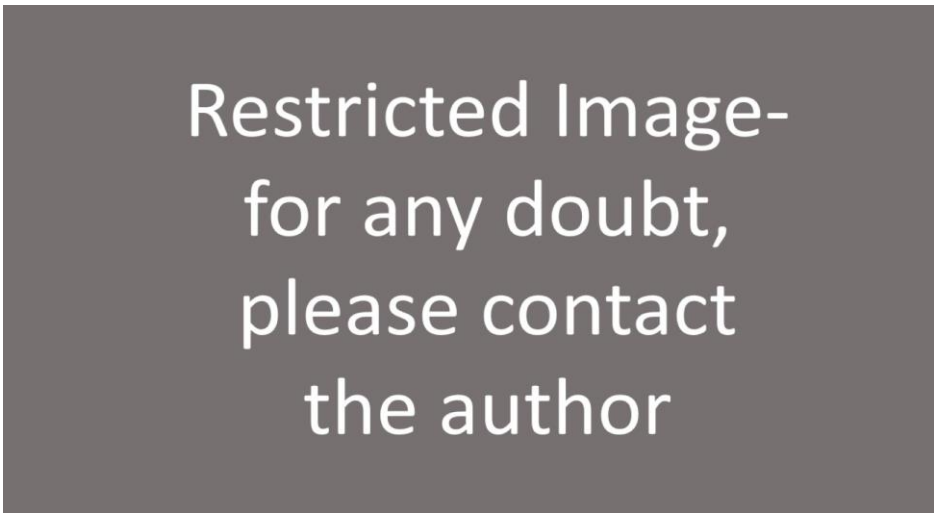

Figure 30: Guide tube assembly components (a), guide tube with graphite springs and guide tube assembly fully assembled (c).

- **Melting chamber preparation:** once the crucible and the guide tube assembly are ready, they can be placed inside the melting chamber. At the bottom of the melting chamber there is a hole where the guide tube assembly can be placed, with an electrical connection to the heating system. After that, a base of alumina is placed on the top of the guide tube assembly to sustain the crucible and match the guide tube to the hole of the plug. A cone made of porous alumina is placed between the bottom and the plug of the crucible, assuring the communication between the guide tube and crucible, also preventing leakages. Before placing the crucible, several layers of alumina components are placed in order to protect the induction coil from heat. Figure 31 represents the crucible in the melting chamber with all the refractory layers.

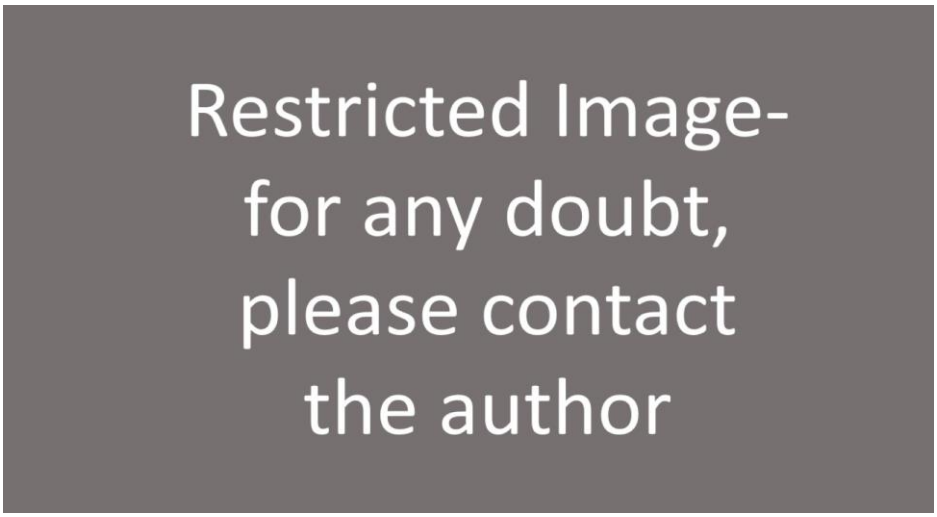

Figure 31: An alumina crucible in the melting chamber, surrounded by the refractory layers.

- **Stop rod positioning:** after the crucible is in position, the stop rod has to be placed. The stop rod is an alumina or graphite stick which matches with the plug in the crucible side. The purpose of this matching is to avoid leakages of molten metal. The matching stop rod-plug can be considered as a valve. The system that allows the stop rod movement at the exact moment of the atomization consists of a pneumatic actuator that controls a spring outside the melting chamber (Figure 28). This system is linked to a mechanical arm where the stop rod is glued and serrated by two screws after ensuring the matching with the plug. During the atomization, the actuator moves the spring, which controls the mechanical arm. In this way, the matching plug-stop rod is lost, allowing the molten metal to enter the atomization chamber through the guide tube. The temperature of the molten metal at the bottom of the crucible is controlled by a thermocouple placed into the stop rod (Figure 32). As it can be noticed from Figure 31, the stop rod is equipped with a metal shield, which protects the serration mechanism from the high temperatures reached during the melting phase.

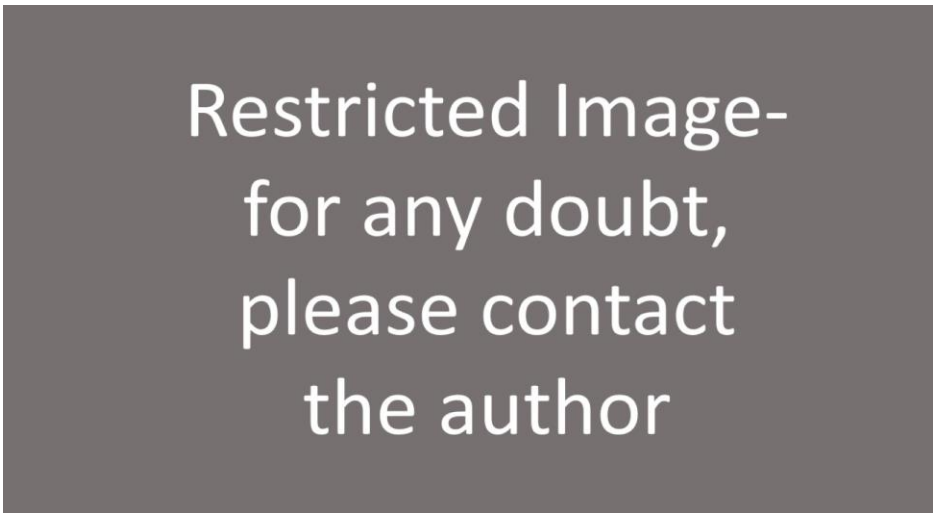

Figure 32: Stop rod equipped with a thermo-couple.

- **Material loading:** the raw material derives from ingots of controlled composition, or a mix between two or more different materials, according to the powder composition desired. The ingot is cut into small pieces that are positioned inside the crucible. This operation is carried out, paying attention to interfere as less as possible with the stop rod since the matching stop rod-plug must be preserved. The maximum load depends on the material and can be optimized by adapting the dimension of the pieces and improving the packing inside the crucible.

- **Vacuum starting:** after the crucible is loaded, the melting chamber is sealed, and the vacuum cycle can start. The vacuum is necessary to perform the melting in an atmosphere of oxygen and contaminants free, to preserve the chemical composition of the alloy. It is a significant advantage since, with this plant, it is possible to produce reactive material with oxygen. The vacuum level required to start the melting phase is around 8-9x10^{-3} bar. Reaching this vacuum level will require around 45 minutes if the vacuum pump is fully operative and the crucible was correctly degassed.

Once the system is in vacuum, the melting phase, which is the first step of the atomization phase, can start. The preparation phase requires approximately one day, considering the time of degassing and drying, the material cutting and the melting chamber preparation. The preparation phase is the most time-consuming phase of the atomization process, excluding the cleaning.

2.1.1.2 Atomization phase

The atomization phase can be further divided into a melting phase and the atomization itself.

The melting phase starts switching on the vacuum induction melting controller while the system is under vacuum. The operator can control the heating rate which must not exceed 25 °C/min by selecting the appropriate power (kW) and electric potential difference (V). This heating rate limitation is due to the risk of cracking the crucible, which is sensitive to the sudden changes in temperature. During heating, the operator controls the heating rate, adjusting if needed. It is also possible to set an automatic heating cycle. An important parameter to take into account is the matching percentage. This parameter indicates how the material inside the crucible is sensitive to induction. The higher this value, the better the ability of the material to melt. In particular, materials with high matching percentage will require low power to be heated up. It must be considered that the matching percentage value can be affected by the crucible material. In the case of graphite crucibles, in fact, the matching percentage results being very high due to its high conductivity. In this case, the effect of induction will affect the crucible and not the material inside. For this reason, the crucible will be heated by induction, while the material inside will be heated by conduction.

Before reaching the melting temperature, it is a good practice to perform a backfilling inside the melting chamber to prevent the evaporation of low-weight elements due to the high vacuum level. For this reason, the vacuum pump is switched off and argon is introduced into the melting chamber to reach an overpressure of 0.1 bar. After that, the melting phase takes place, assuring that all the material inside the crucible is melted. After that, a further temperature increase step is necessary to reach a superheat between 100 °C and 250 °C. At this point, the power of the furnace is adjusted to hold the melt at a stable temperature for a few minutes and to allow the homogenization of the melt. Now the atomization phase can start.

The first step of the atomization phase is the setting of the atomization pressure, which affects the PSD of the powder. Then the operator checks the atomization valve to understand if there is clogging in the system, which could lead to an atomization failure. After that, the top pressure is adjusted. The top pressure is the pressure applied in the atomization chamber [23]. Before starting to pour the metal inside the atomization chamber, the guide tube is heated up through the electrical system previously described. The heating time of the guide tube can be in the range

of 3-5 min. The sign that the right temperature is reached is the incandescence of the tip, which is visible by the operator through the window of the atomization chamber. At this point, the atomization can start activating the actuator, which controls the stop rod, and pouring the molten metal inside the atomization chamber. At the same time, when the molten stream is visible, the atomization gas valve is open, and the atomization itself starts. During this phase the operator can check the stream of the metal from the crucible and the "atomization cone" (Figure 33) which has to be continuous, without pulsing effect. In order to prevent the pulsing effect, the top pressure has to be adjusted, especially in the last part of the atomization when the crucible is almost empty, and the molten metal has no pushing force of its weight anymore.

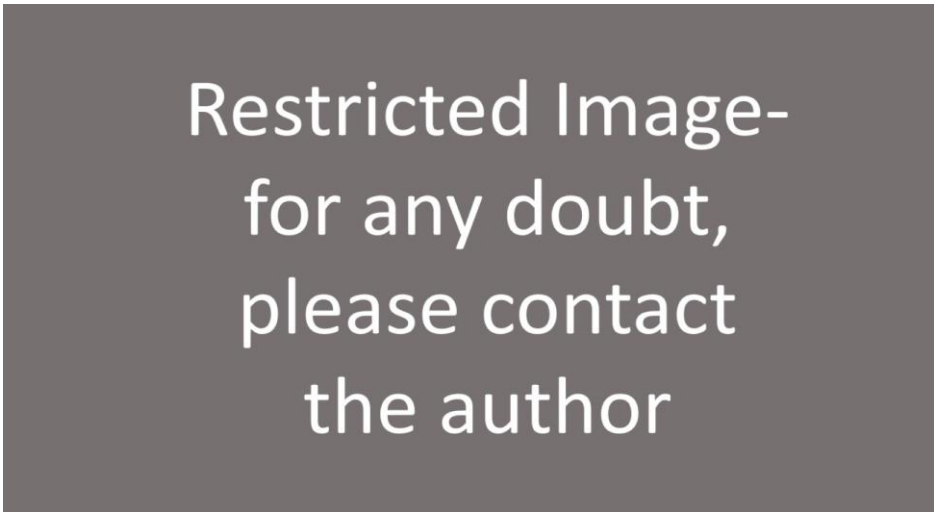

Figure 33: The "Atomization cone", captured by the camera inside the atomization chamber.

The atomization time can vary from 3 to 10 minutes according to the load of the crucible, the top pressure, the superheating etc.

Once the crucible is empty, the atomization valve is closed, and the post-atomization phase can start.

2.1.1.3 Post atomization phase

The post-atomization phase includes all the operations required to collect the powder and allows the preparation phase to start again. After the atomization, the system has to cool down to safely collect the powder and remove the used components, such as the crucible and guide tube. In the case of reactive materials

such as aluminum, passivation is necessary before collecting the powders. This step is needed because the reaction between the aluminum powder and the oxygen is firmly exothermic and might lead to a fire ignition or explosion. For the reactive powders, a procedure has been defined to safely expose the powder to oxygen, introducing a mix of oxygen and argon inside the atomization chamber and gradually increasing the oxygen percentage. This procedure allows to "passivate" the powders, creating a thin oxide film on the surface of the particles. The thickness of the oxide film depends on the increase of oxygen if it is faster or slower. This procedure must be conducted when the temperature of the system is below 150 °C to decrease the powder reactivity. Once the passivation is completed, the powder can be unloaded and ready for analysis. Regarding the atomization plant, once the temperature is around room temperature, the crucible can be removed and the guide tube as well. If the atomization did not present any problem all the components inside the guide tube assembly can be reused for the next atomization except for the guide tube itself, which presents, in the majority of cases, cracks and is clogged by the solidified metal.

Now the cleaning operations can start, including the complete cleaning of the atomization chamber, the melting chamber, the powder collector and all the components in contact with powders. This step is essential to prevent contamination in the next atomization, especially when the material to atomize is different from the previous one. After the cleaning, the preparation phase repeats all the steps already described to perform a new atomization cycle.

2.1.2 First atomization trials

The first atomization trials were necessary to define the optimal atomization parameters for AlSi10Mg to understand the yield of the process, PSD, and the powder quality. The standard process parameters are summarized in **Table 4**.

Table 4: Standard atomization parameter for AlSi10Mg

Temperature	Superheat	Pressure	Top pressure
800 °C	200 °C	40 bar	0.25 bar

Following the suggestion of Phoenix Scientific Industries Ltd - PSI, which also supplied the standard atomization parameters, the first atomization trial was performed in the graphite crucible. The graphite crucible does not require special preparation care, such as the alumina crucible. For this reason, it was a good choice for the first atomization trial in order to avoid an eventual failure caused by not correct preparation. The first comparison was made between two runs with a crucible half loaded and fully loaded to understand if there was a variation in particle size distribution and yield. The yield refers to the ratio between the weight of the raw material (ingot) and the weight of the powder collected at the end of the process.

In general, the vacuum induction melting imposes on the melt a strong effect of electromagnetic stirring, which contributes to homogenizing the melt [106]. This effect is beneficial when it needs to create custom alloys with the atomization, mixing two or more ingots from different materials inside the crucible. The electromagnetic stirring is visible as a "boiling" of the melt inside the crucible. This effect was not visible using the graphite crucible. For this reason, the third and fourth tests were performed using an alumina crucible since further studies could involve AlSi10Mg as a base for other alloys recipes. All the information regarding the first four RUNs is summarized in **Table 5.**

Table 5: Information about the first three atomization RUNs.

RUN N°	Material	Load (kg)	Crucible	Induction matching [%]	Yield [%]
1	AlSi10Mg	1.5	Graphite	200	62
2	AlSi10Mg	3.1	Graphite	200	79
3	AlSi10Mg	1.5	Alumina	80	88
4	AlSi10Mg	3.1	Alumina	80	78

From **Table 5**, it can be noticed that the graphite crucible has a matching percentage much higher than the alumina crucible, which confirms the observation about the electromagnetic stirring. There was a significant yield difference between RUN 1 and 2, which had to be investigated.

Since the atomization conditions imposed for all the RUN were the same, the recording of the atomization parameters was checked in order to understand the cause of this difference. It was found that the atomization pressure indicator signed a different value than the one imposed. The plant has two pressure sensors for the atomization gas. The first one is a gauge next to the knob used by the operator to

choose the atomization pressure. The second one is inside the atomization chamber, and it detects the atomization pressure during the atomization process. The values detected by the sensors are saved second by second and accessible through a pen drive after the atomization process. Checking these values, it was found out that the pressure value red by the gauge and by the internal sensor were different in the case of RUN 1. In fact, even for RUN 1, as the RUN 2, 3 and 4, the pressure imposed was 40 bar, defined by the operator through the knob and checking the gauge. Despite the pressure imposed, the internal sensor detected an atomization pressure of 50 bar, 10 bar higher than the one imposed. It explains the decrease in yield since a higher atomization pressure leads to the production of finer particles, increasing the amount of the particles in the secondary collector at the expense of the amount of powder in the primary collector. The yield value was consistent in the case of RUN 2 and RUN 4, where the only difference was the material of the crucible (same atomization conditions and same load).

2.1.3 Powder characterization

The powder characterization was performed on the powder produced to define the main properties. The characterization was compliant with the standard ASTM F3049-14 [107], which introduces the main techniques to characterize metal powders suitable for AM technologies. The powders analyzed were the AlSi10Mg self-produced and the commercial grade counterpart (CL31), supplied by GE additive - Concept Laser. In addition, also the powders Al3Er and AlSr were analyzed before and after the mechanical mix with CL31. Further details on this point will be given in the sections dedicated. The composition of AlSi10Mg is reported in **Table 6**.

Table 6: AlSi10Mg nominal chemical composition.

Element (%)	Si	Fe	Cu	Mn	Mg	Ti	Al
AlSi10Mg	9–11	≤ 0.55	≤ 0.05	≤ 0.45	≤ 0.2–0.45	≤ 0.15	Balance

Regarding the self-produced powder, some analyses were performed before sieving ("as run" state), while a complete characterization was performed after sieving. For the commercial powders, a complete characterization was performed as well. Before sieving, the following analyses were carried out:

- Weight of the powders, for the yield of the process.
- Volume PSD.
- Scanning electron microscope (SEM) observation with secondary electron detector.

After these first analyses, the powder was sieved with the granulometry <20, 20-50, 50-106 and >106 μm. The powder yield was calculated based on each granulometry. Special attention was given to the 20-50 μm granulometry suitable for the LPBF machine. Chemical analysis were performed to detect the presence of oxygen, nitrogen and hydrogen (ONH), for all granulometries. After that, only the "useful" granulometry was subjected to complete characterization, including:

- Volume PSD and number PSD.
- SEM observation (back-scatter detector) and energy dispersive X-Ray analyses (EDX).
- Shape descriptors analysis.
- ONH analysis.
- Rheological analyses.

It follows a description of the instruments used for the analysis of powders.

For volume PSD, a Mastersizer 3000 Malvern Panalyticak was used, while for number PSD and shape descriptor analyses, a Morphologi-4 Malvern Panalytical analyzer was used and image analysis of SEM images through ImageJ was performed. ImageJ is an open source image analysis software developed by the National Institute of Health, United States. The SEM observations were performed with a field emission gun-scanning electron microscopy (FEG-SEM) on a ZEISS SIGMA 500 and a desktop SEM Phenom pro X equipped with a back-scattered electron detector. With the same instrument were performed, the energy dispersive X-ray spectroscopy (EDX) analyses. For the ONH analyses, an ONH836 analyzer by LECO was used. In particular, three samples of 0.2 g per powder were analyzed, and the result was an average of these measurements. The same procedure with a CS844 analyzer by LECO was applied for the determination of carbon percentage of the samples. LECO supplied the program to use during these measurements to

control the heating cycle, which is compatible with aluminum alloys. The rheological analyses included flowability and tap density tests, which were carried out compliant with the respective standard ASTM B213 [108] and ASTM B527-22 [109]. In detail, the flowability was performed on three samples of 50 g per powder. A cylinder of 100 ml with 100 g per powder was used for tap density.

2.2 Process parameters optimization

This part of the Chapter comprises all the operations for the process parameters optimization, including the SSTs and bulk samples production. Particular attention was dedicated to describing the SSTs method and the script developed for the automatic analysis.

2.2.1 SSTs

2.2.1.1 Jobs preparation

In order to prepare the Jobs of SSTs, the procedure described by Bosio et al. [67] was followed. The main steps of the procedure are reported below:

- The powder was mixed with ethanol at 50 % vol to facilitate layer deposition, producing a slurry.
- The slurry was deposited on supporting disks with a diameter of 4 cm with the same powder material through a recoating system capable of controlling the layer thickness.
- The disks were heated up to 150 °C for 10 minutes to facilitate ethanol evaporation.
- The disk was placed in unique supporting platforms compatible with the LPBF machines to generate the laser tracks.

The powders used for SSTs production were Al4Cu and CL31. The Al4Cu powder was an aluminum alloy gas atomized powder containing 4.5 wt% Cu, supplied by the Universität Bremen. This powder was sieved below 50 µm and was processed using an EOSINT M270 Dual mode system. The EOS machine is an industrial-scale system equipped with a Yb-fiber laser with a maximum power of 200 W, a wavelength of 1070 nm and a spot size of 100 µm. The building platform is 25 x 25 cm^2, and the inertization of the chamber was achieved by Ar. The layer thickness chosen for this powder was 50 µm.

The CL31 powder was supplied by GE Additive - Concept Laser. The powder was sieved below 40 µm and was processed by Concept Laser Mlab cusing R. This machine is a laboratory-scale system equipped with a fiber laser with a maximum power of 100 W, a wavelength of 1070 nm and a spot size of 50 µm. The building platform is 9 x 9 cm^2, and the inertization of the chamber was achieved by Ar. The layer thickness chosen for this powder was 25 µm.

In both powders SSTs Jobs scan speed and laser powder were varied to define a proper process parameters window, producing an SST for each combination of process parameters. In Figure 34 is represented the disk with the SSTs after printing. Each "box" corresponds to a different combination of laser power and scan speed.

Figure 34: Supporting disk with a diameter of 5 cm with SSTs on the top after printing.

2.2.1.2 Image Acquisition and elaboration

The instrument to acquire the images of the SSTs was a LEICA DMI 5000 M optical microscope. For each SST, nine 100 x images were acquired to cover the entire length of the track. The images at the track edges were excluded to avoid errors in the measurements caused by border effects. In order to facilitate the post-processing image analysis, the pictures were acquired, centering the SSTs as much as possible. After gathering all the images acquired, the script can be run.

The script was implemented in ImageJ. More precisely, the script was written through Fiji, a distribution of ImageJ, which includes a compiler environment, and the language used was derived from Java script. The first step was the automatic threshold to convert the greyscale image to a binary image (black and white). The script works on the greyscale histogram of pictures to apply the binarization in the

same way for all images. This operation avoids acquisition errors and improves the reliability of the measurements. The typical greyscale histogram of an on-top SST is represented in Figure 35-a. After several tests, the script was set to detect the minimum of the curve, observing that applying the threshold at this point would achieve the best results in terms of SST border definition. After that, the images are converted to binary images (Figure 35-b).

The last step was a further conversion from a binary image to a closed profile characterizable by ImageJ in different ways. This profile is defined as a "region of interest" (ROI), and is savable with the extension .roi. A representation of a ROI is shown in Figure 35-c.

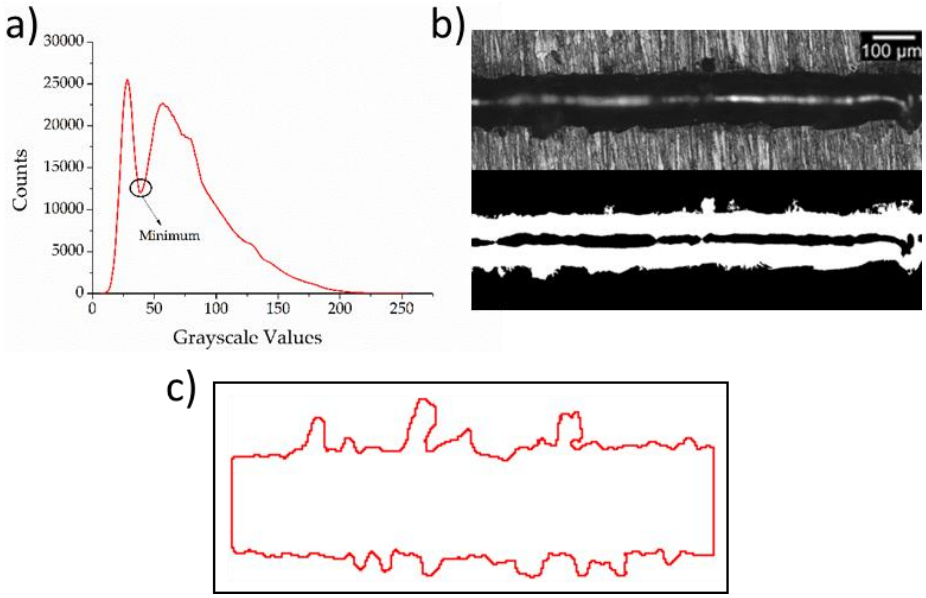

Figure 35: Greyscale histogram of the pictures and minimum definition (a), on-top SST image with binarization (b) and ROI representation (c).

The script is set with a regularity control which allows discarding the defective SSTs. An SST is classified as "discontinuous" if there is more than one image representing not closed profiles or "irregular" along the length. This situation verifies with an important melt failure (Figure 36-a) or small substrate melts (Figure 36-b). On the other hand, if the images presented a closed profile, the SST is classified as "regular" (Figure 36-c) and selected for further analysis.

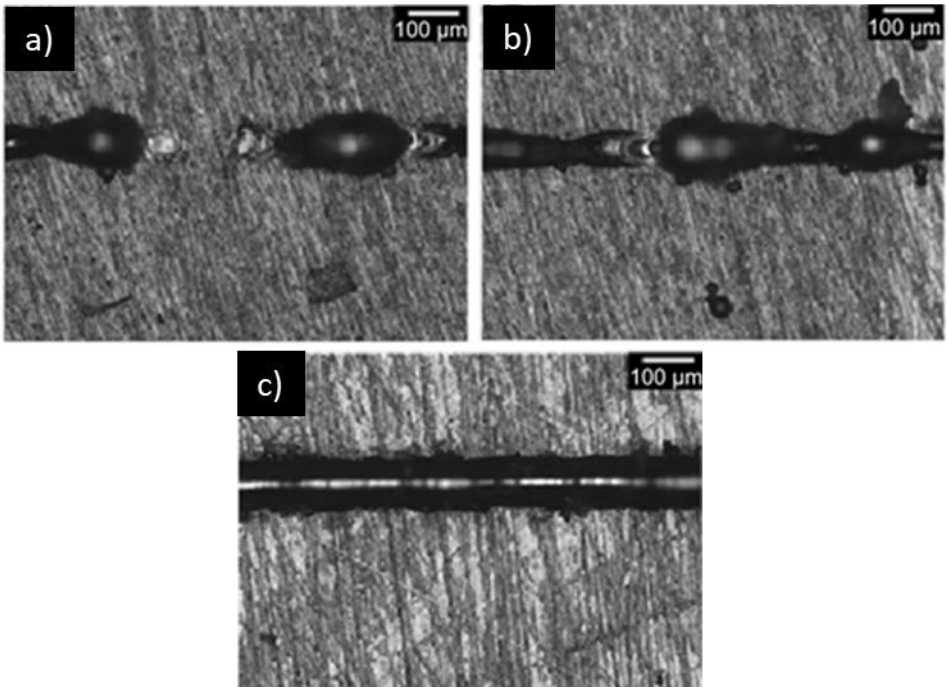

Figure 36: Optical pictures of "irregular" SSTs (a, b) and a "regular" one (c).

The script approach for the "regular" SST selection is schematized in Figure 37, where an example of the process of 400 images, representing a complete SST job characterization, is reported together with the processing time.

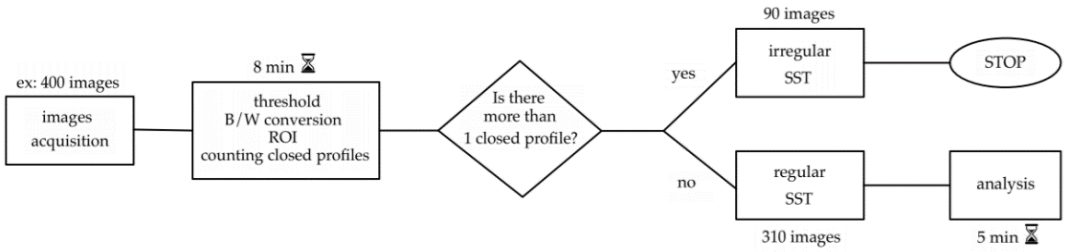

Figure 37: Flowchart of the image elaboration by the script and processing time each step

The next step represents the analysis of the ROIs of the regular SSTs by the script, which is described in more detail in the next paragraph.

2.2.1.3 Regularity Indexes

The system developed to quantify the regularity of SSTs implemented in the script is based on regularity indexes. Three different regularity indexes have been defined:

1. Perimeter index
2. Roughness index
3. Width standard deviation (STD) index

The representation of the regularity indexes is proposed in Figure 38.

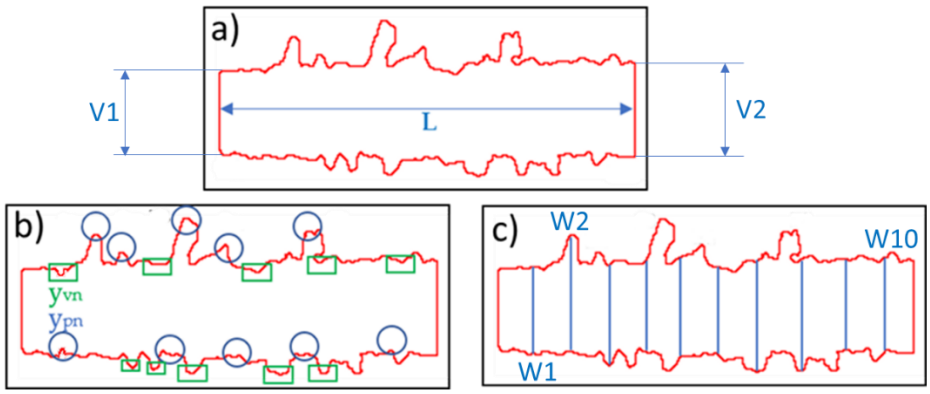

Figure 38: Representation of the ROIs indexes: the perimeter (a), is calculated by difference of the effective perimeter of the ROI and ideal perimeter obtained by the sum of 2 times the length of the ROI (2L) and the vertical segments (V1 and V2); the roughness (b), obtained by the Rz formula which considers peaks ($\mathbf{y_{pn}}$ in blue) and valleys ($\mathbf{y_{vn}}$ in green) in the upper and lower border of the ROI; the width STD (c), which considers the average of ten measurements of the width (W1,W2,…W10) of the ROI and returns the standard deviation.

The first index referred as the perimeter of the ROI, is calculated through the equation (1):

$$\text{index } 1 = P_{real} - P_{ideal} \tag{1}$$

where P_{real} is the real ROI perimeter, obtained by the ImageJ calculation and P_{ideal} is obtained as the sum of V1, V2 and 2L, following the scheme reported in Figure 38-a. P_{ideal} represents a SST with ideally regular border, associable to a rectangle, so the lower the value of index 1 the more regular ROIs borders.

The second index is associable with a roughness measure of the borders of the ROI according to the equation (2):

$$\text{index } 2 = R_z = \frac{(y_{p1} + \cdots + y_{p5}) - (y_{v1} + \cdots + y_{v5})}{5} \tag{2}$$

Where y_{pn} stands for the y-value of the n-peak and y_{vn} for the y-value of the n-valley (Figure 38-b). It can be noticed that for the upper border y_{pn} are the peaks and the y_{vn} are the valley of the border, while for the lower border is the opposite. The information returned by index 2 concerns the local linearity of the lower and upper borders of the ROI. It is clear that the lower the value of index 2 the higher the regularity of the ROI. The script evaluates the index 1 and 2 values for the different images which constitutes the SST and then the average value is calculated.

Index 3 exploits the width measurement (W) of the ROI. The script can perform ten equally spaced width measurements considering the extreme value of the y coordinates of the ROI between the upper and lower border. The standard deviation of these measurements is saved and is applied to all images of the SST according to the following equation (3):

$$\text{index } 3 = \sigma_{tot} = \sqrt{\sum_{i=1}^{n} {\sigma_i}^2} \tag{3}$$

where σ_i is the STD of the width measured on a single image and σ_{tot} is the STD of the SST width measured using all the image of the SST. In opposition with index 1 and 2, index 3 gives results about the global ROI regularity. The lower the index 3 value, the higher the global regularity of the ROI. In this step the width measurements are saved to define the hd value of the bulk samples jobs.

A schematic representation of all the procedure for indexes evaluation is proposed in Figure 39.

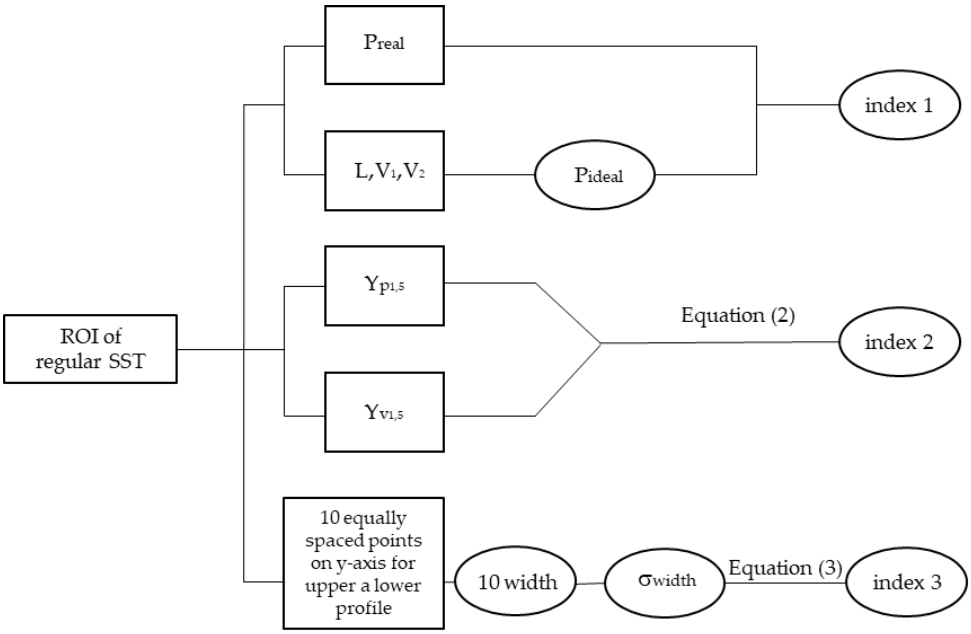

Figure 39: Flow chart to summarize the regularity index calculation.

2.2.2 Bulk samples

In this paragraph, the production and the characterization of the bulk samples of this PhD thesis is presented. Bulk samples were produced with different kind of powders:

- CL31 (AlSi10Mg).
- HM (AlSi10Mg).
- Al3Er (Er 3% wt).
- Al3Er+CL31 (Er 0.3 % wt).
- AlSr (Sr 10%).
- AlSr+CL31 (Sr 0.1 % wt).

All the powders were commercial grade except HM. This choice is because the thermophysical properties of these new compositions were yet to be available, and the atomization process was not solid enough to process them. It was preferred to perform a preliminary study on commercial compositions that were already available in the lab. In order to obtain the alloy Al3Er+CL31 (Er 0.3 % wt), the powders Al3Er and CL31 were mechanically mixed in a jar without any grinding media placed in a rotary system for 24 hours to assure a good distribution. The same

procedure was repeated for the alloy AlSr+CL31 (Sr 0.1 % wt), using the powder AlSr.

All the bulk samples were produced with the laboratory-scale LPBF machine, Concept Mlab Cusing R. The characteristics of the machine were already described in the paragraph 2.2.1.1. When in this PhD thesis work there is the reference to the "Standard Parameters" it stands for 95 W of laser power, 650 mm/s of scan speed, 105 µm hatching distance, with an "island" scanning strategy and a rotation between the various layer of 90°. The rest of process parameters are described for the various alloys. The samples produced for the basic characterization and hardness tests were cubic with dimensions 10x10x10 mm^3. For the tensile strength tests specific samples were produced, described more in detail in section 2.2.3.

2.2.3 Basic characterization

After production, all samples were divided from the building platform through Wire Electrical Discharge Machining (WEDM). After that, all the samples were cut along the YZ plane (building direction) through a cutting machine Mecatome T210 by Presi. For general metallographic observations, the samples were polished using silicon carbide papers (#600-#2400) for the grinding step and colloidal silica (0.025 µm) for the finishing operations. The porosities analysis was carried out by observing the surface of the samples with a Leica DMI 5000M and performing image analysis through ImageJ. Figure 40 represents the method of image analysis while a threshold to the image was applied to obtain a binary version of the surface observed. The porosity level was calculated as a percentage of the black area on the white background.

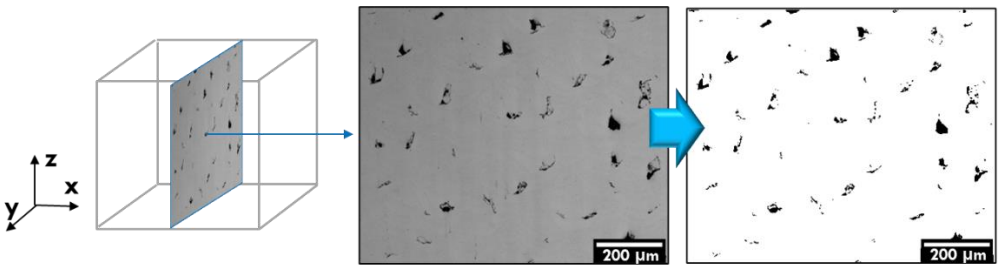

Figure 40: Image analysis performed to define the densification of the samples.

The magnification set was 100x. This magnification was chosen because it represents the best compromise regarding the smallest porosity detected and analyzed area. The same procedure was applied to define the densification of the most porous samples (AlSr, AlEr), but the images were acquired with a desktop digital microscope Dino-Lite Digital Microscope. In order to study their microstructure, the samples were etched using Keller's solution. To obtain 100 ml of Keller's solution, it is necessary to mix 1 ml of HF, 1.5 ml of HCl, 2.5 ml of HNO_3 and 95 ml of distilled water. The etching time was between 10-15 s. The etching technique applied was the drop technique, consisting of spreading a drop of etchant on the samples surface through a pipette. The microstructure was observed through an optical microscope (LEICA 5000M), SEM (Phenom ProX) and for very detailed analysis was used a Field Emission Scanning Electron microscope (FESEM) Zeiss Supra 40, with in-lens detector. The Phenom ProX was also used with the back-scattered detector to detect eventual compositional differences in the samples. EDX aided this kind of analysis.

2.2.4 Mechanical characterization

The hardness test was the first analysis performed to understand mechanical properties in the first place. In detail, micro-Vickers hardness tests were performed with a load of 0.1 kg for 15 s. Ten measurements per sample were repeated. The instrument used to perform the hardness test was a DHV-1000 digital micro-Vickers durometer. Flat samples were produced to perform the tensile tests along the XY direction (parallel to the building direction). Figure 41 shows the tensile samples on the building platform. It can be noticed that to prevent problems related to stress and distortion the samples were produced with supports. The support structure was removed by WEDM.

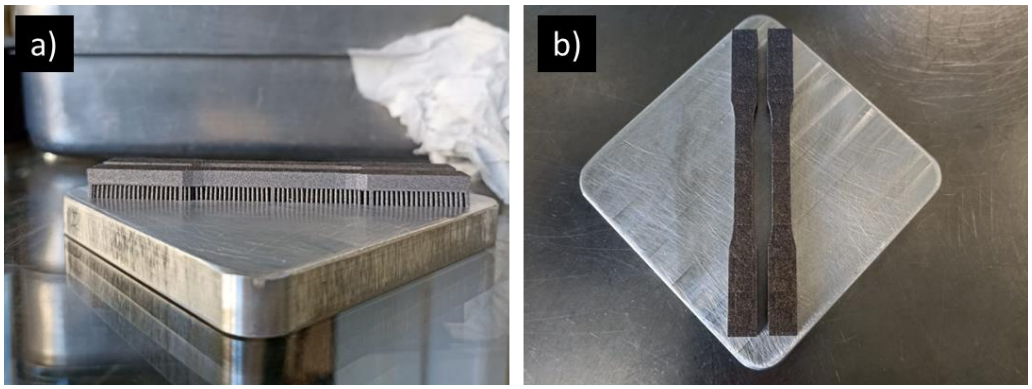

Figure 41: Side view (a) and top view (b) of the tensile samples attached to the building platform.

The testing machine used was a Zwick-Roell Z050 tensile tester. The dimensions of the samples were compliant with the standard ASTM E8/E8M [110], with a thickness of 3.5 mm and a width of 6 mm. The standard describes this kind of sample as a "sub-size" specimen. Three specimens per measurement were tested.

2.2.5 Other characterizations

The aluminum alloys with strengthening elements in the composition required additional characterizations. In order to detect the phases contained in the samples the two mix Al3Er+CL31 and AlSr+CL31 were analyzed through X-ray diffraction (XRD) and Differential Scanning Calorimeters (DSC). XRD was useful to detect the phases constituting the samples and the calculation of cell parameters. This kind of analysis was performed using a PANalytical X-Pert PRO diffractometer in Bragg Brentano configuration with a Cu source of radiation (Kα = 1.5406 Å), 40 kV and 40 mA. The setting of the machine included a step size of 0.013°, a time step of 25 s and a 2ϑ range between 30 and 100°. While for DSC analyses a Netzsch DSC 214 was used. The conditions for the tests performed included a temperature range from 30°C to 400 °C, a heating rate of 10 °C/min and the material of the crucible was alumina.

Chapter 3

Powder production and characterization

In this chapter, the powder analyses are explained. The metal powder is the raw material, the first ring of the chain of the AM technology. As explained in State of art the powder for AM requires specific characteristics that are strictly related to the final quality of the components. For this reason, it crucial to have complete control of the production process to achieve the best results possible in terms of quality and yield.

The first part is dedicated to powder analysis, with all the comparisons between the powder of the different RUNs to highlight some differences in terms of production equipment.

The second part concerns the comparison between a commercial AlSi10Mg powder (CL31) and a self-produced, “home-made”, AlSi10Mg (HM). This comparison is essential for understanding the reliability of lab-scale gas atomization, which is very useful for producing new alloys to be studied for future applications. Some data in this part were previously published in the work “Evaluation of a Laboratory-Scale Gas-Atomized AlSi10Mg Powder and a Commercial-Grade Counterpart for Laser Powder Bed Fusion Processing” [111].

3.1 Powder characterization: first atomization runs

After the powder is produced and collected, the preliminary analysis is performed, including weight to understand the atomization yield, PSD and SEM analysis. All the powders analyses performed in this paragraph cover from the first atomization trials to the final process parameters defined for AlSi10Mg. The powder analysis of the strengthening elements powders (Al3Er, AlSr and the relative mechanical mixes) will be treated separately, in the dedicated chapter. According to the particle size distribution, it can be noticed from Figure 42 that the amount of load and the material of the crucible did not affected the PSD since the curves are very similar. The PSD curves presented in all cases a "tail" for the coarser particles. This effect is due to the presence of metallic scraps in the powder collector, as it is shown in the detail of Figure 42. These metallic scraps mainly belong to the last part of the atomization process. After the gas flow is closed, some molten metal residual can still be present in the crucible. Some drops of the molten residual can fall into the atomization chamber, reaching the powder collector.

In accordance with the curves even the values of D_{10}, D_{50} and D_{90} are very similar, despite the slightly different conditions between the RUNs (**Table 7**). Only the RUN 4 showed slightly smaller particles.

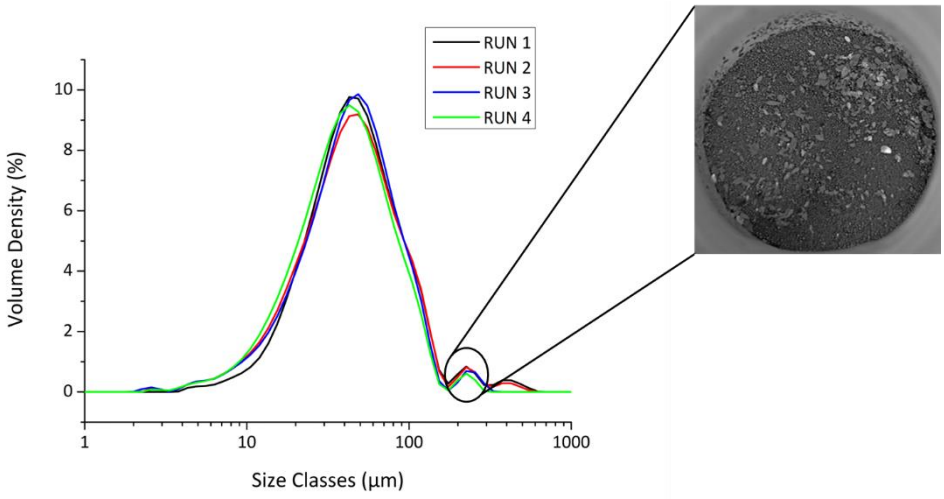

Figure 42: PSD comparison between RUN 1, 2, 3 and 4.

Table 7: D_{10}, D_{50} and D_{90} values of RUN 1, RUN 2 and RUN 3.

RUN	$\boldsymbol{D_{10}}$ **[µm]**	$\boldsymbol{D_{50}}$ **[µm]**	$\boldsymbol{D_{90}}$ **[µm]**
RUN 1	19.3	45.2	105.0
RUN 2	16.6	44.0	102.0
RUN 3	16.8	44.8	95.7
RUN 4	15.8	40.6	90.4

At the same time, SEM analyses were performed to observe the particles morphology. As can be noticed from Figure 43, all the RUNs presented similar features in terms of morphology. In every case, the powder presented a mostly spherical morphology. In the pictures at higher magnification (Figure 43-b, Figure 43-d, Figure 43-f and Figure 43-h), the surface of the particle appeared smooth and with some satellites attached to the coarser particles. In RUN 1 and 2, a global agglomeration phenomenon was not evident, except for the presence of satellites, while in RUN 3, agglomeration is more evident. Again, in RUN 4 (Figure 43-g) agglomeration phenomenon disappeared, suggesting that the cause was not related to the material of the crucible. In general, this effect is undesired since it can affect powder flowability. However, the powder has to be sieved to reach adequate granulometry for LPBF processing, which helps reduce the quantity of finer particles.

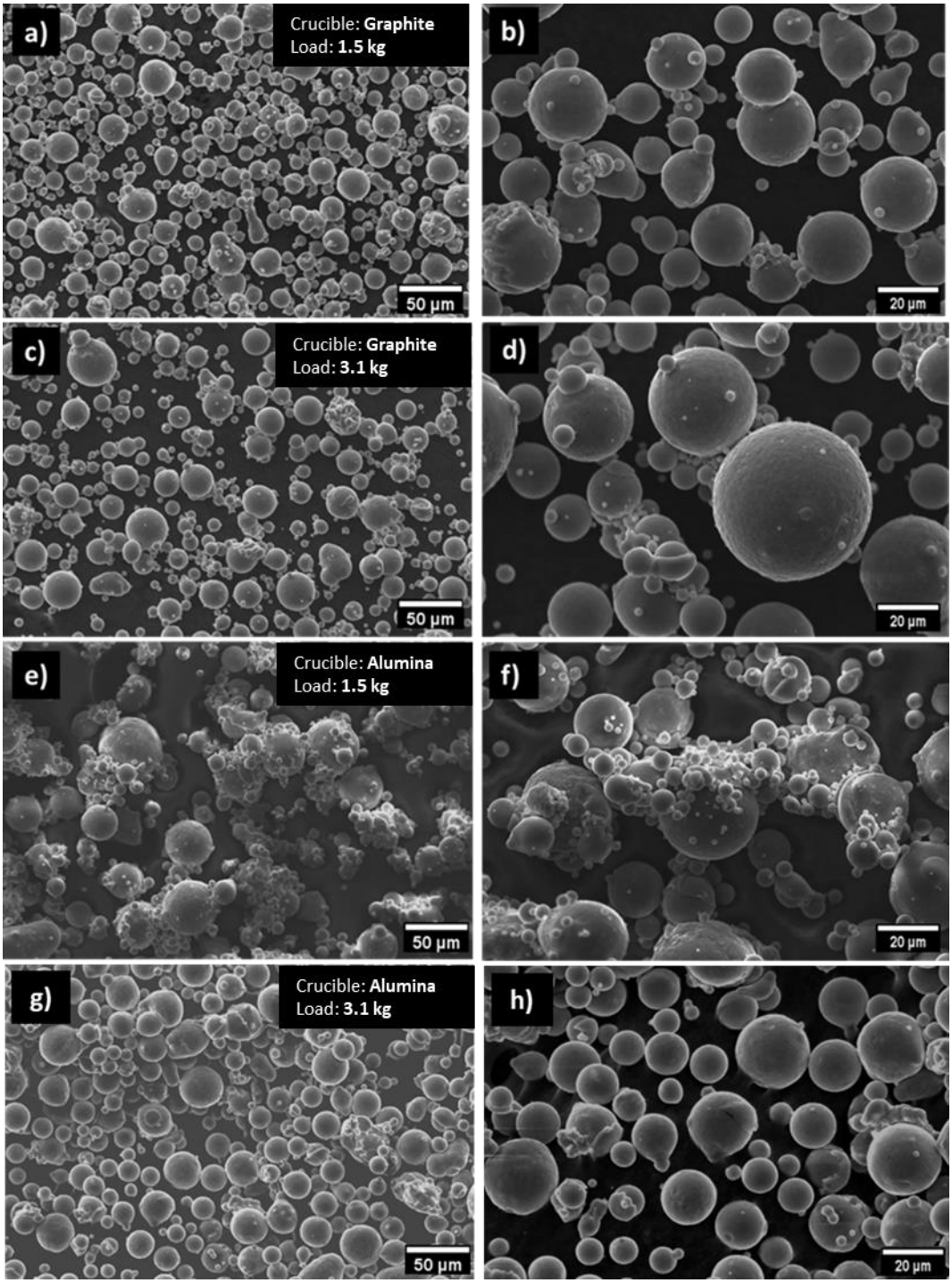

Figure 43: SEM images of the powder from the RUN 1, 2 and 3. In particular RUN 1 at 500 X (a) and 1.5 kX (b), RUN 2 at 500 X (c) and 1.5 kX (d), RUN 3 at 500X (e) and 1.5 kX (f) and RUN 4 at 500 X (g) and 1.5 kX (h).

After the first analyses, the powders were sieved in fractions <20, 20-50, 50-106 and >106 µm. This operation is mandatory because the fraction required for the LPBF process used in this thesis is between 20-50 µm. The yield of each fraction for RUN 1, 2, 3, and 4 are reported in **Table 8**.

Table 8: yield of the different fractions of RUN 1,2,3 and 4 after sieving.

RUN N °	Tot [g]	<20 [µm]	20-50 [µm]	50-106 [µm]	>106 [µm]
1	930	2%	67%	26%	5%
		19 g	623 g	242	46 g
2	2528	11%	46%	32%	11%
		278 g	1163 g	809 g	278 g
3	1320	6%	49%	38%	7%
		79.2 g	646.8 g	501.6 g	92.4 g
4	2500	14%	43%	37%	7%
		350 g	1075 g	925 g	175 g

It can be noticed that the yields were quite similar in the three cases except for RUN 1, which presented some differences with respect to RUN 2,3 and 4. The main differences are in the 20-50 µm and 50-106 µm ranges. The higher pressure imposed in RUN 1 explains the slight increase of yield in 20-50 µm and the decrease in 50-106 µm. However, this difference was not detected by the volume PSD, which was almost identical for the four batches of powders (Figure 42). As it can be noticed from **Table 3**, a high atomization pressure (50 bar) increases the yield in 20-50 µm fraction, which is helpful for LPBF production, but the total yield is decreased. Comparing the amount of powder in 20-50 µm fraction of RUN 1 and RUN 3, where the crucible was loaded with the same amount of material, it can be noticed

that a similar amount of powder was produced. This result suggests that a 50 bar atomization pressure does not cause an increase in the total amount of powder produced in 20-50 µm fraction.

There are some characteristics of the powders which are affected by the dimensions of the particles for instance the oxygen, nitrogen and hydrogen content. The results obtained from ONH analyses are shown in Figure 44. As it can be noticed the values of oxygen, nitrogen and hydrogen are quite similar for every run in every condition. The comparison was made between RUN 1 and RUN 3, in order to understand the difference in terms of material of the crucible, with equal load of material. In general, the fraction <20 µm presented a much higher level of oxygen than the other fractions. This result can be explained considering the dimensions of the powder, since a reduced dimension leads to a higher surface of interaction with the molecules of oxygen and so to an easier tendency to oxidize. It can be noticed also that the fraction >106 µm of RUN 1 also presented a high level of oxygen, nitrogen and hydrogen coupled with a high standard deviation. This effect can be explained by the presence of the metal scraps, which in these cases significantly affected the measurement respect to RUN 3.

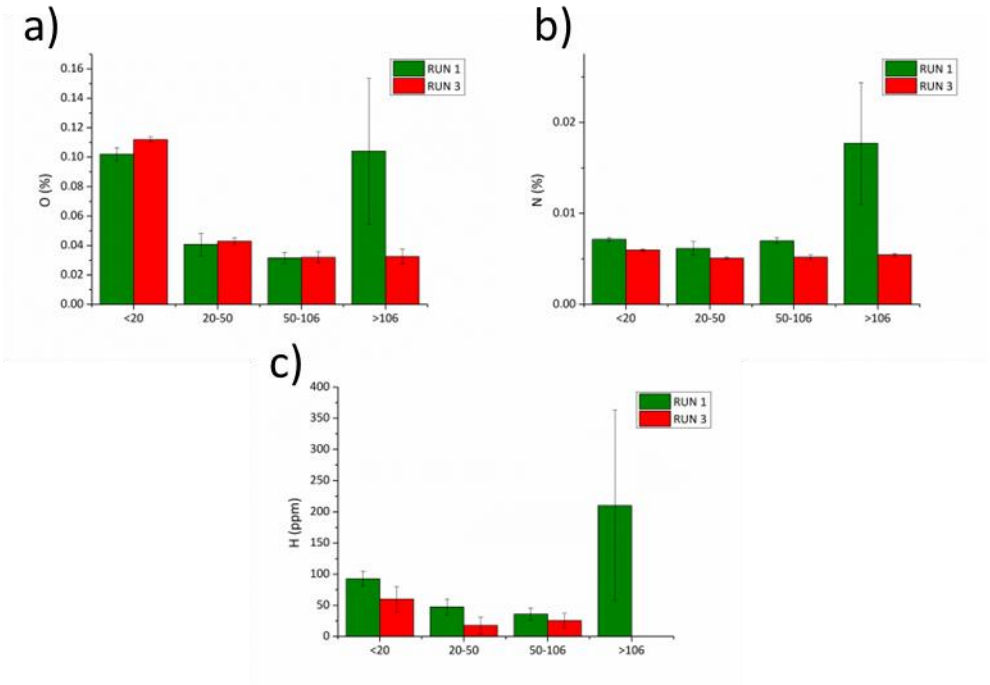

Figure 44: ONH analyses of RUN 1 and 3.

In addition, the level of carbon of RUN 1 and 3 was determined. The results are shown in Figure 45. Interestingly, the only value differentiating RUN 1 and 3 is the high value of carbon detected in RUN 1 with the fraction > 106 µm, consistent with the ONH analysis. Conversely to what was expected, using a graphite crucible (RUN 1) rather than an alumina one (RUN 3) did not affect the amount of carbon in the other fractions since a very similar percentage of carbon was detected. This result suggests that using a graphite crucible will not compromise the chemical composition of the powder.

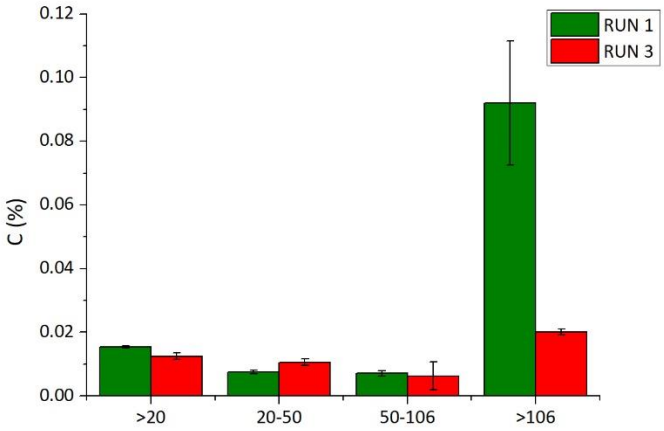

Figure 45: C percentage analysis of RUN 1 and 3.

From this moment all the further analysis were focused on the "useful" fraction, 20-50 µm. It is important to evaluate the properties of this specific granulometry, because is the one required for LPBF production using the Concept Laser Mlab machine.

The backscattered SEM images of RUN 1,2,3 and 4 powders are reported in Figure 46. This kind of analysis is useful to understand if the powder is contaminated by previous RUNs, especially if the material used was different. As it can be noticed from Figure 46-a, the RUN 1 presented some brighter particles (highlighted with red arrows), which indicate the presence of heavier elements inside the powders. In fact, the previous RUN was involving the production of 304L steel. The EDX analysis confirmed the presence of 304L, since the typical elements of these alloy were detected (Figure 47). In RUN 2 and 3, no contamination was detected, since from the RUN 1 all the RUNs involved the same material.

Furthermore, from Figure 46 it can be noticed that in all RUNs some particles finer than the sieving limit are still present after sieving. These particles are mostly satellites “welded” to the bigger ones during the atomization process. For this reason, these particles are not excluded by the sieving process. It can be noticed that the agglomeration detected in RUN 3 (Figure 43-e) was solved by the sieving step (Figure 46-c), since there are no big cluster of agglomerated finer particles.

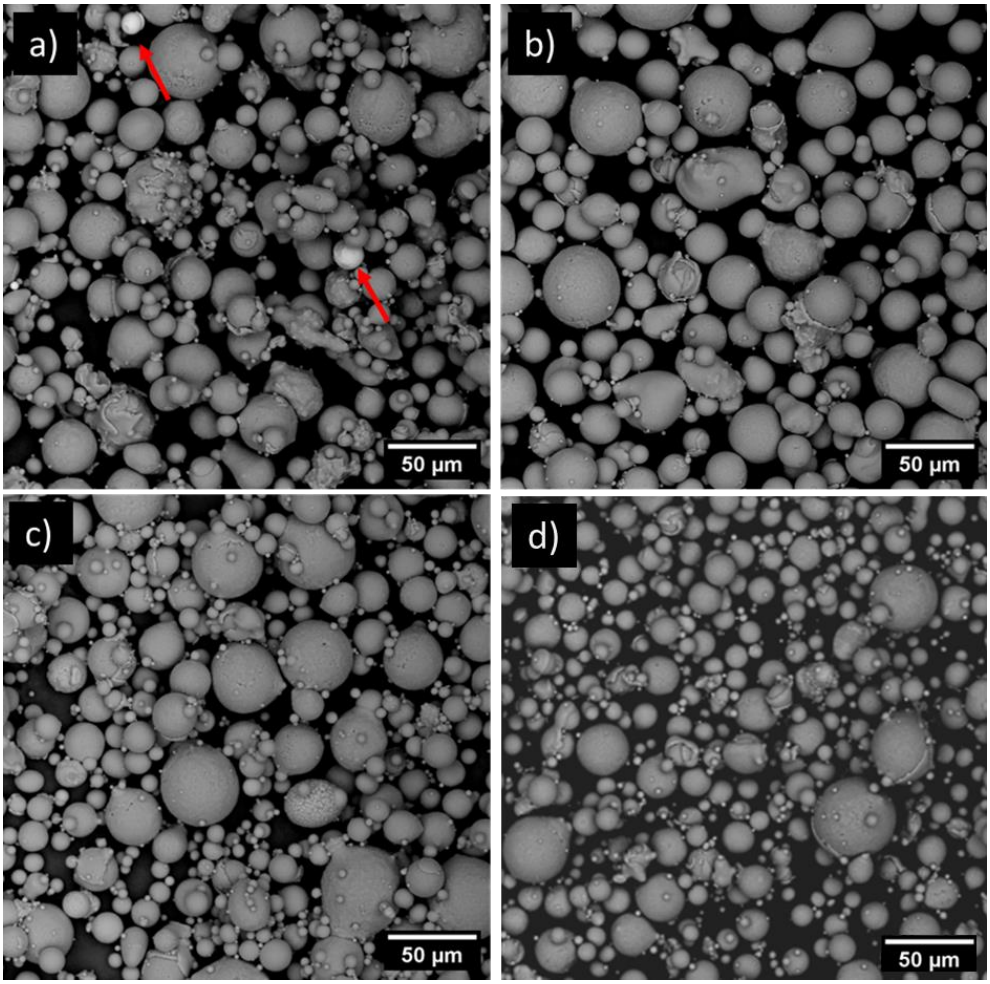

Figure 46: SEM images of 20-50 of RUN 1 (a), 2 (b), 3 (c) and 4 (d). Red arrows indicate impurity particles

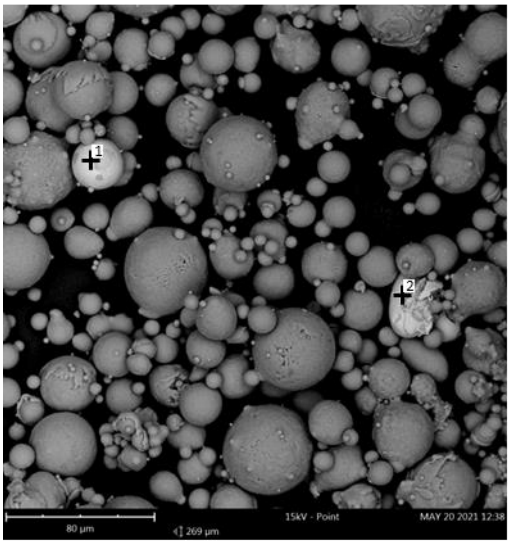

Spot 1

Element Symbol	at %	wt %
Fe	68.28	69.85
Cr	18.89	17.99
Ni	8.26	8.88
Si	2.68	1.38
Mn	1.89	1.90

Spot 2

Element Symbol	at %	wt %
Fe	70.08	71.54
Cr	19.85	18.87
Ni	6.72	7.21
Si	1.99	1.02
Mn	1.35	1.36

Figure 47: EDX analysis of RUN 1. The analysis confirmed that the white particles are steel grade 304L.

Focusing on the useful fraction, the rheological properties were analyzed including flowability, tap density and apparent density. All the three RUNs did not flow in the standard Hall and Carney flowmeters. The density measurements are reported in **Table 9**. All the RUNs showed similar values in terms of apparent density and tap density. The Hausner Ratio in all cases is below 1.25, which represents the threshold value, according to literature, of a "free flow" powder [9]. It is interesting to note that, despite a significant presence of agglomeration of RUN 3 before the sieving, the rheological behavior of its 20-50 µm fraction was similar to the other RUNs. This confirms the good efficiency of the sieving step. The best results in terms of flowability were achieved by RUN 4, since it presented the lowest Hausner Ratio. The difference between the "no flow" behavior through flowmeter measurements and the "free flow" behavior through the Hausner ratio evaluation is explained by literature. In fact, the evaluation of rheology with the flowmeters or the Hausner ratio often results in over generalization. The powder can behave differently based on the test performed since there are several factors which can influence the rheology [9].

Table 9: Rheological properties of RUN 1,2,3 and 4.

RUN	Flow rate	Apparent density [g/cm^3]	Tap density[g/cm^3]	Hausner Ratio
1	No flow	1.28 ± 0.07	1.56 ± 0.04	1.21
2	No flow	1.35 ± 0.03	1.55 ± 0.03	1.15
3	No flow	1.33 ± 0.06	1.59 ± 0.08	1.19
4	No flow	1.41 ± 0.03	1.53 ± 0.02	1.09

3.2 Comparison between commercial and lab scale powder

Once the powder analysis was completed, a comparative study between the AlSi10Mg powder self-produced and a commercial AlSi10Mg was carried out. This comparison is essential to validate the atomization process to understand if a lab-scale plant can produce powders that present the same characteristics as the big suppliers. Reaching this goal means using a plant that can produce a powder with good reliability and will open the door to studying new alloys system, which could also work in massive production and not only in experimental phases.

In order to achieve this result, a commercial AlSi10Mg (CL31) supplied by Concept Laser GE was chosen. Between the RUNs previously produced, RUN 4 was chosen for this comparison for several reasons:

- The quantity of powder produced was enough to allow the further production of massive samples (Chapter 4).
- It presented the best results in terms of rheology.

- It was produced with the alumina crucible, allowing a better melting homogenization.

The comparison was carried out on the 20-50 μm fraction for self-produced powder (defined as home-made, HM) and on as-received state for the CL31 one.

At the first place the powder was compared considering the SEM images with back scattered detector. As it can be noticed from Figure 48 a-b the powder aspect was quite similar in terms of surface quality. In both cases satellites and agglomerates were observed. The agglomerates are common in aluminum powders due to the low density and the strong interaction force between the finer particles. For these reasons, they have the tendency to stick to each other, creating irregular clusters which are easily recognizable among the majority of particles which are spherical (red circles in Figure 48 a-b). The volume PSD (Figure 48 c-d) revealed that the CL31 powder was slightly finer than HM. The values of D_{10}, D_{50} and D_{90} are reported in **Table 10**.

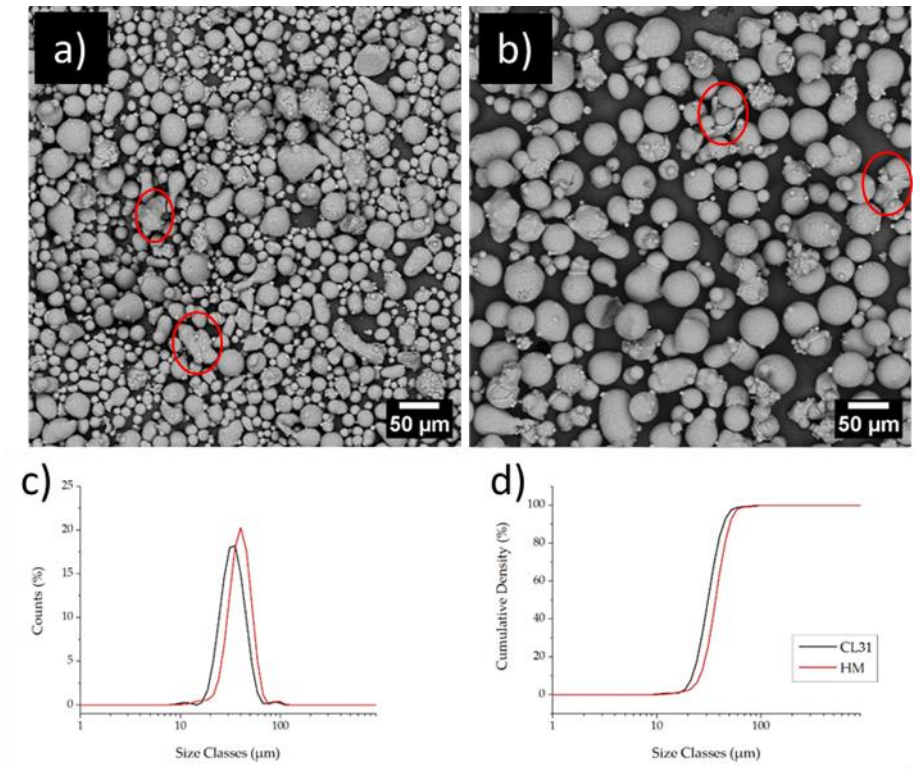

Figure 48: Comparison between SEM images and volume particle size distribution of the powders. SEM image of CL31 image (a) and HM (b) and comparison between volume particle size distribution (c) and cumulative distribution (d). Red circles indicate clusters.

Table 10: Comparison of D_{10}, D_{50} and D_{90} of CL31 and HM powder.

Powder	D_{10} [µm]	D_{50} [µm]	D_{90} [µm]
CL31	24.7	35.4	51
HM	29.5	41.8	57

To better explore the differences between the two powders, the number PSD was defined through SEM image analysis. In addition, morphological analyses were performed, using a Morphologi image analysis system. Through this method it is

possible to evaluate the presence of some morphological features using specific shape descriptors such as High Sensitivity Circularity (HSC) and Aspect Ratio (AR).

In order to have a complete overview of the PSD of the powders, a number PSD was performed too. The results between the volume PSD (Figure 48 c-d) and the number PSD (Figure 49) were not in agreement.

Regarding the number PSD there was a significant difference between CL31 and HM. In fact, the majority of particles detected in CL31 powder are in the range 5-30 µm. On the other hand, the HM powder showed a wider distribution covering the range of 5-50 µm. In addition, the CL31 powder presented a significantly higher amount of fine particles (with a mean diameter around 10 µm). This is a very interesting result which highlights the importance to consider both PSD analysis volume and number, since this difference was not clear only with volume PSD. In fact, the lower amount of finer fraction contributes to decrease the internal friction of the powder, promoting a better flowability [112]. In another work, it was demonstrated that a wider PSD leads to a high packing density of the powder bed. This fact makes possible to achieve consistently higher relative density than narrow PSD powder at lower VED applied. With an excessively high VED, the result is the opposite, probably due vaporizing of the smaller particles, which leaves voids in the powder bed [113].

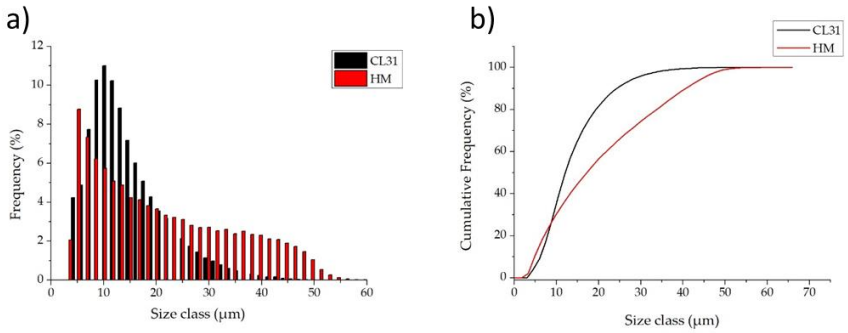

Figure 49: Number particle size distribution of CL31 (a) and HM (b).

The morphological analyses with the shape descriptors are shown in Figure 50. It can be noticed that the trends of both HSC and AR with respect to the particle dimensions are very similar for both powders. Despite of the powder analyzed a decrease in HSC and AR with the increase of particle size was observed. This effect was already reported in literature, and it is due to the different solidification times

of the particles, according to their dimensions. In fact, for the larger particles the solidification time is higher than spheroidization one, while for the finer ones it is the opposite. It follows that, it is more common to find large irregular particle rather than fine irregular ones, which are in fact mostly spherical [114]. Moving on the mean values of the shape descriptor, which are reported in **Table 11**, it can be noticed that the HSC was identical for both powders. On the other hand, the value of AR of HM was slightly higher than CL31, which suggests that the HM powder was slightly better in terms of morphology rather than CL31. In general, the mean values of HSC and AR are lower than 0.9, which is probably due to the presence of powders clusters, previously detected in the SEM analysis (Figure 48).

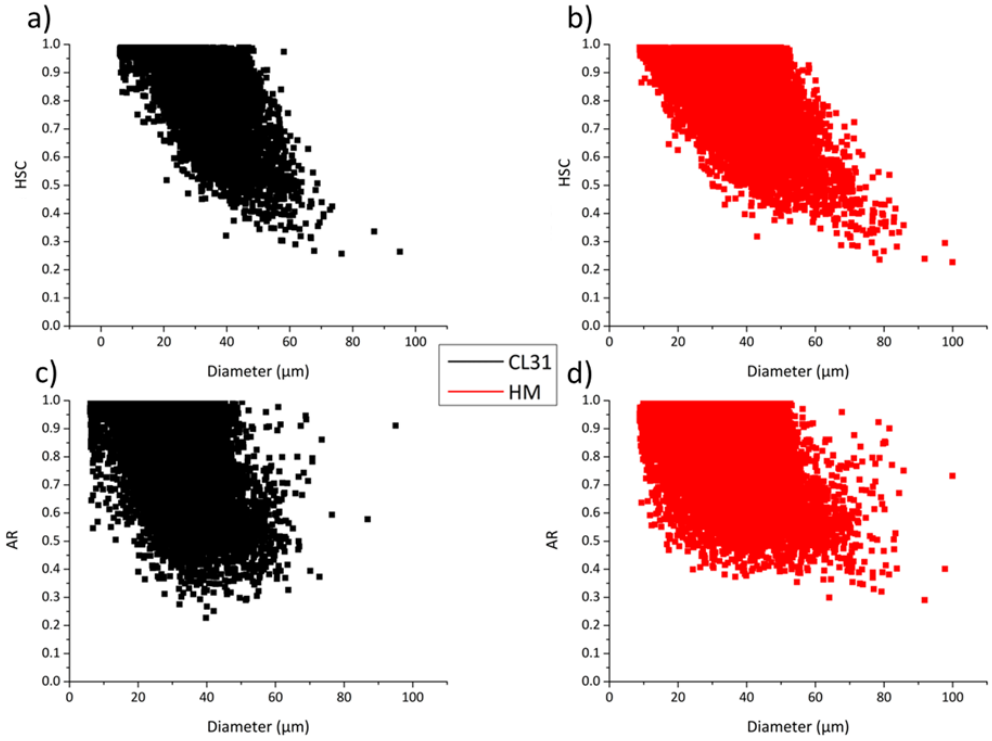

Figure 50: HSC plot vs. the equivalent diameter for CL31 (a) and HM (b) and AR plot vs. the equivalent diameter for CL31 (c) and HM (d).

Table 11: Mean values of HSC and AR for CL31 and HM.

Powder	HSC	AR

CL31	0.87 ± 0.12	0.80 ± 0.14
HM	0.87 ± 0.14	0.84 ± 0.15

After that the rheological behavior of the powder was evaluated. The results for the powder HM were already reported in **Table 9** (RUN 4). Here, the data are repeated in **Table 12** together with the CL31 ones in order to better visualize the differences. As can be noticed in **Table 12**, the higher amount of finer particles mainly affected the Tap density of CL31 powder and, consequently, the Hausner ratio with respect to HM one. In fact, the value of the Hausner ratio of CL31 is 1.14, against a value of 1.09 of HM. According to Sutton et al. the flowability of a powder with a Hausner ratio of 1.14 is classified as "good", while a value of 1.09 corresponds to the class "excellent" [9].

Table 12: Rheological values of HM and CL31.

Powder	**Flowrate**	**Apparent density [g/cm^3]**	**Tap density [g/cm^3]**	**Hausner ratio**
CL31	No flow	1.45 ± 0.02	1.65 ± 0.01	1.14
HM	No flow	1.41 ± 0.03	1.53 ± 0.02	1.09

In order to understand the differences in terms of oxidation ONH measurements were performed. As shown in **Table 13**, the oxygen, hydrogen and nitrogen content of CL31 were higher than HM. Focusing on the oxygen content, the CL31 value was further compared with the work of Raza et al. where a coarser powder of the same supplier was analyzed, with the same testing method [115]. The value obtained in the present work is consistent with the literature since the oxygen level of the present CL31 is higher than the one obtained by Raza et al., since a finer powder is more prone to oxidation due to the larger surface area.

Table 13: Results of ONH analyses of CL31 and HM.

Powder	**O [%]**	**N** [%]	**H [ppm]**
CL31	0.0878 ± 0.0159	0.00951 ± 0.0005	54.9 ± 0.942
HM	0.0287 ± 0.0007	0.00483 ± 0.0002	20.1 ± 22.7

Aluminum powders always present an oxide layer on the surface, which is formed during the passivation step. For this reason, the oxidation level of the powders could derive, at the first place, from the passivation conditions but also from successive operations such handling, shipping etc [116]. The higher oxygen level of CL31 can be explained by the fact that since it is a commercial powder it was subjected to more handling operation and shipping than HM which was produced in the lab and directly analyzed.

Chapter 4

Process parameters optimization

The lab-scale atomization plant was successfully validated in Chapter 3 through the production of a good quality powder, which is highly comparable with a commercial powder. The next step is to choose the right combination of process parameters to produce bulk samples.

As already introduced in Chapter 1, the optimization of process parameters is a procedure which can be carried out in several ways. This PhD thesis focuses on the SST method, which can be very useful when a new powder must be tested, especially when in the literature there is no baseline of process parameters to start. The rapidity and easy performance of SST makes this technique perfect for this purpose which is a critical point in new powder production and validation. However, this technique presents several drawbacks, that make the results unreliable.

The first part of Chapter 4 is dedicated to the SST method, with a study on the traditional analysis methods, highlighting the main drawbacks. After that, an alternative method is proposed. This new method can overcome the main critical issues of the SST approach and increase the analysis velocity. The main results in this part were previously published in the work “An automatic on-top analysis of single scan tracks to evaluate the laser powder bed fusion building parameters” [117]. Then, the final optimization of CL31 and HM process parameters through this new analysis method is reported.

The second part of this Chapter regards the bulk samples production of CL31 and HM with optimized process parameters. In this part are present density analysis,

microstructure and mechanical properties, intending to finalize the comparison between the powder and to understand if the powder self-produced is reliable after the production of bulk components. Part of the result of these analysis were reported in the previous work "Evaluation of a Laboratory-Scale Gas-Atomized AlSi10Mg Powder and a Commercial-Grade Counterpart for Laser Powder Bed Fusion Processing" [111].

4.1 SST: Traditional analysis of Al4Cu SST

The first SST analysis included on-top and cross-section observations of an Al4Cu powder processed using an EOS M270 Dual Mode machine. The work of Bosio et al. [66] was used as a baseline for the actual SST analysis since there a complete study of SSTs produced with an EOS M270 Dual Mode was reported. Their analyses included qualitative on-top observations of SSTs and measurements of the main geometrical features of their cross-sections.

For Al4Cu, a similar analysis was reproduced. As described in Material and Methods section, the single powder layer was obtained according to the procedure reported by Bosio et al. [66]. Several process parameters were chosen to have a complete idea of the melting and solidification behavior of SSTs with the variation of laser power and scan speed. Figure 51 represents the on-top pictures and process parameters. A color code was used to indicate the SST quality. Red indicates the SSTs which presented evident defects in terms of discontinuity or "balling" effect. For this reason, the corresponding process parameters must be excluded from the selection. In green potential suitable parameters combinations are represented. These parameters sets produce SSTs that appears smooth and regular.

Considering this first analysis, it seems that the low power combinations must be excluded from the selection probably because the energy supplied to the powder is not enough to perform a correct melting. It seems that at least a power of 160 W is necessary to obtain regular SSTs. Increasing the power (180 W and 195 W), all the scan speeds can be chosen. However, the potential good parameters are still too numerous to define a precise combination of process parameters.

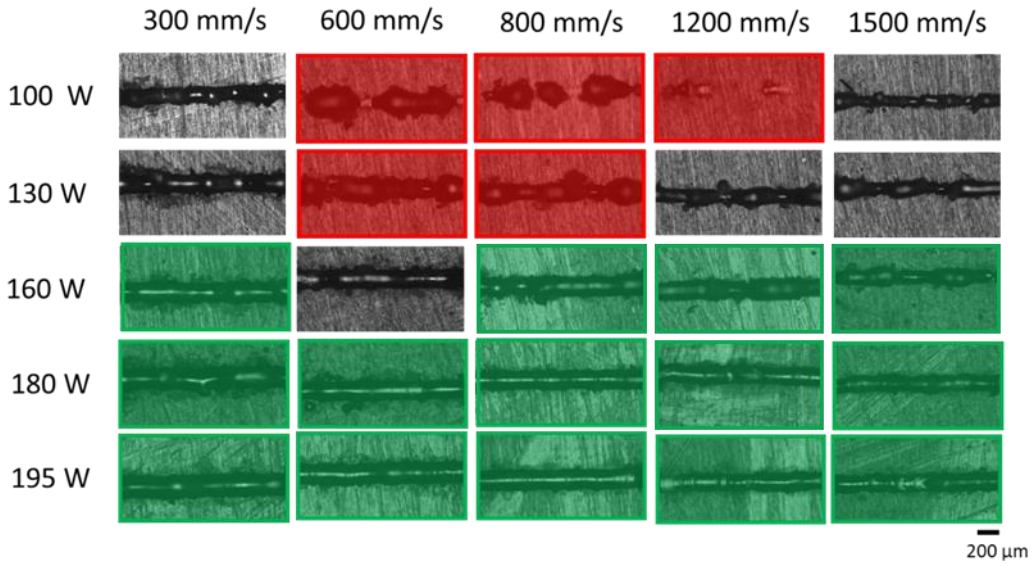

Figure 51: On-top process map of Al4Cu SSTs. Here are reported the images of the SSTs with the corresponding process parameters. In red are represented the highly defected SSTs, associated with incorrect process parameters. In green are represented the regular SSTs associated with potentially correct process parameters. The pictures not colored represent the SSTs which are borderline, not too defective, but not good enough to be chosen as correct parameters.

In order to narrow the process window, cross-section analyses were also performed. Following the same procedure as Bosio et al. [66], the cross-sections of SSTs were evaluated in terms of ratio growth/depth (g/d). As represented in Figure 52, the growth is related to the portion of SST that is above the substrate and it is related to the wettability of the powder with the substrate, while the depth is related to the penetration of the track in the substrate.

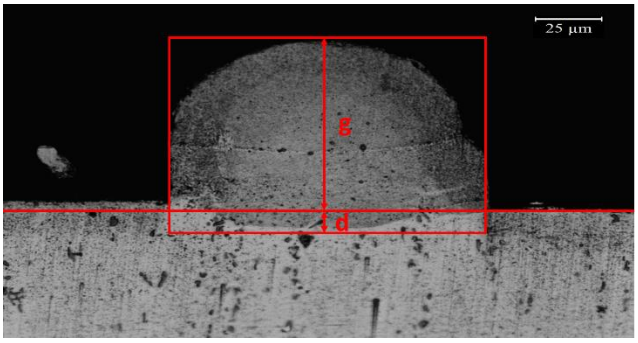

Figure 52: The growth (g) and depth (d) of a SST cross-section.

The g/d ratio can be considered a shape descriptor of the SST, and as explained by Bosio et al., the value must be around 1 to have a good balance between penetration of the melt in the substrate and the growth of the track. All the SSTs cross-sections are shown in Figure 53. The empty spaces are associated to SSTs where it was impossible to observe the cross-section, corresponding to discontinuous tracks. This result is consistent with the on-top analysis since these parameters combinations were already marked as irregular. The green pictures, instead, represent the best SST in terms of g/d, so the potential good choice of process parameters combination. As it can be noticed, even in this case, the minimum acceptable power is 160 W, which seems to be enough to produce the right g/d ratio SST, with scan speeds of 600 mm/s and 1500 mm/s. Increasing the power to 180 W the good results were obtained, with scan speed values of 300 mm/s and 800 mm/s.

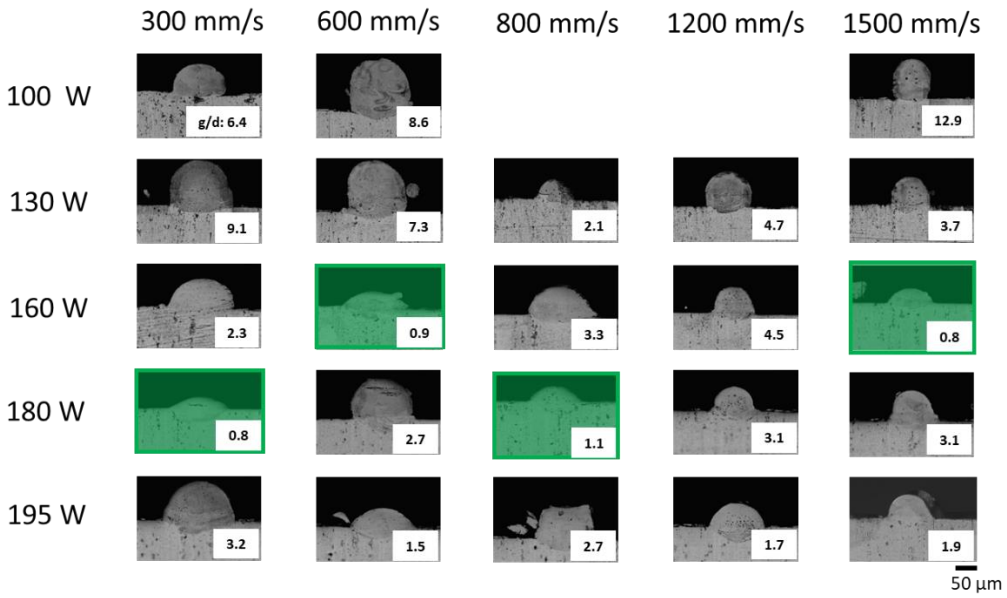

Figure 53: Cross-sections process map cross-sections, with the g/d ratio values of each parameter combination. Samples highlighted in green correspond to acceptable samples according to the g/d ratio value.

Comparing the results of on-top and cross-section analyses, it can be asserted that laser power values lower than 160 W must be excluded since they would produce irregular and defective tracks. According to the on-top analysis, almost all the speeds could be used to define the proper process parameters window. The cross-section analysis limited the choice to only four power scan speed combinations. Regarding the 160 W series, the 600 mm/s was not accepted by on-top analysis.

The series of 180 W seemed to produce two useful combinations of parameters detected in both analysis on-top and cross-section, with scan speed of 300 mm/s and 800 mm/s.

In conclusion, the SST analysis suggested that the potentially good parameter combination belongs to the series of 180 W. The consistency in results between on-top analysis and cross-section highlighted especially the exclusion of low power combination, with evident discontinuity and irregularity of the SSTs. However, detecting a trend in the results was impossible, which can suggest a lack of reliability in the measurements. In the case of on-top analysis, several parameter combinations were associated with the regularity of the border of the SSTs, probably because the qualitative analysis is not sensitive enough to detect differences between the various conditions. On the other hand, the cross-section analysis highlighted only four conditions which did not seem to follow a specific trend. This result is probably due to the principal limitation of cross-section observation which is related to the analysis of only one portion of the track, which can include measurement errors due to isolated defects.

The traditional method highlighted the benefit of SSTs in excluding unsuitable parameter combinations and to have a general idea of the proper process parameters window. However, the reliability of the technique is not high enough to precisely define the process parameters to choose due to the limited sensitivity of the qualitative analysis on-top and the analysis of a single cross-section. This last drawback could be overcome by repeating the measurement on different cross-sections of the same sample. However, it would imply a multiple-sample preparation with a consistent increase in the analysis time, which contrasts with one of the main advantages of the SST technique.

The primary purpose of the “new” method, defined as Index Method (which results are shown in the next paragraph), is to overcome the drawbacks of qualitative analysis on-top and quantify the regularity of SSTs, avoiding the cross-section method, which has shown a lack of statistical relevance.

4.2 SST: Index Method on Al4Cu

The Index Method of SST analysis is an upgrade of the on-top observation. The on-top analysis was chosen rather than cross-section because the on-top observation is the most rapid method of analysis since it does not imply a sample preparation. In addition, the main drawback of the cross-section analysis is the lack of statistical

relevance in the results since only one portion of the SST is analyzed per sample preparation. This could lead to misleading results since the only section analyzed could not represent the entire SST.

As already explained in Chapter 1 and highlighted in the previous paragraph, the main drawback of the on-top analysis is the qualitative results since the quality of SSTs is evaluated only based on the operator' s observation, without quantifying it. This implies misleading results and a lack of reliability since the results can change based on the operator who performs the analysis.

The Index Method is based on an image analysis script, which quantifies the quality of SSTs through regularity indexes. Through these indexes, it is possible to define the quality of the SSTs without the operator's subjective influence.

As explained in the Materials and Methods section, the script can extract the contour of a SST as a ROI and analyze the ROI properties to define the regularity index values. The Al4Cu SSTs were analyzed to understand the Index Method potential. In this way, it was possible to outline a direct comparison between the traditional method and the Index Method.

4.2.1 Quantitative and automatic: the main improvements of the Index Method

As previously mentioned, the first improvement given by the Index Method is the possibility to express the regularity of the SSTs borders through the regularity indexes. These represent a value that quantifies the regularity of SSTs and makes a possible comparison between the different process parameters. As described in the Materials and Method section, the regularity index is an expression of some geometrical features of the ROIs related to the regularity of the border. For instance, Index 1 derives from the perimeter analysis of the ROI.

A second improvement given by Index Method is the complete automatization of the analysis. The image analysis script is able to process entire folders of images. For this reason, the first step is adjusting the threshold parameters, which will be applied to the entire folder to process

The effect of these two main improvements is well represented in Figure 54 where results of Index 1 evaluation, obtained with automatic or manual threshold are compared.

Figure 54-a shows the measure of Index 1 obtained on images where the threshold was manually made. On the contrary Figure 54-b reports to the same measures obtained on images processed by an automatic threshold.

First, the irregular SSTs (i.e. discontinuous, defective or not measurable) are highlighted with full-scale bars with patterns. The SSTs of the series 100 W and specifically with scan speeds 600, 800 and 1200 mm/s were discarded by the software, consistently with the traditional method analysis.

It appears very clearly that, despite the use of the software to measure the ROI perimeter (Index 1), so not involving a fully manual operation, the results obtained with an arbitrary threshold selected image-by-image by the operator and the ones obtained through an automatic threshold applied to all the images, are very different.

The majority of the values of Index 1 (Figure 54-a) obtained with the arbitrary threshold are around 4000-4500 (highlighted with a black line), with a broad standard deviation. In this kind of analysis, the standard deviation represents the regularity of the border of SSTs along all the length analyzed since it is calculated on the number of images taken to represent the entire SST. A broad standard deviation is translated to an irregularity of the SST along the length, probably due to defects caused by the incorrect choice of process parameters. No trend is visible from the graph, although the condition of laser powder and scan speed are very different in some cases, significantly changing the value of the energy supplied to the material. In addition, the condition with 100 W and 300 mm/s seemed to be the best choice, since the value of the Index 1 is low and the standard deviation is narrow.

The results obtained using the automatic threshold analysis (Figure 54-b) revealed more information. First, concerning the 300 mm/s series, the high value of Index 1 and the broad standard deviation with respect to the other conditions suggests that this scan speed should be avoided. A similar discussion can be extended to the 195 W series in all scan speed conditions since the value of index 1 or standard deviation, using this scan speed, was high. The best conditions in terms of low value of index 1 were obtained with 180 W and scan speeds of 800 and 1200 mm/s. On the other hand, the same scan speed conditions with a laser power of 160 W presented a slightly higher index 1 value but with a significantly narrower standard deviation. In both power conditions, the scan speed of 1500 mm/s seemed to produce good SST in terms of Index 1 value and standard deviation.

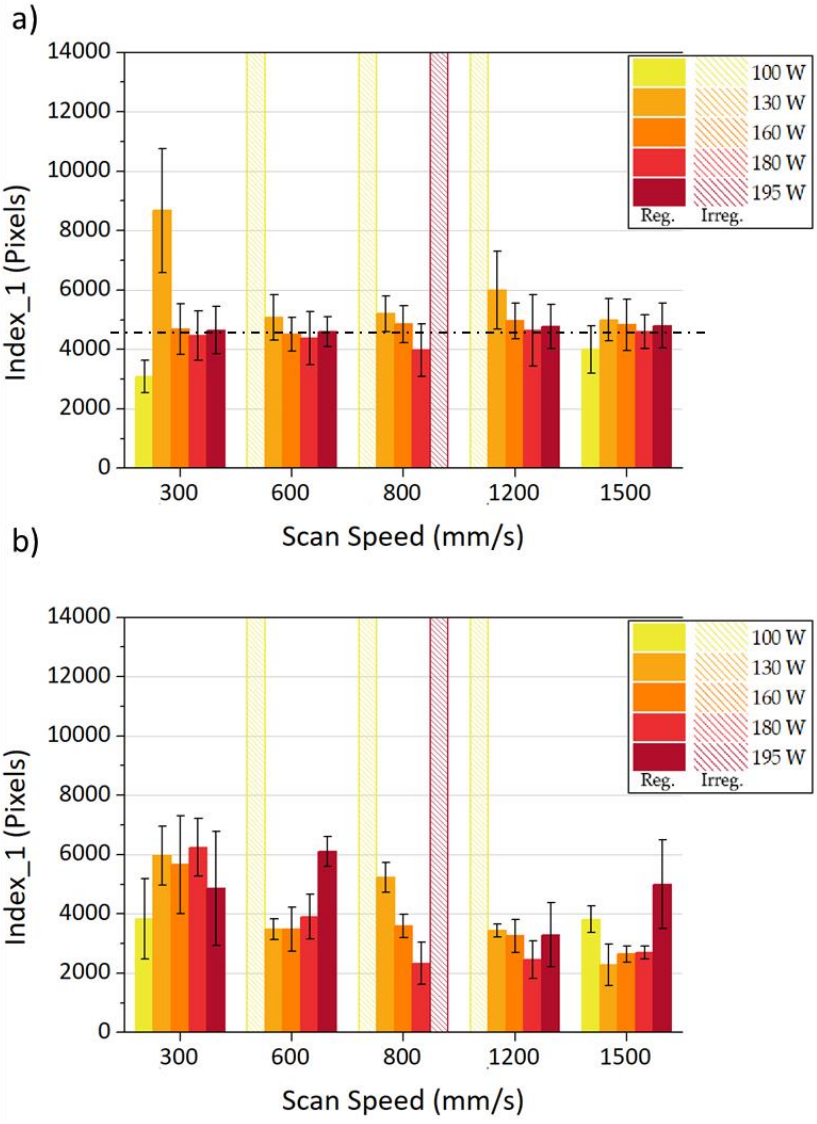

Figure 54: Comparison of Index 1 data obtained on Al4Cu SSTs images with manual (a) and automatic threshold (b). The full-scale bars with a pattern are related to the SSTs with more than 2 discontinuous regions, discarded by the script, while the dash line in the graph-a represents the mean value of Index 1 for the manual analysis.

Finally, the condition 100 W with a scan speed of 300 mm/s, in this case, presented a higher value of index 1 and a significantly broader standard deviation, which caused the exclusion of this combination of the process parameters from the final choice. To confirm this last result, in Figure 55 is presented the comparison between the condition 100 W with 300 mm/s and the condition 180 W with 800 mm/s. This last condition was promising also considering the traditional method. As it can be

noticed, the SST produced with the condition 100 W and 300 mm/s (Figure 55-a) presented irregular borders with some sputtered particles around, which suggests an incorrect combination of process parameters. On the other hand, the SST produced with a power of 180 W and a scan speed of 800 mm/s (Figure 55-b) presented regular borders and not evident defects.

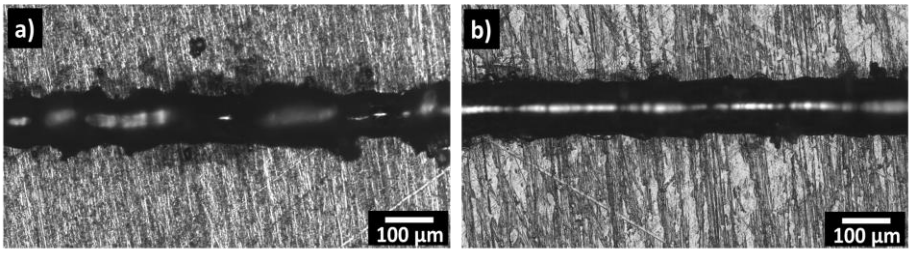

Figure 55: On-top micrographs of SST obtained with 100 W and 300 mm/s (a), and180 W and 800 mm/s (b).

4.2.2 Indexes 2 and 3

To complete the Index Method analysis also, Indexes 2 and 3 must be evaluated. As explained in the Materials and Method section, Index 2 is related to the roughness of the border of the ROI, while Index 3 indicates the standard deviation of width measurements. After comparing a manual technique with an automatic one and confirming that the automatic threshold can achieve more reliable results, Indexes 2 and 3 were evaluated for the ROIs obtained with the automatic method.

The results are shown in Figure 56. Figure 56-a displays a clear trend of Index 2 vs. power and scan speed. Index 2 value decrease with the increase of scan speed, suggesting that a too low scan speed, associated with an excessive power, promotes the formation of irregular SST. Furthermore, Index 2 data confirmed the choice of 180 W series since the lowest values of Index 2 were achieved with this power and scan speeds of 800, 1200 and 1500 mm/s. A similar result was obtained with the 160 W series, even if, in this case, the value of Index 2 were slightly higher (consistently with Index 1), considering the same scan speeds chosen for the 180 W series.

Observing the Index 3 data, a clear trend is not visible (Figure 56-b). As explained in Materials and Methods, Index 3 gives an information of the global regularity of the tracks. In this case probably, the different combination of process parameters affected the regularity of SSTs only in short range and not in long range, so the trend of Index 3 is not visible. For this reason, the evaluation of Index 3 is used

mainly to confirm the previous results or to help the choice when two conditions are very similar.

The values of Index 3 confirmed the results obtained with Index 1 and 2 for 180 W and 800, 1200 and 1500 mm/s scan speeds. On the other hand, for the 160 W series, only the scan speed of 800 mm/s was confirmed since the values of Index 3 in the other conditions resulted significantly higher.

In general, also the exclusion of the scan speed of 300 mm/s for all power condition was confirmed by both indexes. Conversely, this result was not applicable for the 195 W series since there are some values in certain speed conditions comparable with the other combinations (i.e., 195 W and 1200 mm/s for Index 2).

This last result suggests that to have reliable process windows through this method, a combination of all three indexes must be considered. Because of this reason, the parameters that were approved by all the indexes were included in the in the combination approved by the traditional method.

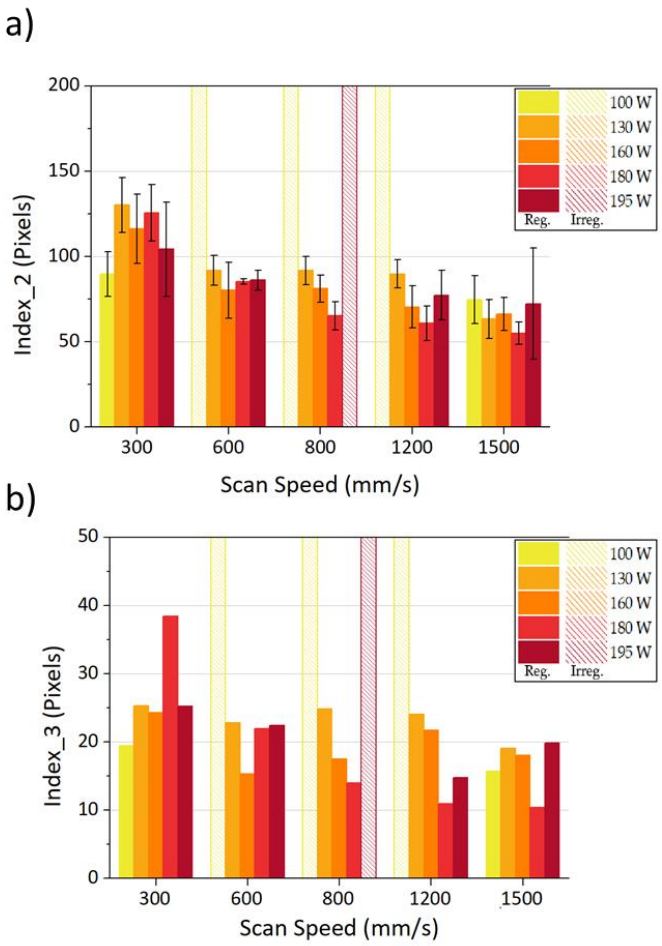

Figure 56: Indexes 2 (a) and 3 (b) of Al4Cu SSTs

The Index 1, 2 and 3 results are summarized in the process map reported in Figure 57. The comparison of the process map obtained through the Index Method with the one obtained with the traditional method (Figure 51) indicates that using the software it is possible to achieve a narrower process window. This outcome clearly underlines the advantages of the Index Method with respect to the traditional one.

Furthermore, a closer look to the process maps indicates the reason why some parameters sets could have been excluded. The power of 100 W and 130 W are probably too low to produce regular SST. Low energy supply might lead to poor penetration of the melt pool and consequent stability issues [62]. SSTs obtained with 195 W, on the contrary, have been probably excluded due to a to high laser power which can also cause issues in the stability of a track [61]. Even with the correct power, the scan speed of 100 mm/s and 300 mm/s are excluded for the same

reason, i.e., the energy supplied would increase too much, leading to defects and irregularities on the SST [63].

It is worth highlighting that these results were achieved only through the on-top observations of the SSTs, combined with a rapid automatic analysis. Avoiding the sample preparation required for the cross-section analysis and the error due to considering only one section per SST, the "new" method offers reliable results with a significant saving of time. In fact, the time of processing and generating the indexes results for an entire folder of images (around 400 images) is around 5 minutes, with a completely automatic process, as reported in the scheme in Figure 37.

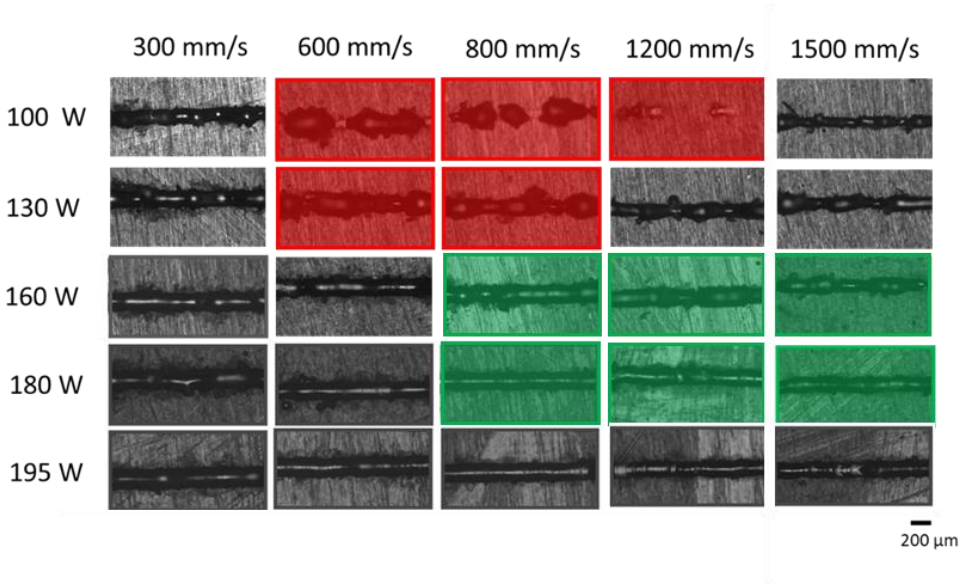

Figure 57: On-top process map defined with the Index Method.

4.3 SST: Index Method on CL31

After the reliability of the Index Method was confirmed on the Al4Cu alloy, this kind of analysis was ready to be applied to different powders. In the case of this PhD thesis, the method was further tested on CL31, using the Concept Laser Cusing R machine. To choose the process parameters combinations to analyze, the standard parameters provided by Concept Laser were used as starting point. The standard

parameters are 95 W of laser power and 650 mm/s scan speed. Therefore, the power values chosen were 85, 90 and 95 W, while the scan speed values were 350, 500, 650 and 800 mm/s.

The Index values obtained from the analyses of these SSTs are shown in Figure 58. It can be noticed that the best results in terms of low value of Index 1 (Figure 58-a) and standard deviation were obtained with the power of 95 W with a scan speed of 650 and 800 mm/s. This result was confirmed by Index 2 (Figure 58-b). Also Index 3 (Figure 58-c) of these conditions showed low values with respect to the other conditions, but here also the combination of 85 W and 650 mm/s seemed to be promising. However, this last combination showed a broad standard deviation for Indexes 1 and 2 and for this reason it was excluded from the final choice.

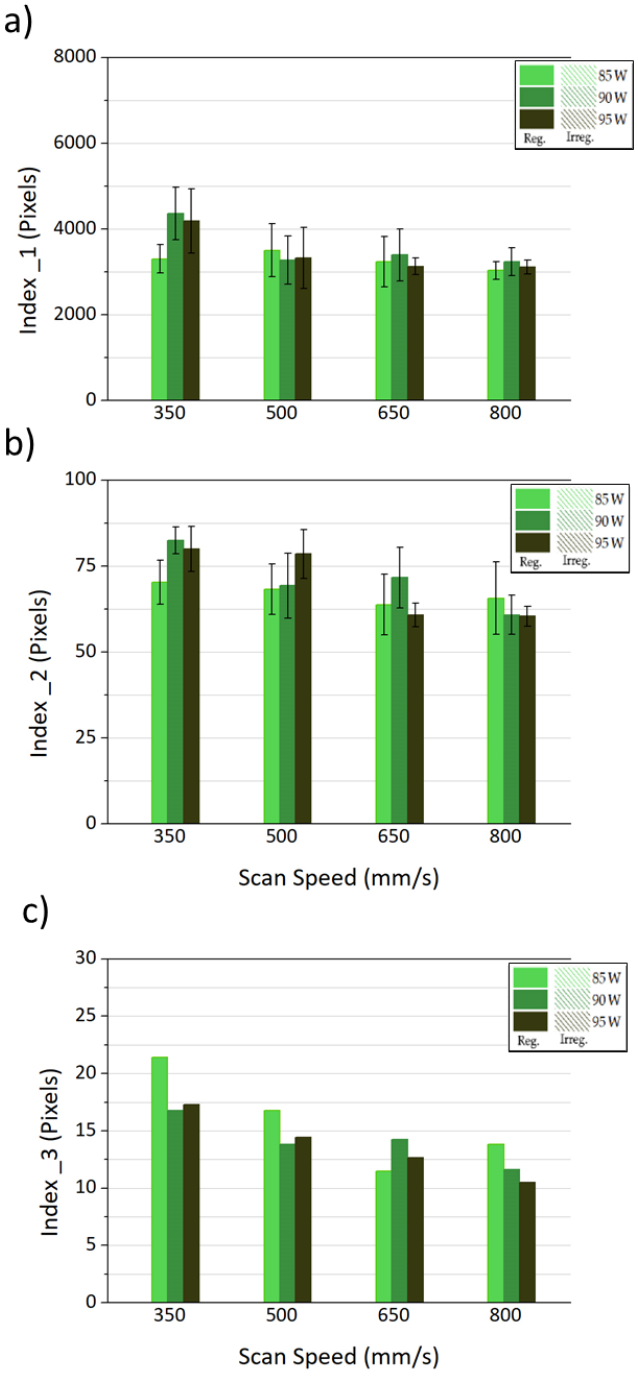

Figure 58: Indexes 1 (a), 2 (b) and 3 (c), calculated for CL31.

The results of CL31 through indexes evaluation revealed that the best choice would be the condition 95 W with a scan speed of 650 mm/s , confirming the choice proposed by Concept Laser. It is interesting to notice that even the conditions with

the same laser power but with lower scan speed, returned worse results in terms of SSTs regularity probably because of the excessive energy supplied to the material. On the other hand, all the conditions with a laser power lower than 95 W returned less regular SSTs probably because the energy supplied to the material was not enough to produce stable scan tracks.

The result of this analysis further confirmed the robustness of the Index Method. The application of the method to the Concept Laser MLab machine was more challenging because this machine does not have a robust system of platform alignment (as the EOS M270) and works with a less powerful laser. These two aspects could represent a problem in terms of stability of SSTs, but the automatic analyses seemed to successfully detect the best combination of process parameters.

4.4 Hatching distance evaluation through SSTs

A novelty in the work proposed by Bosio et al. [66] was the evaluation of SST width to define the hatching distance. In their work, the authors asserted that the laser tracks should overlap to obtain the best results in terms of densification. The optimal range of overlapping (OL) defined was 0-10 %, defined as "partially overlapped". The hatching distance (h) was calculated by the equation in Figure 59, where w is the width of the SST and φ the overlapping percentage.

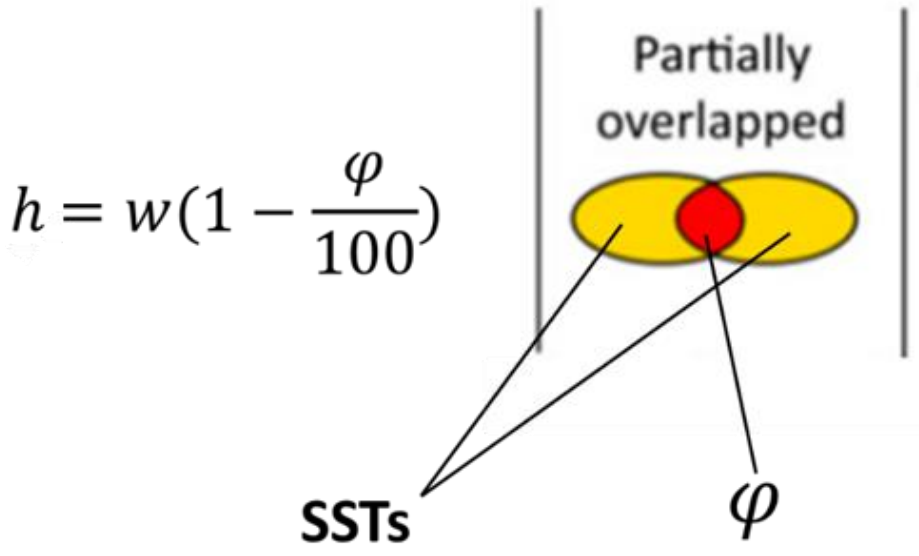

Figure 59: Equation to estimate the hatching distance (h) from the width of SSTs (w) and schematic representation of two overlapping tracks.

As explained in the material and method section, during the calculation of Index 3, the script also saves the values of SSTs widths. This last point is an improvement of the previous method, which implied a manual measure of the SSTs width. With the resulting mean width of the SSTs it is possible to estimate the correct hatching distance to obtain an OL of the tracks between 0 and 10 %. This last SSTs analysis was applied to CL31 to confirm the standard parameters provided by Concept Laser.

The results of the width evaluation are shown in Figure 60. The width value follows a visible trend as it clearly decreases with the increase in scan speed. This result is expected since a low scan speed means higher energy supplied to the material. This is translated into wider SSTs. However, following the same principle, the laser power only slightly affects the SSTs width. This phenomenon is probably due to too limited power variation between the various conditions.

Asides from these general considerations, another result is even more interesting. The width of SSTs in the condition of 95 W with 650 mm/s (standard by Concept Laser) is lower than the standard hatching distance. Concept Laser suggests in fact a hatching distance of 105 µm while the hatching distance achieved with the standard parameters was around 90 µm. This means that applying the standard hatching distance suggested by Concept Laser would lead to a negative OL value.

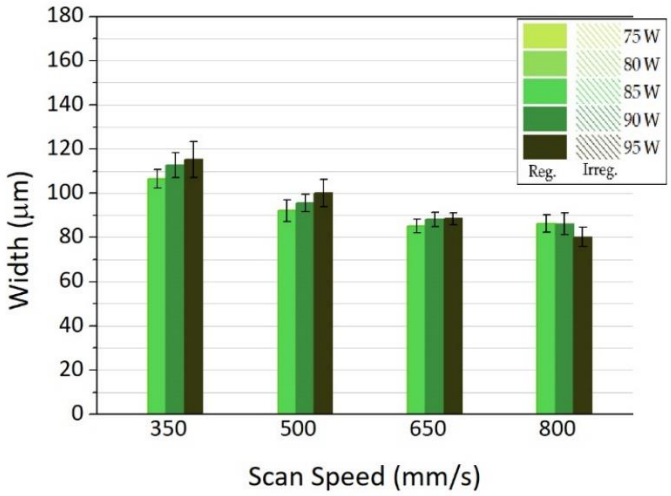

Figure 60: Width evaluation of CL31 SSTs.

For this reason, a further step was made producing bulk samples, in order to confirm if the mean width chosen by SSTs analysis was correct. The job was defined with the standard parameters suggested by Concept Laser, but with a variation of hatching distance values. It was chosen to start from the standard value (105 µm) and to decrease the hatching distances (90 µm and 80 µm) increasing the energy supplied to the material.

The results are shown in Figure 61. Interestingly, the best result in terms of porosity was achieved with a hatching distance of 90 µm. The porosity value resulting from a hatching distance of 90 µm was 0.5 ± 0.15 % while 1.2 ± 0.15 with the hatching distance of 105 µm. This result suggests that the CL31 powder needs a higher energy to achieve a better densification. This difference is probably due to the machine continuative use, which led to a partial deterioration of the laser source since the optimization of process parameters was performed by Concept Laser with a new laser source. The continuative use of a laser source causes a decrease in nominal laser power, so the real energy supplied to the material decreases with the same process parameters. Probably to supply the same amount of energy of a new laser source with the actual laser source, considering the same laser power and scan speed imposed, the hatching distance value should be 90 µm and not 105 µm anymore. The OL obtained with the hatching distance of 90 µm, is around -1 %.

According to the trend observed in Figure 61, a hatching distance of 105 µm (OL around -17%) was not enough to reach the optimal energy level needed, while 80 µm (OL around 10 %) led to an excessive increase of energy which would lead to the defects already explained in Chapter 1.

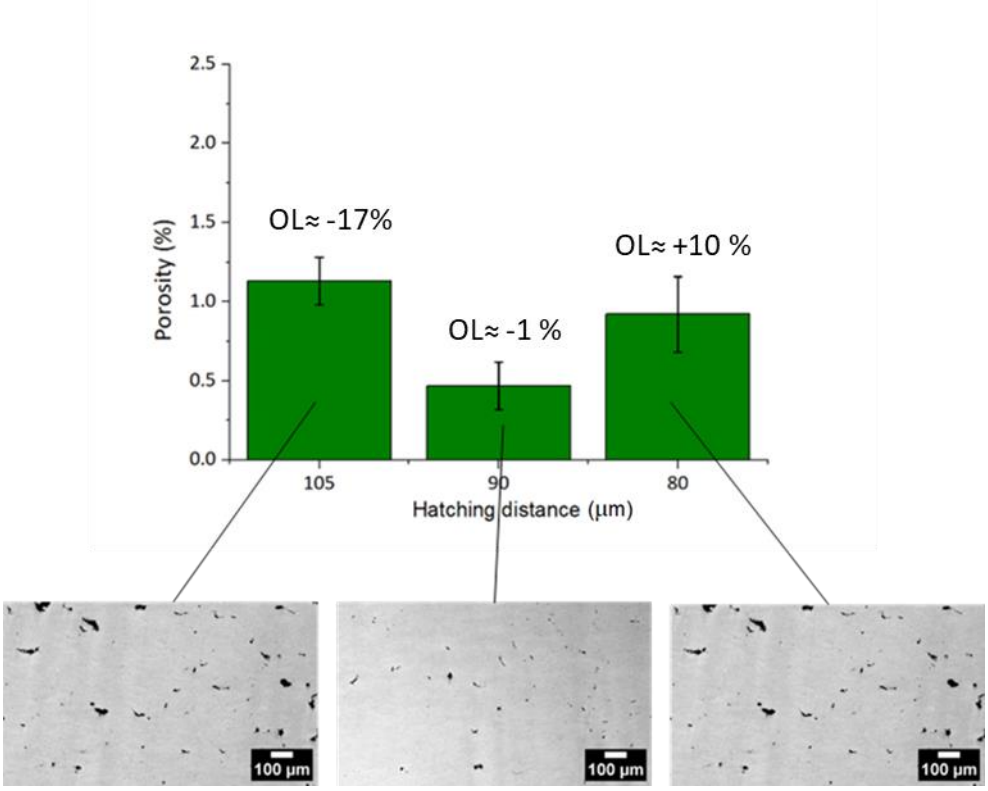

Figure 61: Porosity level of bulk samples with the hatching distance variation and the relative OL percentages. Optical micrographs of the sample's cross-sections.

The hatching distance optimization results further confirmed the usefulness of the Index Method of SSTs. In fact, the only way to detect the correct hatching distance in the past was to produce massive samples with a significant waste of material and time. With the work of Bosio et al. [66] and all the optimization of hatching distance through SSTs width and OL study, it was possible to avoid building massive samples with a considerable saving of time and material.

The Index Method represents an upgrade since all the measures are automatically performed, decreasing the time of analysis and showing that proper analysis on SST could be very useful in process parameters choice. For this reason, this method was already applied to new alloy systems which were gas atomized with the laboratory-scale plant.

In summary, the process parameters optimization for CL31 confirmed the choice of laser power (95 W) and scan speed (650 mm/s) suggested by Concept Laser, but not the hatching distance, which resulted being higher than the optimal value (90 µm).

4.5 Bulk samples comparison: CL31 vs. HM

The comparison between powder characteristics, exposed in section 3.2.2, showed that the powder properties of HM are very similar to the CL31 ones. It is necessary to study the processability of the powder via production with the LPBF machine to complete the comparison and validate the powder production through the laboratory-scale gas atomizers. In order to pursue this purpose, relative density, microstructure, hardness and mechanical properties (tensile) were analyzed. The comparison was carried out 1:1 per each property, following the same approach of section 3.2.

It was chosen to apply the standard parameters suggested by Concept Laser, including the hatching distance of 105 μm. This choice was made because the primary purpose of producing bulk samples was to compare a commercial powder with a laboratory-scale powder in terms of processability. In this sense, the essential issue is understanding if a laboratory-scale gas-atomized powder presents the same characteristics in bulk samples properties as a commercial grade counterpart with the same supplier conditions. The powder was tested by producing bulk samples in the same machine and with the same process parameters suggested by the machine supplier, which is the same supplier of commercial-grade powder. In this way also, future comparisons between different batches could be possible.

4.4.1 Relative density evaluation and microstructure

In order to determine the relative density of the bulk samples, they were cut along the YZ direction and observed with the optical microscope. The micrographs in Figure 62 show the most representative zones of the samples, for CL31 (Figure 62-a) and HM (Figure 62-b). Analyzing all the pictures per each sample the total relative density achieved for CL31 was 98.87 %, while for HM 99.17 %. These results suggest that the HM presents a slightly better processability, probably due to the lower level of oxygen, but also to the lower number of finer particles, which leads to a better powder packing.

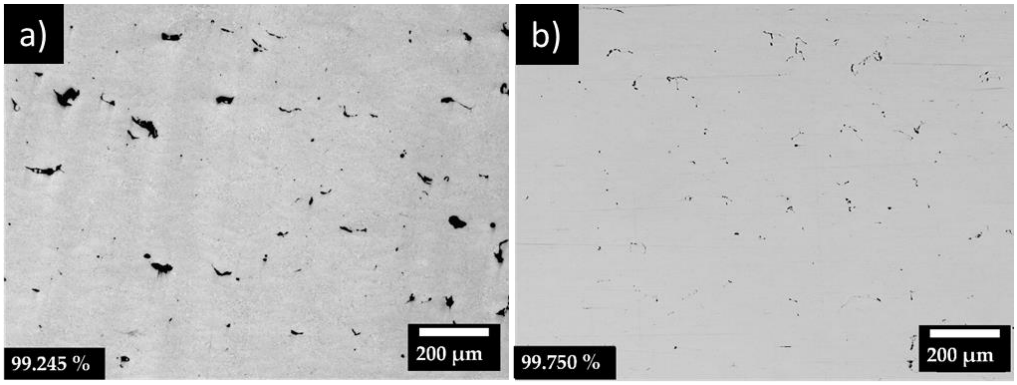

Figure 62: Optical micrographs of CL31 (a) and HM (b), XZ cross-sections. The relative density values are shown in the left bottom corner.

Regarding the microstructure, a more powerful instrument was necessary to highlight the main features. In Figure 63 the microstructures obtained via FESEM are presented. Figure 63 represents the microstructure of CL31 at lower (Figure 63-a) and higher (Figure 63-c) magnification and HM at lower (Figure 63-b) and higher (Figure 63-d) magnification. The presence of the typical AlSi10Mg microstructure after LPBF production is straightforward: fibrous eutectic silicon structure and primary aluminum cells. The complete explanation of this kind of microstructure was reported in Chapter 1. There was no difference between CL31 and HM since the pictures showed the same features for both materials.

Image analysis was performed to detect if there were differences in terms of cell dimensions. The images chosen belonged for both materials to the columnar zone. In the analysis, the width of the cells was evaluated. The mean dimension resulted in 240 ± 30 nm for CL31 against 270 ± 50 nm for HM, so no significant dimension variation was detected.

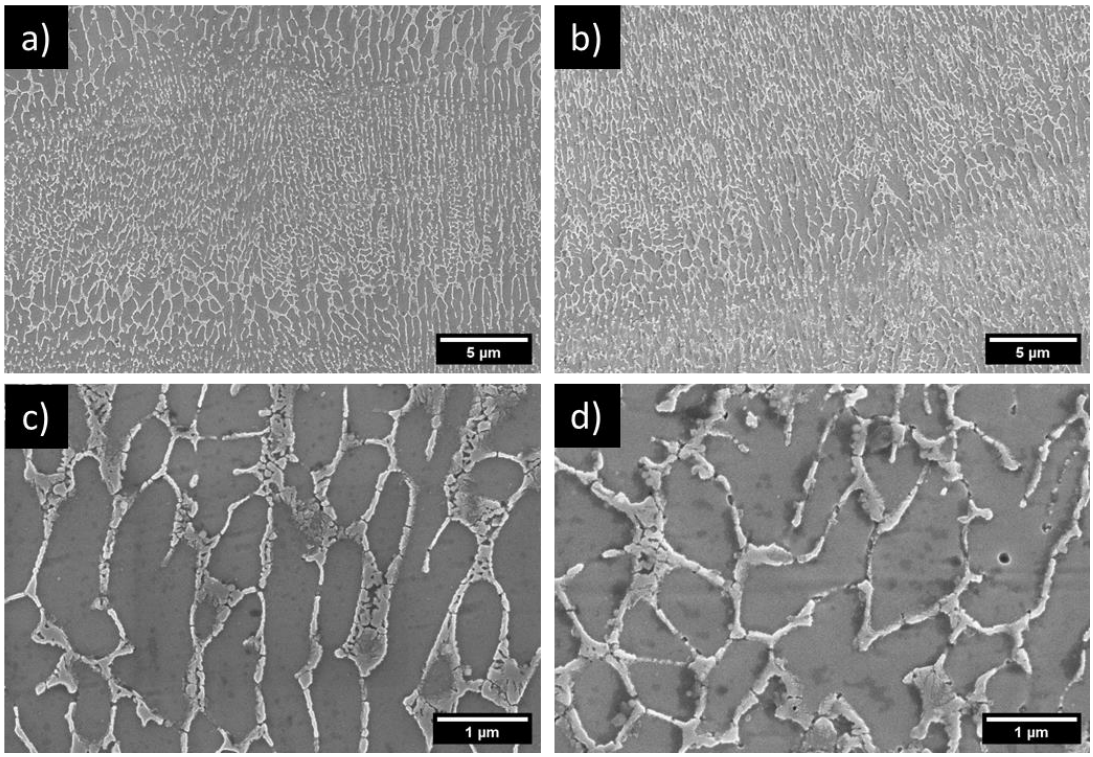

Figure 63: FESEM microstructures at high magnification of CL31 (a) and HM (b) at 10 kX and CL31 (c) and HM (d) at 50 kX.

4.4.2 Mechanical properties

CL31 and HM were tested in terms of tensile strength and hardness. The tensile properties are shown in **Table 14**. In order to confirm the reliability of the measurements, the results were compared with literature. There the tests were performed, as in this case, on AlSi10Mg tensile samples, produced along XY direction via LPBF. The value of Young Modulus was very similar to the current work, while the Ultimate Tensile Strength (UTS) was slightly lower and the and ε_{break} slightly higher [118].

In order to show directly the comparison of the properties of CL31 and HM, in **Table 14** a Δ for each property reported was added. The Δ indicates the difference between the HM property value and the corresponding CL31 mean value. It can be noticed that Δ is always a positive value, which means that the properties of HM were, in any case, slightly better than CL31. As part of the other properties, the most interesting result was achieved regarding the Yield Strength (YS) since the HM samples showed a significantly higher value than CL31. The last consideration

can be done considering the hardness which is reported in the last row of **Table 14**. Even in this case the value of hardness of HM was slightly higher than CL31. For visualization in Figure 64, are reported the stress-strain curves of CL31 and HM. Even from Figure 64, it is clear the main difference between the two materials which is the YS.

Table 14: Mechanical properties of CL31 and HM samples.

Powder	**CL31**	**HM**	**Δ [%]**
E [GPa]	65.5 ± 4.4	65.6 ± 4.2	0
YS [MPa]	286 ± 8	323 ± 14	13
UTS [MPa]	412 ± 14	422 ± 23	2.4
ε_{break}[%]	3.6 ± 0.8	4.1 ± 1.5	14
HV	135 ± 9	139 ± 5	3

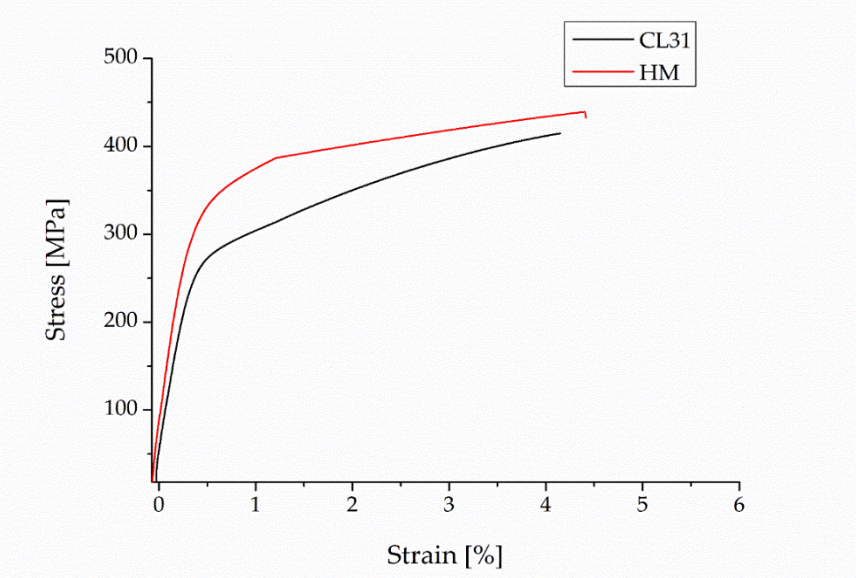

Figure 64: Representative stress strain curves of CL31 and HM samples.

The analysis of the mechanical properties was the last step of the evaluation to define the difference between the laboratory-scale HM powder and the commercial-grade counterpart. Even in this case, the powders showed very similar behavior, with a higher YS of HM powder with the respect to the CL31 one probably due to the better densification of the samples. For this reason, the processability of the laboratory-scale gas atomized AlSi10Mg can be considered as good as the commercial-grade counterpart.

Chapter 5

Modifiers elements in AlSi10Mg

The powder production and the LPBF process parameters optimization were described in the previous chapters. All the steps of LPBF were covered, reaching the point of bulk samples production of AlSi10Mg and mechanical testing. In Chapter 5, a further step forward is proposed. This step concerns modifying the microstructure and improving the mechanical properties of AlSi10Mg by adding specific alloying elements.

In this PhD thesis work, two elements are proposed: Er and Sr.

The description starts with the general powder characterization used to mix with AlSi10Mg, followed by the bulk samples characterization divided by the element used.

5.1 Powder characterization

In order to insert the strengthening elements in the AlSi10Mg, as explained in Materials and Methods section, the powders were mechanically mixed. For both mechanical mixes, the CL31 (AlSi10Mg) was used.

In order to understand how the mixing could affect the properties of CL31 powder, some preliminary analyses were conducted on the aluminum powders with the inoculant elements. Figure 65 shows the SEM micrograph of the powders, Al3Er (Figure 65-a) and AlSr (Figure 65-b).

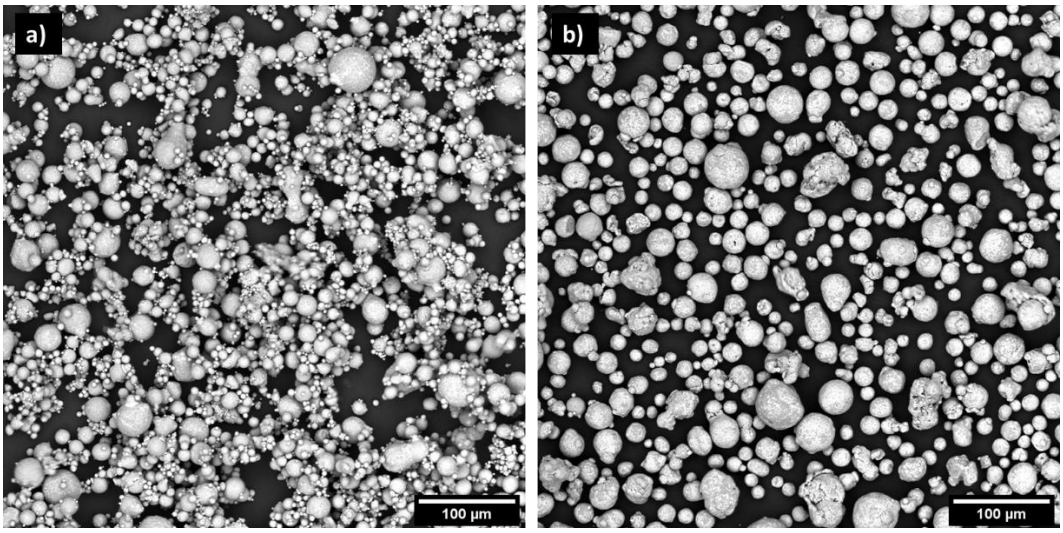

Figure 65: SEM powders images of Al3Er (a) and AlSr (b).

As can be noticed, the powder Al3Er showed a significant number of fine particles and satellites attached to the bigger particles. This could negatively affect the flowability and so the processability of the alloy. On the other hand, the AlSr powder seemed unaffected by this problem, and, despite some irregularly shaped particles, the aspect of the powder was good.

In order to have an overview of the dimensions of the particles, the SEM images were analyzed to obtain the number of PSDs. The analysis was performed on more than 30000 particles per sample. The results are presented in Figure 66.

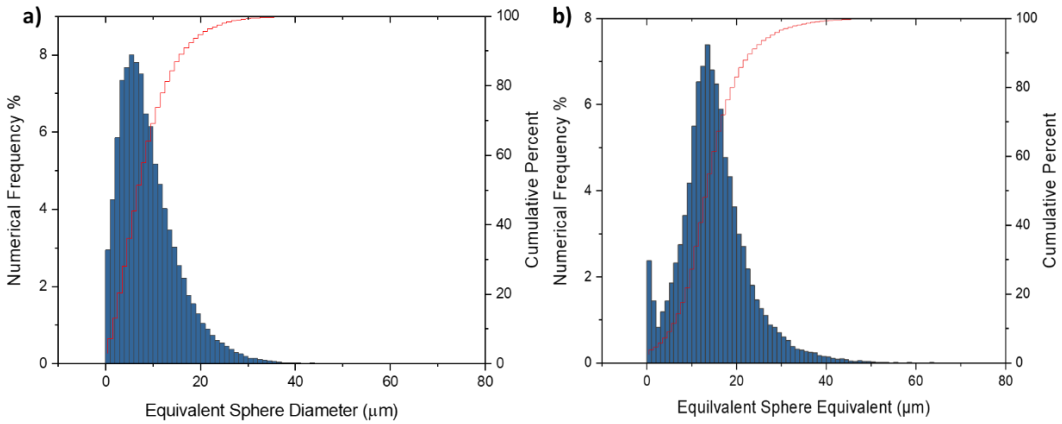

Figure 66: Number PSD of Al3Er (a) and AlSr (b). The results were achieved through image analysis of the SEM images.

As can be noticed, the Al3Er number PSD (Figure 66-a) is shifted to finer dimension rather than AlSr (Figure 66-b) due to the presence of a significant amount of finer

particles, confirming the consideration of SEM observation. In fact, the D_{10} , D_{50} and D_{90} of Al3Er were respectively 2.3, 7.4 and 17.5 µm against 6.1, 13.8 and 24.1 µm for AlSr.

The next analysis concerned the rheology of the powders in order to understand the behavior during the spreading phase in the LPBF machine. The results of the test are presented in **Table 15**.

Table 15: Rheological properties of Al3Er and AlSr.

Powder	Flowrate	Apparent density [g/cm^3]	Tap density [g/cm^3]	Hausner ratio
Al3Er	No flow	0.87 ± 0.01	1.29 ± 0.01	1.47
AlSr	No flow	1.30 ± 0.01	1.55 ± 0.01	1.20

Both powders did not flow according to both Hall and Carney tests. The Hausner ratio of Al3Er was 1.47, which is defined as “Very poor/cohesive” by the classification of Sutton et al., while AlSr, with a value of 1.20, is defined as “Fair” [9]. As expected, the massive amount of fine particles of Al3Er was significantly detrimental to the flowability of the powder. This could lead to problems in mixing with CL31 and successive spreading in the LPBF machine, resulting in no optimal densification of the samples. On the other hand, the rheological properties of AlSr are comparable with CL31, which means that good mixing and good flowability after the mix were expectable.

In order to avoid the effects of agglomeration during the process, both mixes of powders were dry in an oven at 120 °C for 3 h. In Figure 67 is shown the building platform with the powders spread on the surface.

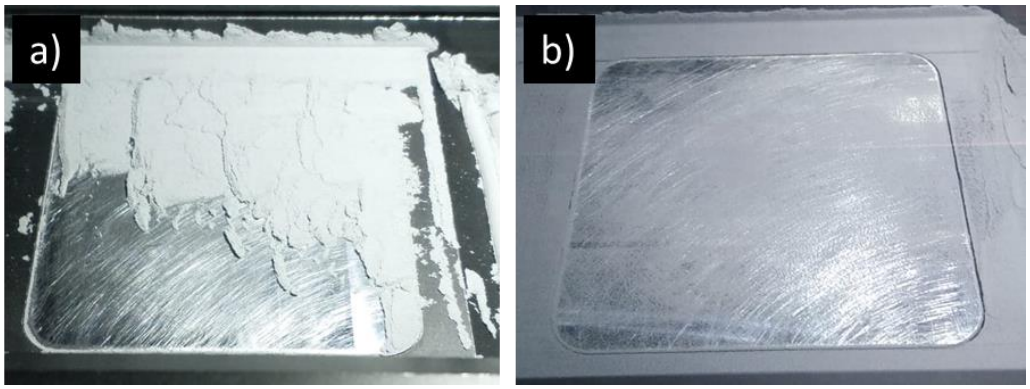

Figure 67: The aspect of the powder bed after the first layer deposition of Al3Er (a) and AlSr (b).

The spreading of the first layer with the Concept Laser Mlab Cusing R machine, is a manual operation. During this step of the process, the operator aligns the platform giving the 0 coordinate along the building direction. After this, the powder is spread on the building platform adjusting the height in order to create a thin layer of powder. This operation is very important to spread a good powder layer and assure the bonding of the samples to the platform. If the powder has a poor flowability, the deposition of thin layers is not possible. As consequence, the contact of the samples to the building platform could be difficult or insufficient.

The deposition of a thin layer of powder was not possible in the case of Al3Er (Figure 67-a), due to the poor flowability of the powders. This problem was overcame repeating several times the first layer deposition and taking special care of the building process, especially during the building of the first layers. Conversely, the deposition of AlSr (Figure 67-b) did not present any issues.

After mixing of both Al3Er+CL31 and AlSr+CL31, the powder was checked through SEM. Figure 68 shows the result of this analysis.

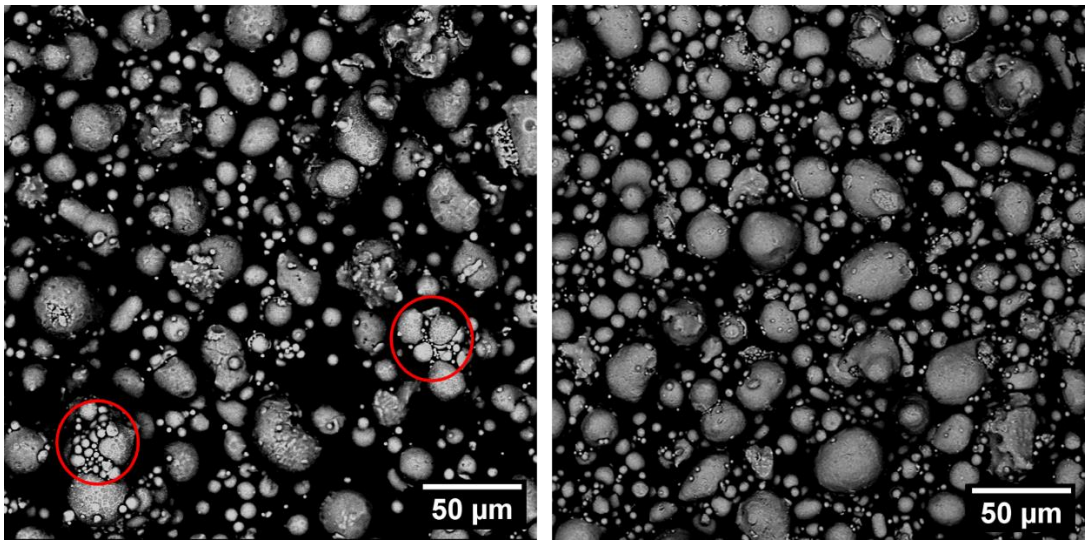

Figure 68: SEM images, with backscattered detector, of the two mixes Al3Er+CL31 (a) and AlSr+CL31 (b). In the Figure-a some agglomerates of finer particles, highlighted with a red circle, are present.

Concerning Al3Er+CL31 (Figure 68-a), it can be noticed that the mixing step promoted the deagglomeration of the finer particle, even if some cases of finer particles agglomerates are still present (red circles in Figure 68-a). It is clear that these agglomerates belong to the Al3Er from the color. The images are in fact obtained through backscattered detector, so brighter color of the agglomerates is due to heavier elements in their composition, in this case Er.

Concerning AlSr+CL31 (Figure 68-b) no big agglomerates of powder are present.

5.2 Er containing alloys

This paragraph describes the analyses conducted on the bulk samples produced with the powders containing Er in their composition. The Jobs performed were two: the first with the Al3Er powder and the second one with the mix Al3Er+CL31. The results and the consideration of these two jobs are treated separately.

5.2.1 Al3Er

The process parameters chosen for the Al3Er samples production are shown in **Table 16**.

Table 16: Process parameters used for Al3Er

Power [W]	Scan Speed [mm/s]	Hatching Distance [mm]	Layer Thickness [mm]	Strategy	VED [J/mm^3]

95	850	0.105	0.015	Island 90°	70.962
95	850	0.105	0.015	Stripes 67°	70.962
95	650	0.12	0.015	Island 90°	81.197
95	650	0.12	0.015	Stripes 67°	81.197
95	650	0.105	0.015	Island 90°	92.796
95	650	0.105	0.015	Stripes 67°	92.796
95	650	0.09	0.015	Island 90°	108.262
95	650	0.09	0.015	Stripes 67°	108.262
95	450	0.105	0.015	Island 90°	134.039
95	450	0.105	0.015	Stripes 67°	134.039

A Design of Experiment (DoE) involving an increasing VED value was adopted to optimize the process parameters. All the process parameter combinations were repeated for two scan strategies: Island (with a layer rotation of 90°) and Stripes (with a layer rotation of 67°).

The choice to perform a classic DOE approach rather than the SST method was because to correctly apply the SST technique, the single layer of powder should be spread on a substrate that presents the same chemical composition of the powder. The effect of the interaction between the powder and substrate on the stability of the laser track still needs to be clarified. Since there were no disks of the exact composition of the powders, in this case, the classical approach was preferred.

The densification of the samples was determined by image analysis. The results are represented in Figure 69.

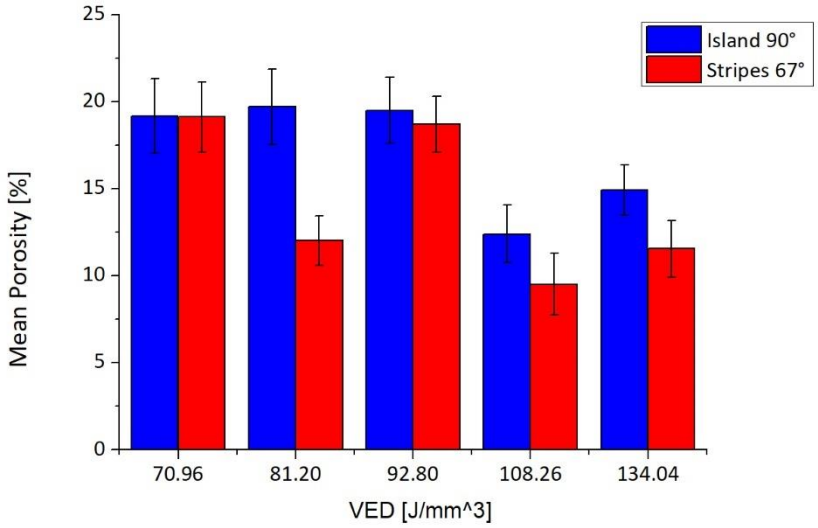

Figure 69: Mean porosity of Al3Er samples.

As can be noticed from the graph, the mean porosity of the samples was relatively high, regardless of the condition considered. The minimum value of porosity detected was around 10 %, which suggests that this alloy is not processable with the conditions chosen. However, the increase in VED decreased the mean porosity as expected, but the porosity was still too high. The effect of the different scan strategies was unclear since a trend in the results values was not evident.

It is probably impossible to obtain dense samples with this alloy using the Concept Laser MLab machine due to the limited power suppliable, which is not enough to overcome the high reflectivity of the aluminum powder. For this reason adding a high percentage of Silicon, like in CL31, helps to overcome this problem. In addition, an excessive increase in VED, obtainable with lower scan speed and layer thickness, could lead to further melting defects and a prolonged building process, which is unsuitable for practical application. Furthermore, the poor flowability of the powder could also contribute to the defect formation and the poor densification of the samples. In order to better understand the kind of defects of the bulk samples, further analysis on SEM were conducted (Figure 70).

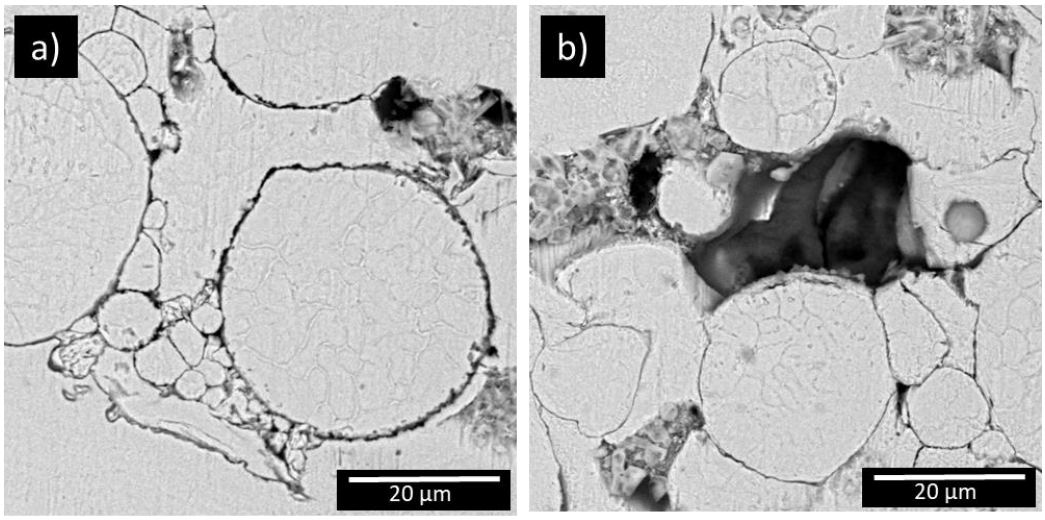

Figure 70: Micrographs of Al3Er with backscattered detector. On the samples were present several zones of unfused particles (a) and lack of fusions (b).

The samples presented different zones with unfused particles (Figure 70-a). This confirmed the previous assumption: the laser powder is not enough to perform a complete fusion of the particles, which are still present in the bulk samples. As a consequence, the incorrect melt led to the creation of large scales defects (with a dimension comparable to the powder granulometry), such as lack of fusions (Figure 70-b).

Due to the poor densification, this alloy was no longer took in consideration for further analyses.

5.2.2 Al3Er+CL31

After analyzing Al3Er samples, the next step was obtaining a mechanical mix with the AlSi10Mg (CL31) powder and the Al3Er, with a proportion 9:1. The AlSi10Mg alloy was chosen because it is a well-known system for LPBF technology and is widely used for different applications. The results in Chapter 4 already demonstrated the excellent processability of this alloy in the Concept machine, so the mechanical mix with Al3Er aims to improve the performances of CL31 in the as-built state.

The process parameters adopted to produce the samples with the mechanical mix are reported in **Table 17**.

Table 17: Process parameters used for Al3Er+CL31.

Sample code	Power [W]	Scan Speed [mm/s]	Hatching Distance [mm]	Layer Thickness [mm]	Strategy	VED [J/mm^3]
ST-NO-LOW	95	650	0.105	0.015	Stripes NO	92.8
IS-90°-LOW	95	650	0.105	0.015	Island 90°	92.8
ST-67°-LOW	95	650	0.105	0.015	Stripes 67°	92.8
ST-67°-HIGH	95	500	0.105	0.015	Stripes 67°	120.6

The samples were coded based on the scan strategy, the rotation between layers and the VED. For example, the first sample was coded as follows:

ST-NO-LOW

where ST indicates the scan strategy "stripes" (IS stands for "island"), NO indicates the rotation between layers (which in this case was not applied) and LOW indicates the VED which was set to the value of 92.796 J/mm^3(HIGH stands for 120.6 J/mm^3).

The next paragraphs will cover all the characterizations of the bulk samples obtained with the mechanical mix.

5.2.2.1 Porosity analysis

The densification of the samples was detected by image analysis. The results are shown in Figure 71.

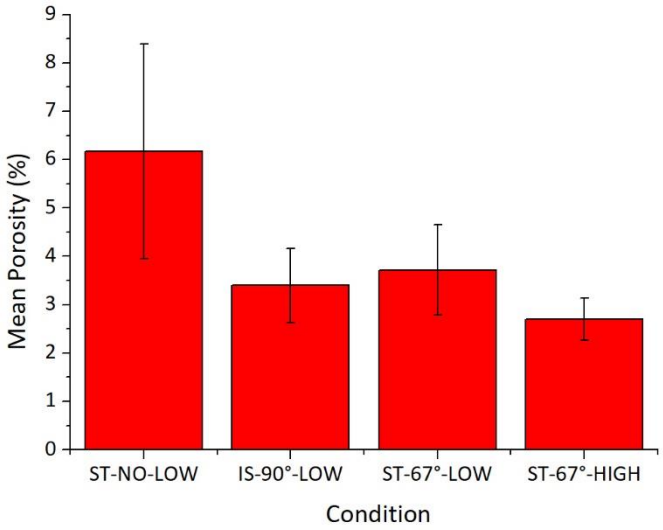

Figure 71: Mean porosity of Al3Er+CL31 samples.

As expected, the highest level of porosity was achieved with the sample ST-NO-LOW. In fact, the rotation of the scan strategy between layers promotes a better consolidation due to a more efficient overlapping of the laser tracks with the consequence of better densification. For this reason, most of the defects which contributed to decrease the mean relative density of the sample ST-NO-LOW are aligned along the building direction (Figure 72-a). On the other hand, the sample ST-67°-LOW, which implied the same process parameters as sample ST-NO-LOW but with a rotation between the layer of 67°, showed significantly better densification with the defects more distributed (Figure 72-b).

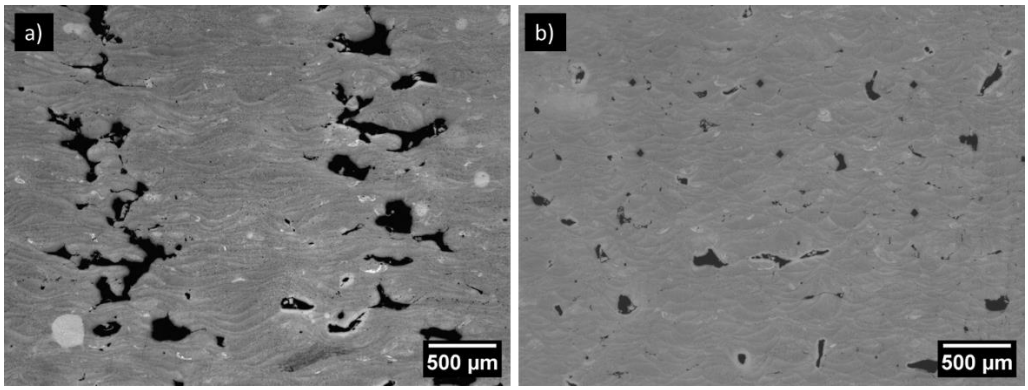

Figure 72: Optical micrographs of Al3Er+CL31 XZ section of ST-NO-LOW (a), with the defects aligned along the building direction and ST-67°-LOW (b), with the defects more distributed.

The difference between Island and Stripes scan strategies for the same process parameters (samples IS-90°-LOW and ST-67°-LOW) seemed negligible since the porosity value and the standard deviation is very similar. In addition, also an increase in VED (ST-67°-HIGH) did not significantly affect the densification.

In general, the porosity level achieved with the mechanical mix Al3Er+CL31, was higher than the one achieved with CL31 processed in the same conditions Figure 62. In fact, as described in Chapter 4, the highest porosity level achieved for AlSi10Mg was 1.12 % in the standard condition. Here, the IS-90°-LOW (with the same process parameters as CL31) is significantly higher, reaching a value of around 3.5 %. As expected, the poor processability of the Al3Er negatively affected the densification of the mechanical mix, even because it decreased the relative amount of silicon, worsening the fluidity of the alloy.

5.2.2.2 Microstructure

The microstructure of the samples was deeply investigated after metallographic preparation and chemical etching. In order to have different information, the samples were observed at different magnifications with different instruments. The investigation was carried out on a sample on ST-67°-LOW, representing the best sample in relative density.

Starting with the optical microscope analyses, the microstructure of the samples is represented in Figure 73.

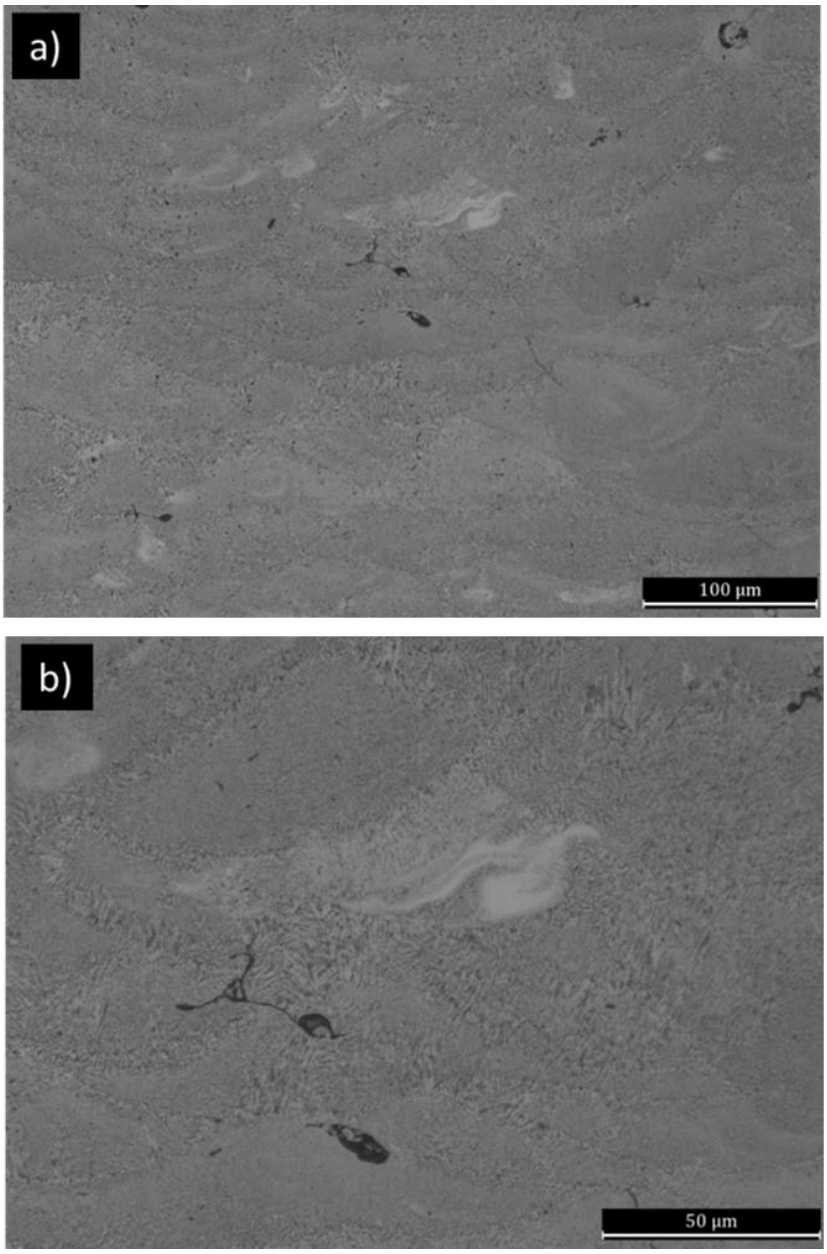

Figure 73: Optical micrographs of Al3Er+CL31 at 200 X (a) and 500 X (b) of.

As can be noticed, the etching corroded the alpha-Aluminum matrix revealing the silicon network and defining the borders of the melt pools. With this magnification, it is hard to determine the features of the silicon network. However, the first observation with LOM helped determine if the standard etching procedure of AlSi10Mg succeeded. In fact, since there are modifications in the composition of the base alloy, the etching conditions can be different. In addition, another detail was revealed: some brighter zones were present in the matrix where the chemical

composition is probably altered since the different behavior of the etching. Further analyses were necessary to determine the nature of these anomalies. The results are shown on the following pages.

Moving on to SEM analysis, the microstructure was deeply investigated. In order to have a complete overview of the microstructure the sample was observed before and after the chemical etching. The SEM micrograph before etching is represented in Figure 74.

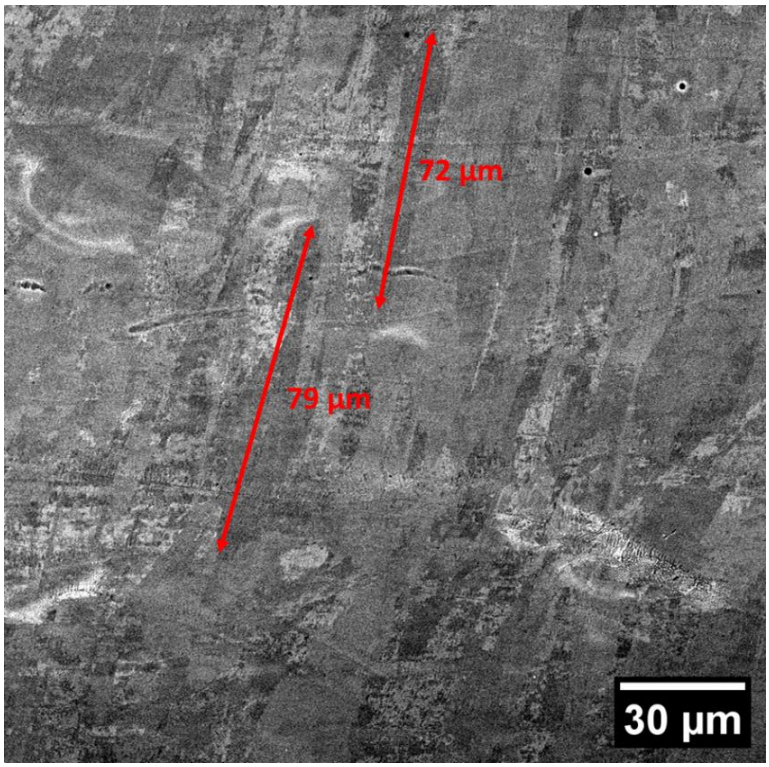

Figure 74: SEM micrograph of Al3Er+CL31 ST-67°-LOW without etching, where the columnar grains are visible.

For the first observation, the SEM was set at low magnification with a large spot size to observe a wide area. In this case, the no etching conditions, and the specific SEM setting allowed us to observe the grain texture. As can be noticed from Figure 74, the typical columnar grain texture derived from LPBF process was observed. The columnar grains derived from the directional thermal gradient which follows the building direction [119]. The dimensions of the grain can reach 70-80 µm, as highlighted in Figure 74, going through different melts pools and consolidated layers.

After etching the surface of the sample appeared different (Figure 75).

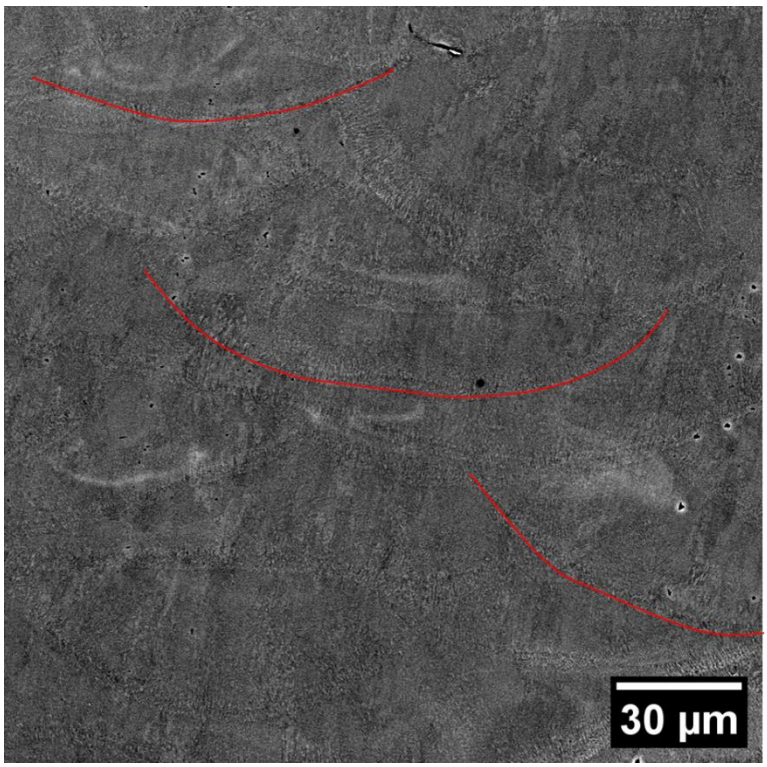

Figure 75: SEM micrograph of Al3Er+CL31 ST-67°-LOW sample etched, with some melt pools (red lines).

The grains were hard to see, while the melt pools more evident. In fact, since the etching corroded the alpha aluminum matrix and the silicon network was more visible, the border of the melt pools resulted more defined, due to the different morphology of the network in this zone. In this case, the SEM was set with the exact condition of Figure 74, so low magnification and large spot size, in order to have a complete overview of the sample, observing a wide area.

In both cases, the image acquisition was carried out through the electron backscattered detector in order to return information about the composition of the alloy. In fact, the brighter zones revealed by LOM observations (Figure 73) are also highlighted with the SEM backscattered detector, which suggests that the chemical composition of these anomalies is different to the matrix. The brighter features correspond to a higher atomic weight of the elements using the backscattered detector. Setting the SEM to the lowest magnification, it was possible to determine the distribution of these anomalies on the samples (Figure 76).

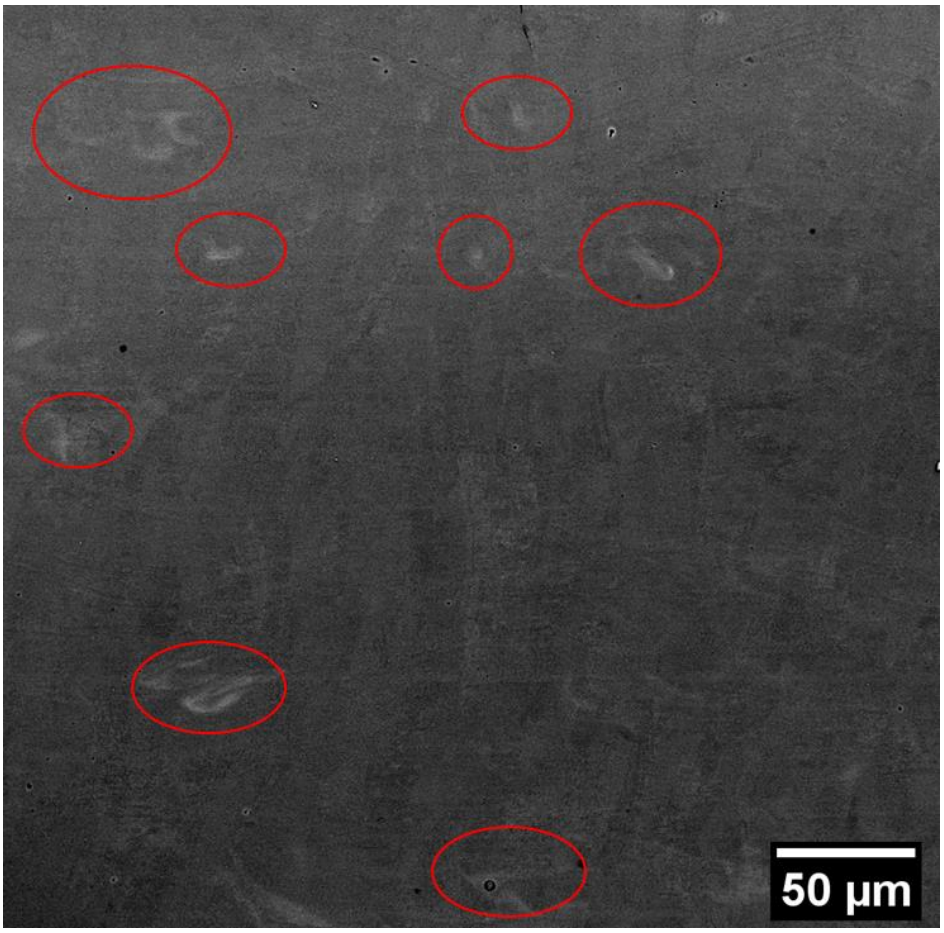

Figure 76: Low magnification SEM image ofAl3Er+CL31 ST-67°-LOW sample which revealed the distribution of the brighter zones.

Clearly, the Er distribution in the sample did not seem to be homogeneous, as suggested by the presence of the brighter zones of Figure 77. This information led to the conclusion that the sample presented local unbalances of chemical composition, which were not homogeneously distributed all over the matrix.

In order to confirm the hypothesis on the local unbalance of chemical composition, EDX analyses were performed (Figure **77**).

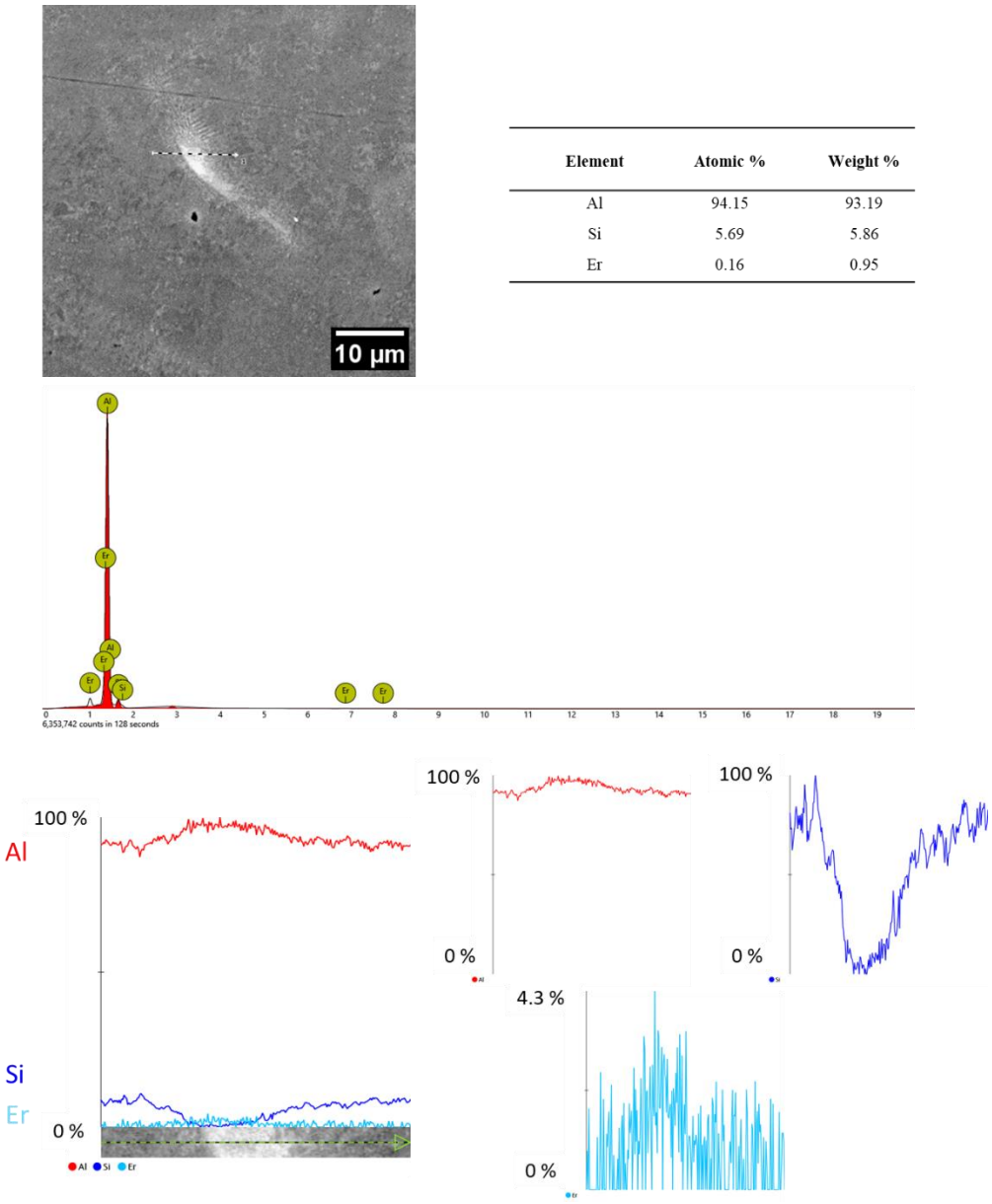

Figure 77: EDX line analysis ofAl3Er+CL31 ST-67°-LOW sample..

The line analysis of Zone 1 (Figure 77) revealed a mean weight concentration of Er three times higher than the base alloy composition (0.95 %wt. against 0.3 %wt.). In fact, the analysis revealed an increase in Er concentration and Al concentration with a significant decrease in Si in correspondence with the white zone.

A second analysis was carried out to confirm the previous result. The spot analysis on Zone 2 is reported in Figure 78.

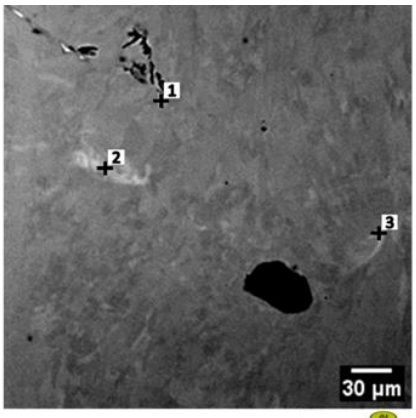

Spot 1

Element	Atomic %	Weight %
Al	92	91.70
Si	8.00	8.30
Er	0	0

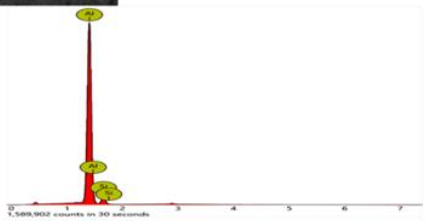

Spot 2

Element	Atomic %	Weight %
Al	99.69	98.14
Er	0.31	1.86
Si	0	0

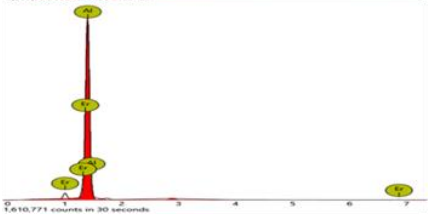

Spot 3

Element	Atomic %	Weight %
Al	99.67	97.98
Er	0.33	2.02
Si	0	0

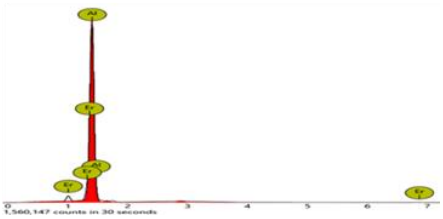

Figure 78: EDX spot analysis of Al3Er+CL31 ST-67°-LOW sample.

Spot 1 is referred to a random zone of the matrix to have a reference with respect to the zones chemically unbalanced. It can be noticed that here the amount of Si in weight is 8.3 %, which is slightly lower than the lower limit of the amount declared in the CL31 datasheet (9 %wt., see **Table 6)**. This can be caused by the addition to the CL31 of a powder which did not contain silicon that caused a dilution of Si in the whole sample. It is interesting to notice that the expected presence of Er in 0.3 % wt. was not detected in spot one, confirming the fact that the distribution of Er was not homogeneous. In fact, in spot 2 and 3, in correspondence with the brighter zones, the weight percentage of Er is respectively 1.86 and 2.02 %wt. Considering that the initial percentage of Er in the AlEr is 3 %, which is close to the values obtained, the diffusion of Er inside the matrix of AlSi10Mg was not successful,

resulting in Er rich zones where the powder of Al3Er was present in the powder bed before fusion.

After the EDX analyses, it can be asserted that the sample presented different zones where the Er did not mix thoroughly with the matrix (Er-rich zones). This phenomenon can be detrimental to the improvement of mechanical properties since the long-range diffusion of Er did not happen, confining the Er effects only in some specific zones.

In order to understand the variation of microstructure that Er could promote, higher magnification images were required. The magnification required to start to focus clearly the silicon network was 5 kX (Figure 79). Here it was possible to recognize the cells of the silicon network. Increasing the magnification and focusing on a Er-rich zone, it was possible to recognize a variation in the silicon network, which seemed to lose continuity in cell formation. However, with this magnification, it was impossible to understand the entity of this variation. Since this instrument magnification was the maximum possible, it was necessary to carry out the final analyses with a more powerful microscope.

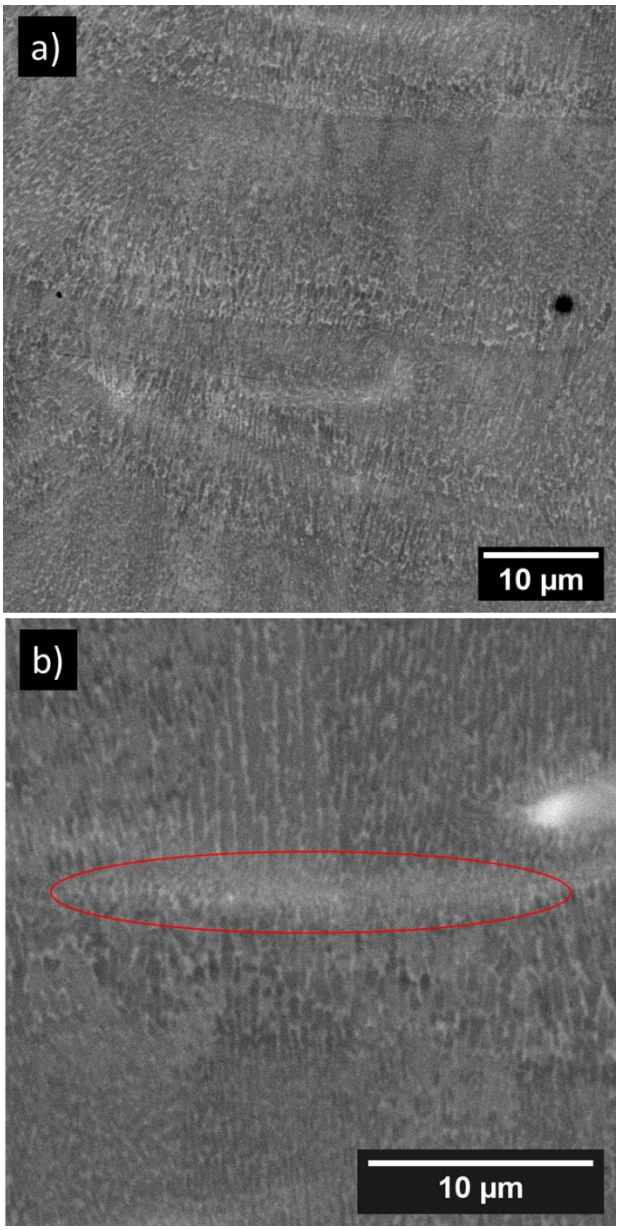

Figure 79: 5 kX (a) micrograph and 10 kX (b) micrographs ofAl3Er+CL31 ST-67°-LOW sample, with a Er-rich zone highlighted in red.

The last analysis was carried out with a FESEM to detect details of the silicon network and the eventual changes due to the presence of Er. An overview of the Si network structure is represented in Figure 80.

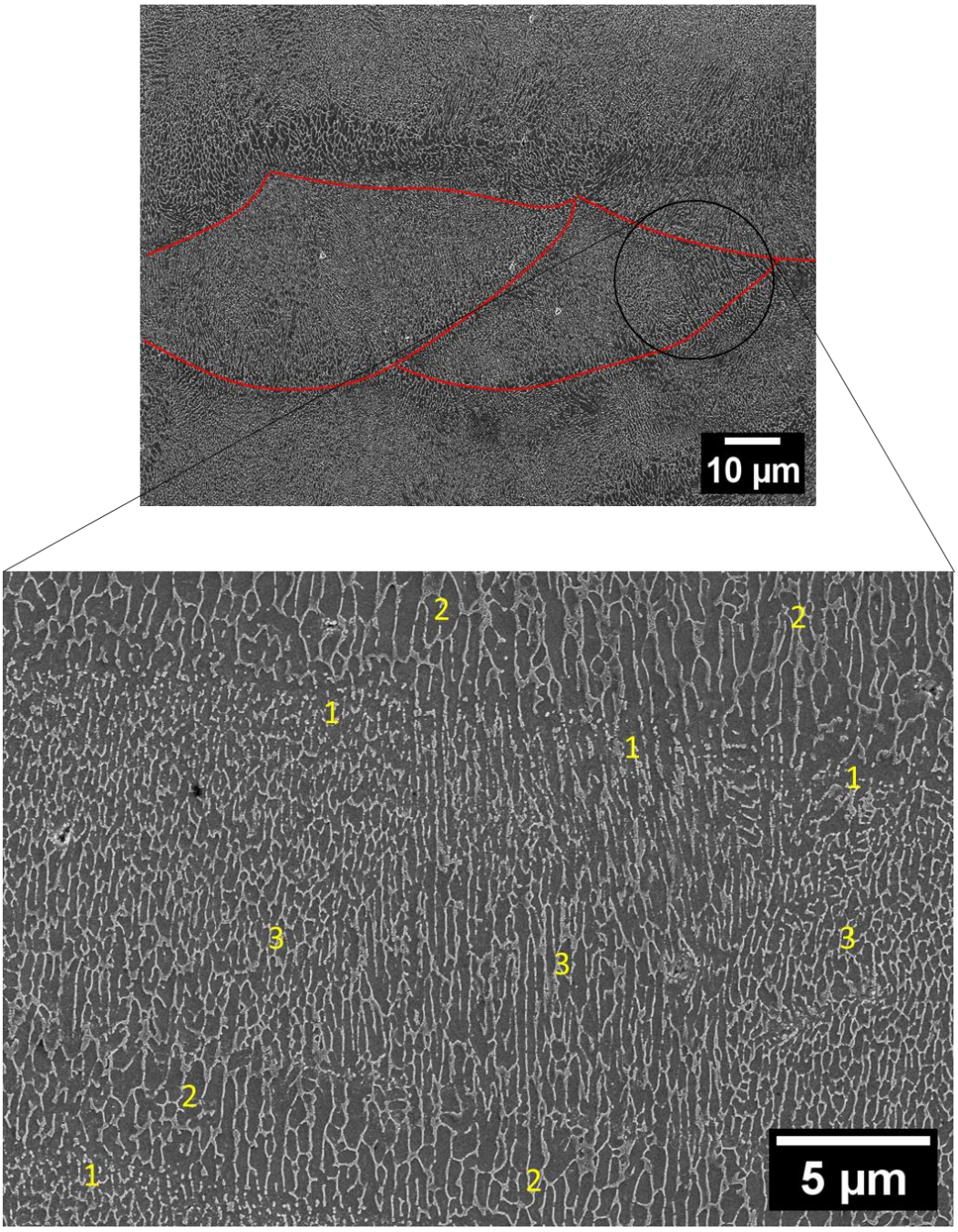

Figure 80: FESEM micrographs of Al3Er+CL31 ST-67°-LOW sample. The overview of the silicon network structure with the melt pools highlighted in red and a focus with higher magnification on the between two melt pools with the different zones of the network highlighted with yellow numbers.

As it can be noticed, the typical silicon network of AlSi10Mg is clearly visible. In particular the three different zone already described in 1.5 and in 4.4.1 were present:

- the HAZ (Figure 80, number 1) which consist in non-continuous silicon network at the border of the melt pools.
- The coarse dendritic structure (Figure 80, number 2) where the growth of the cells is favorable rather than the nucleation.
- The fine dendritic structure (Figure 80, number 3) where the cells are smaller and orientated along the building direction.

No long-range alterations of the network were detected, since the structure just described is the same of an AlSi10Mg produced via LPBF in as-built state.

As detected during the SEM analysis, in some zones (corresponding to the Er-rich zones) the silicon network was altered. Since the analysis on FESEM was carried out with an in-lens detector to have the maximum resolution possible of the silicon network, it was hard to recognize the Er-rich only by the difference in the grey shades of the images. For this reason, as happened for the SEM analysis, it was necessary to adopt dual images with an in-lens detector coupled with the backscattered detector Figure 81.

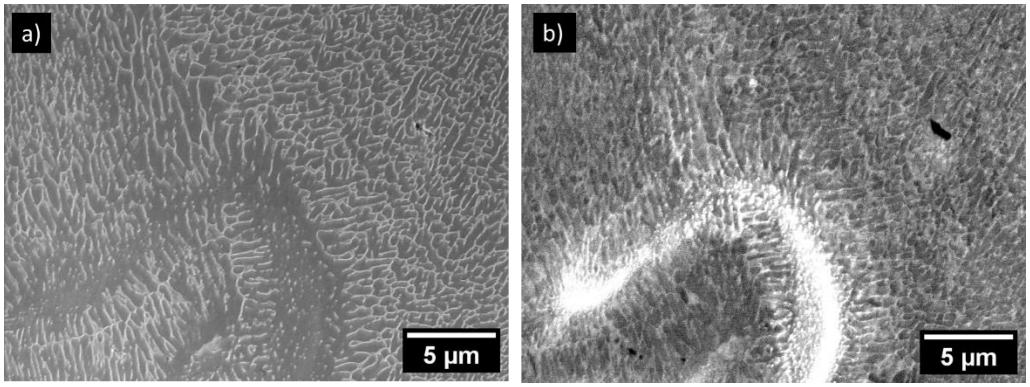

Figure 81: Dual image with in-lens detector (a) and backscattered detector (b) of an Er-rich zone.

It was noticed that in correspondence with the Er-rich zone which appears brighter using the backscattered detector (Figure 81-b), the silicon network was interrupted presenting isolated particles of silicon dispersed in the alpha aluminum matrix (Figure 81-a). In particular, the silicon network transferred into the typical fiber shape from globular shape, in line with the literature available for casting alloys [120].

In conclusion, the microstructure analyses, revealed the presence of Er-rich zones. In these zones the rupture of silicon network was promoted by the Er presence but

unfortunately this phenomenon did not happen in long range all over the matrix, but it was only confined in some zones randomly and not homogeneously distributed in the matrix.

5.2.2.3 Hardness tests

In order to understand the effect of Er on the mechanical properties of the samples, hardness tests were performed. The results are shown in Figure 82.

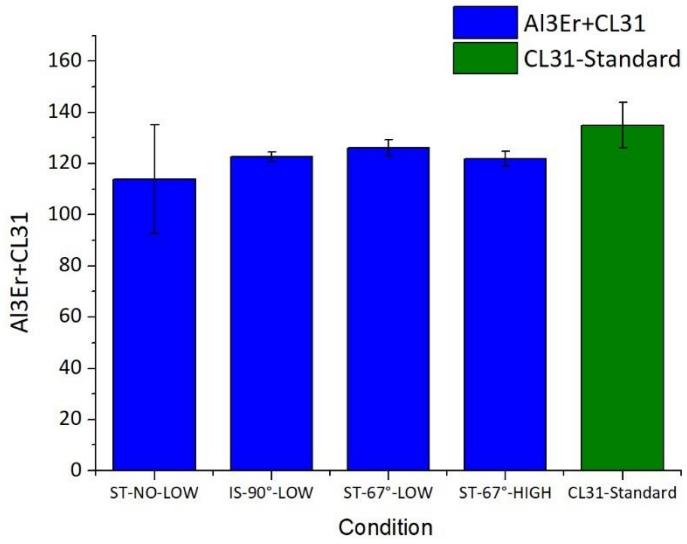

Figure 82: Hardness of Al3Er+CL31 samples in comparison with CL31.

The process parameters related to the conditions in the x-axis of the graph in Figure 82 are shown in **Table 17**.

The lowest hardness was reached with sample ST-NO-LOW, where the stripes scan strategy was applied without rotation of layers. This result is consistent with the porosity analysis since this sample presented the highest porosity level, which negatively affected the hardness. In addition, also the standard deviation between the hardness measurements of sample ST-NO-LOW was the highest due to the high porosity. This can affect the test since the probability of performing the measure on a defective area is higher. This means a significant decrease in the hardness in some zone rather than others and a high standard deviation. The other samples presented a similar hardness value of around 125 HV with a slight standard deviation. The sample IS-90°-LOW is related to the standard parameter of CL31 since the process parameters were the same. The IS-90°-LOW presented a hardness value slightly

lower than CL31. This result suggests that the rupture silicon network due to the presence of Er, slightly affected the hardness, regardless of the bad distribution of Er in the Aluminum matrix. According to literature, the same result (rupture of network and decrease in hardness) is achievable with a heat treatment under specific conditions. In addition, the decrease in hardness is associated with an increase in elongation of the samples, which means an increase in the ductility of the components [121].

5.2.2.4 XRD analysis

To identify the phases and to understand the forming of new phases due to the presence of Al3Er powders were formed, XRD analysis were performed. In Figure 83 is shown the spectrum of Al3Er+CL31.

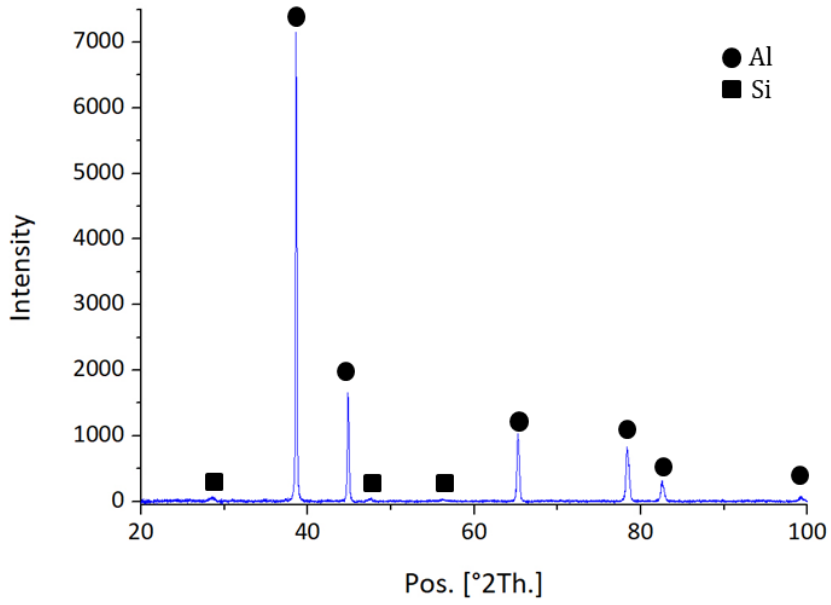

Figure 83: XRD pattern of Al3Er+CL31 ST-67°-LOW sample with the identification of the peaks.

The phases detected in the samples were mainly correspondent to α-Al and eutectic silicon. The intensity of the peaks of aluminum was higher than silicon peaks due to the low relative weight percentage of the silicon with respect to the aluminum. No other phases were detected, probably due to the limited amount of Er in the alloy or the too-small dimension of the precipitates. As explained in Chapter 1, the effect of erbium in aluminum alloys can be considered analogous to the one of the

scandium since the same tendency to form precipitates coherent with the matrix. Considering this, Spiering et al. demonstrated through transmission electron microscope (TEM) analysis that the precipitates of Al_3Sc are around 5-100 nm [101]. For this reason, the possible formation of these kind of precipitates due to the presence of Er could be no detectable with this kind of analysis.

5.2.2.4 DSC analysis

The method applied to understand the microstructural evolution was the DSC. The results of the analysis performed on Al3Er+CL31ST-67°-LOW sample are shown in Figure 84.

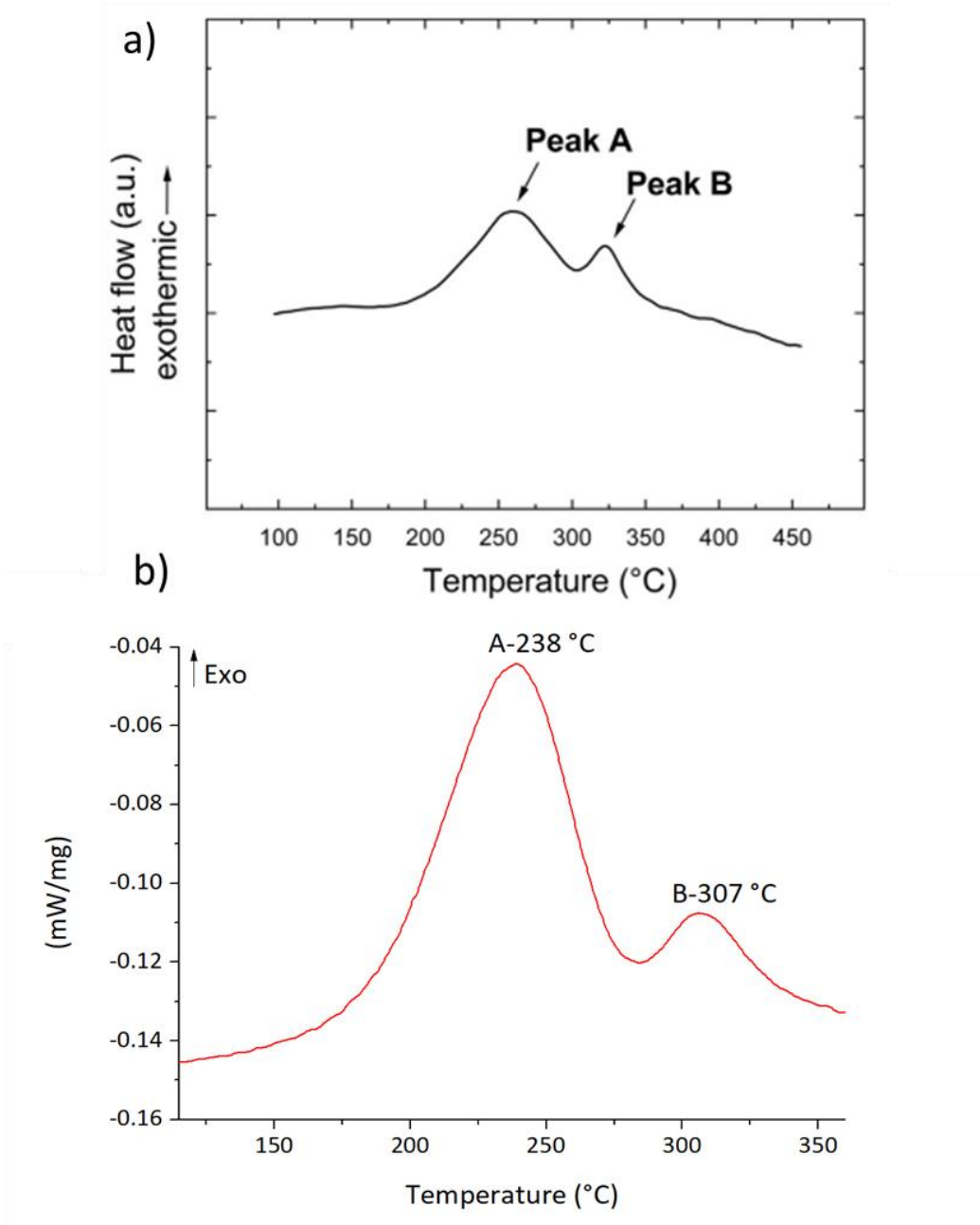

Figure 84: DSC graphs of AlSi10Mg not modified [122] (a) and Al3Er+CL31ST-67°-LOW sample . (b).

As represented in Figure 84-a, a typical DSC for AlSi10Mg produced via LPBF presents two main peaks [86], [122], [123]. The identification of these peaks is based on the interpretation of different authors. The peak A, according to Fiocchi et al., is attributed to the precipitation of Mg_2Si phase, while the peak B is mainly

due to the rupture and spheroidization of silicon phase [123]. On the other hand, Marola et al. attributed the peak A to the precipitation of silicon from the α-Al matrix and the peak B to the formation of precipitates Mg_2Si coupled with others containing Fe [86]. The max temperature of these peaks varies in the different works in a range between 230-260 °C for peak A and 300 and 320 °C for peak B, depending on the condition of the test.

The differences of the calorimetric results in terms of temperature of peak in the different works can be attributed to the inhomogeneity in the microstructure of as-built samples. In particular this effect is due to the fluctuations derived from different scanning modes and layer depositions. In addition, also different batches of powder can return different results in terms of calorimetry, since the different level of impurities of the powders [86].

In the present work, analyzing the Al3Er+CL31 samples (Figure 84-b), the characteristics of these two peaks of AlSi10Mg were present, with a max temperature of 238 °C for peak A and 307 °C for peak B. The results are consistent with the literature. No other peak associated with the presence of Er were detected. This result is analogous to the XRD analysis, suggesting that maybe the quantity of Er in the alloy was not enough to allow the formation of a new phase detectable with these techniques (XRD and DSC).

5.3 Sr containing alloys

This paragraph describes the analyses conducted on the bulk samples produced with the powders containing Sr in their composition. The Jobs performed were two: the first with the AlSr powder and the second one with the mix AlSr+CL31. The results and the consideration of these two jobs are treated separately.

All the analyses and procedures adopted in section 5.2 were repeated for this series of samples to directly compare the effect of the two kinds of strengthening elements on CL31.

5.3.1 AlSr

The process parameters adopted to produce the AlSr samples are the same used for Al3Er and are reported in **Table 16**. The results in terms of densification after image analysis are represented in Figure 85.

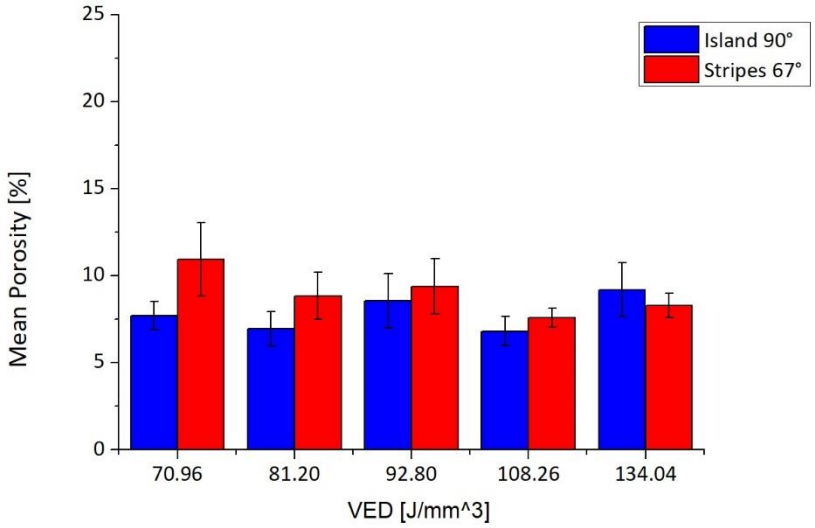

Figure 85: Mean porosity of AlSr samples.

From the porosity point of view, it appears clear that the scanning strategy did not significantly influence the densification. The same discussion can be extended to the VED since an increase in VED value did not affect the densification as expected. Since the best value in terms of porosity achieved was around 7 %, even in this case, it was possible to confirm that this alloy is not suitable to be processed in the Concept Laser MLab machine probably due to the insufficient power supplied.

It was interesting to compare the previous porosity results achieved for Al3Er with the one achieved for AlSr (Figure 86). It was possible to determine that the processability of AlSr is better than Al3Er since the porosity level was significantly lower in every condition studied. This result is probably due to the best spreadability of the powder which allowed the formation of more dense powder bed with a significant improvement in the final densification of the samples.

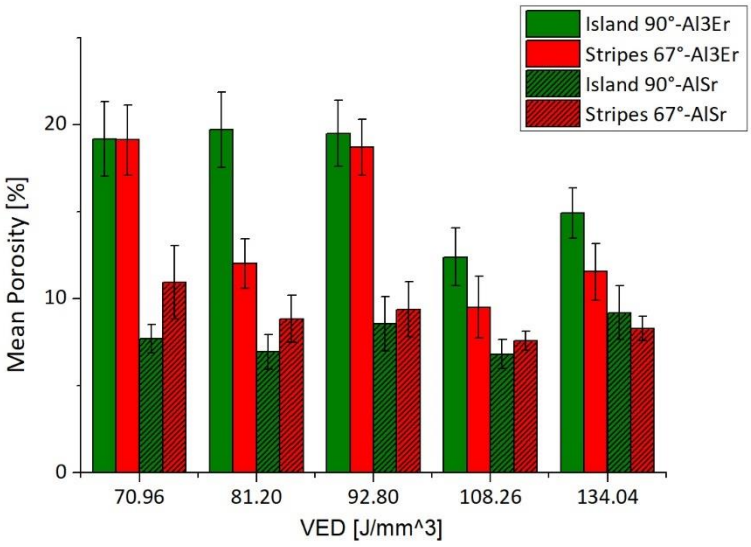

Figure 86: Mean porosity comparison between Al3Er samples and AlSr.

Even in this case, no further analyses were performed since the mean porosity was relatively high.

5.3.2 AlSr+CL31

As happened for Al3Er+CL31 the next step was to study the properties of the samples produced with the mechanical mix AlSr+CL31.

The process parameters adopted to produce this series of samples are equal to the ones used to produce Al3Er+CL31 samples and are reported in **Table 17**.

It follows all the description of the characterizations performed to determine the properties of these samples.

5.3.2.1 Porosity analysis

The porosity analysis results, measured through image analysis are reported in Figure 87.

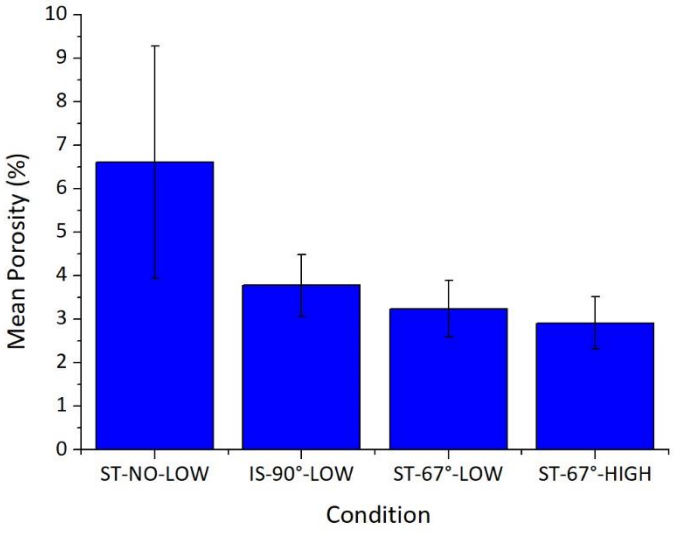

Figure 87: Mean porosity of AlSr+CL31 samples.

Even in this case, as expected, the sample SR-NO-LOW presented the highest level of porosity, for the same reasons already discussed in section 5.2.2.1. The samples IS-90°-LOW and ST-67°-LOW did not present significant differences in terms of mean porosity and standard deviation, suggesting that changing the scanning strategy did not affect the densification. Finally, the sample ST-67°-HIGH presented the lowest level of mean porosity but considering the standard deviation the result is statistically comparable with IS-90°-LOW and ST-67°-LOW conditions. This confirms that neither an increase of VED value influenced positively the densification.

Comparing the results of porosity between the two mechanical mix (Figure 88), is clear that the porosity levels of Al3Er+CL31 and AlSr+CL31 are comparable in all the conditions studied. In general, extending the consideration already done for Al3Er+CL31, the lower processability of the powder containing the strengthening element affected the processability of CL31 in both cases.

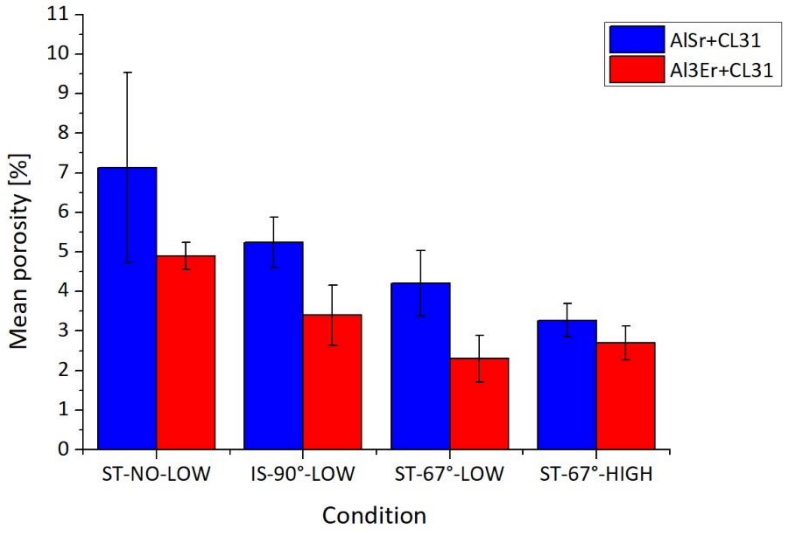

Figure 88: Comparison of mean porosities value between AlSr+CL31 and Al3Er+CL31.

5.3.2.1 Microstructure

The same microstructural analysis procedure of Al3Er+CL31 was applied to the present samples, focusing on the main results already discussed: presence of Sr-rich zones and details at high magnification of microstructure.

In contrast with the LOM observation of Al3Er+CL31, no evident compositional anomalies in the microstructure were detected (Figure 89). This suggests that the distribution of the Sr in CL31 matrix was better than the one achieved with Er in the same conditions.

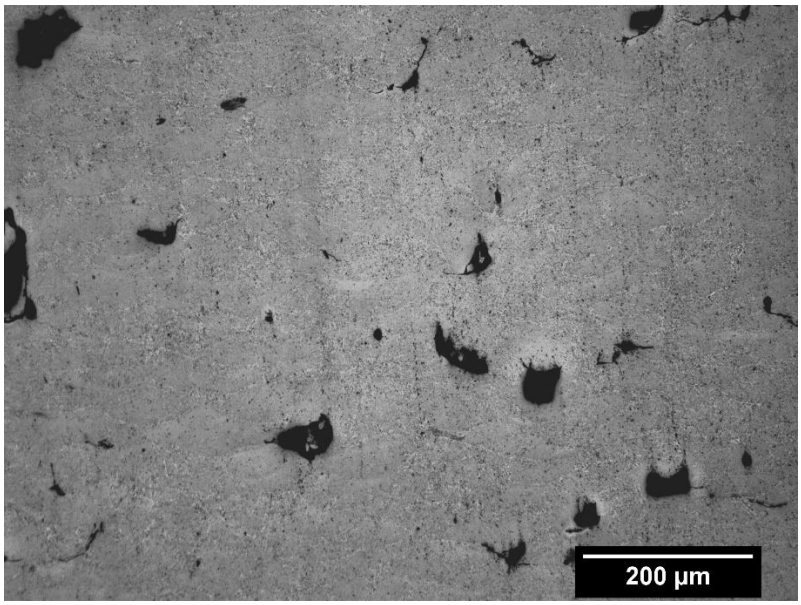

Figure 89: LOM image of AlSr+CL31 ST-67°-LOW sample after etching.

To confirm this result, the observation of AlSr+CL31 was carried out through SEM with the backscattered detector. As it can be noticed from Figure 90, the presence of brighter zones, corresponding to a chemical unbalance and higher heavy elements concentration, is significantly limited with respect to Al3Er+CL31 samples. This result confirms the hypothesis of a better distribution of the Sr in the CL31, rather than Er.

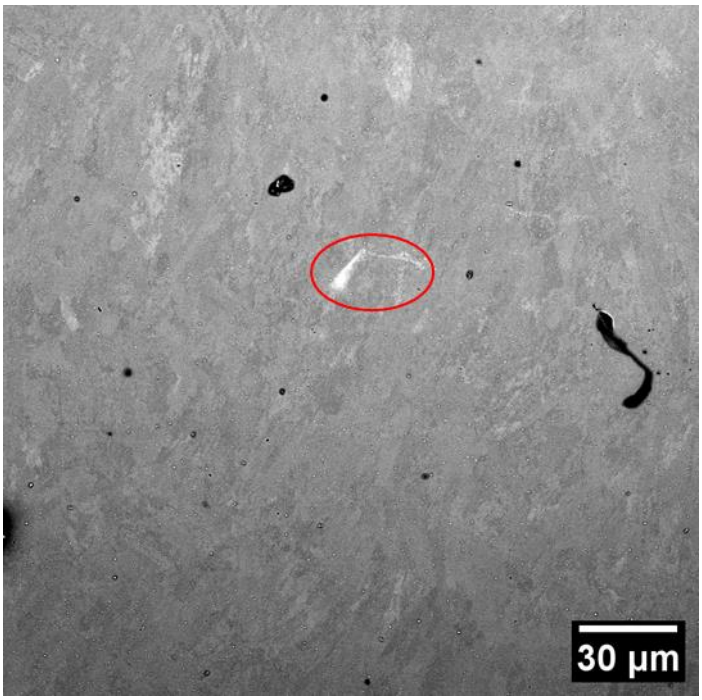

Figure 90: SEM image of with backscattered detector of AlSr+CL31 ST-67°-LOW sample.

However, the limited amount of brighter zones were analyzed to find out their chemical composition. The EDX analysis in Figure 91 shows a spot analysis on a brighter zone of AlSr+CL31. As reported, the chemical composition detected in this zone presented a decrease in the amount of silicon with respect to the CL31 value and a high amount of Sr. Probably in these zones, there was the powder which presented melting defects which did not allow complete mixing of the compositions. However, as already reported, these zones were rarely present in the CL31 matrix, suggesting that the nature of these anomalies was a local melting defect.

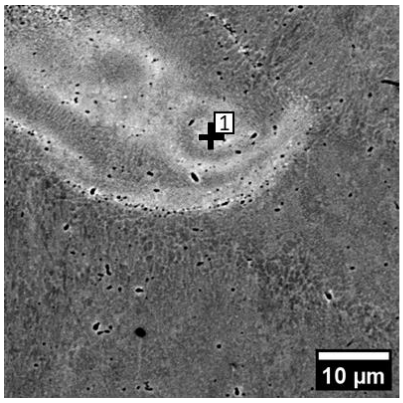

Spot 1

Element	Atomic %	Weight %
Al	94.15	93.19
Si	5.69	5.86
Sr	0.16	0.95

Figure 91: Spot EDX analysis on a Sr-rich zone of AlSr+CL31 ST-67°-LOW sample.

The last step in microstructure analysis was the FESEM imaging, as performed for Al3Er+CL31. Figure 92, where the zones of the melt pool are highlighted as in Figure 22, reveals the silicon network structure, and a difference can be noticed with respect to a conventional AlSi10Mg silicon network. The dendritic structure at the center of the melt pool appeared fragmented and discontinuous. Considering the cells of the network, some presented finer branches, with some isolated silicon precipitates at the center of the cell. This result is consistent with the literature about the cast production. In fact, it was demonstrated that the presence of Sr in cast AlSi10Mg, contributes to refine the silicon network producing a thinner fibrous eutectic silicon phase [124].

However, in opposition with the microstructure related to Al3Er+CL31, the modification of the network was not completely clear and a comparison with CL31 was necessary.

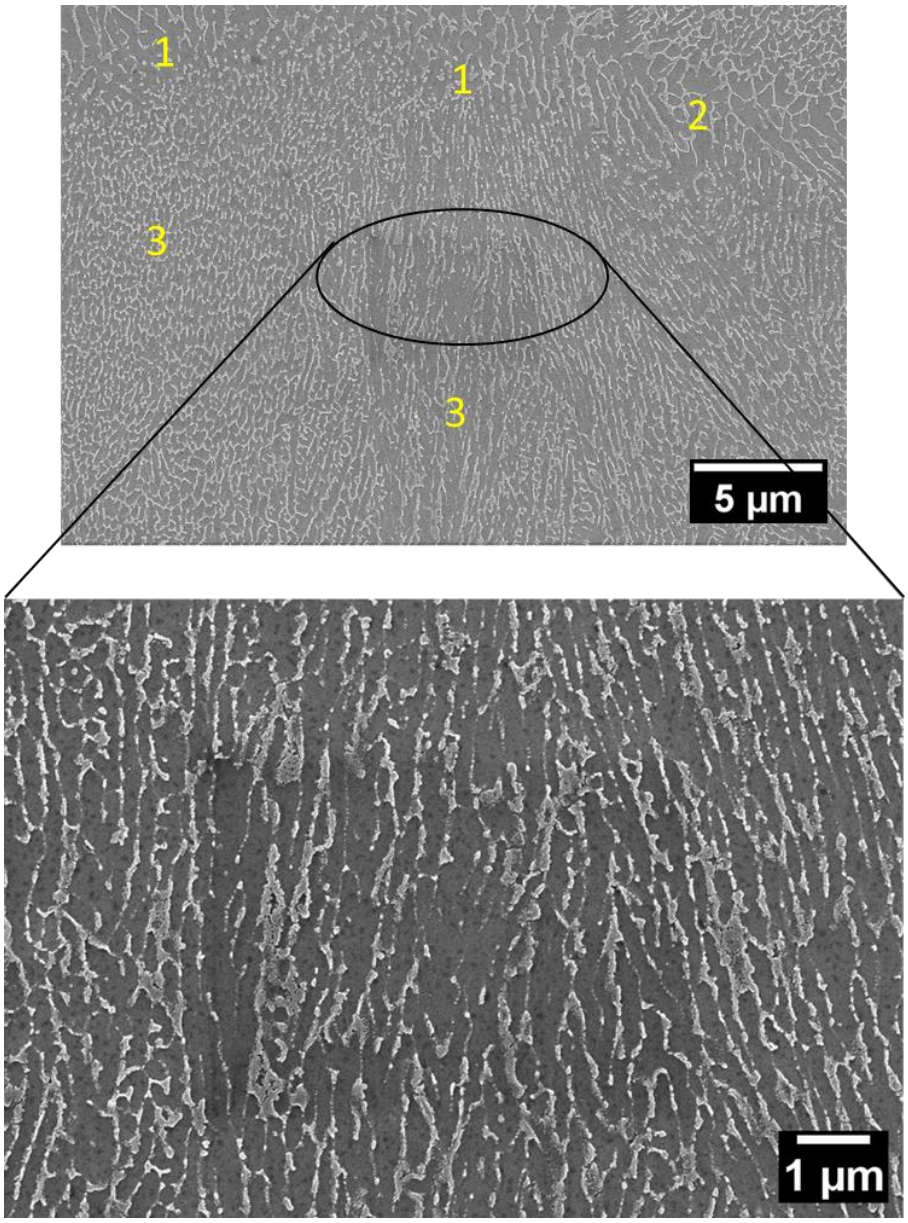

Figure 92: Overview of the silicon network at the center of the melt pool, with a detail at high magnification AlSr+CL31 ST-67°-LOW sample. The numbers are referred to the zone classification adopted in Figure 80.

Figure 93 shows a comparison between the silicon network of a conventional CL31 sample and the AlSr+CL31 one, produced with the same process parameters combination. The images were acquired in both cases at the center of the melt pool (1-FD zone). It is clear that, in opposition with the Al3Er+CL31 microstructure, in this case was harder to recognize the effect of Sr on the morphology of the Si

network. The main difference between the microstructure was the presence of finer silicon cells borders, highlighted in Figure 93-b with red arrows.

In fact, since the distribution of Sr in the aluminum matrix seemed to be effective there were no evident zone Sr-rich where is easy to define the effect of Sr on the silicon-network.

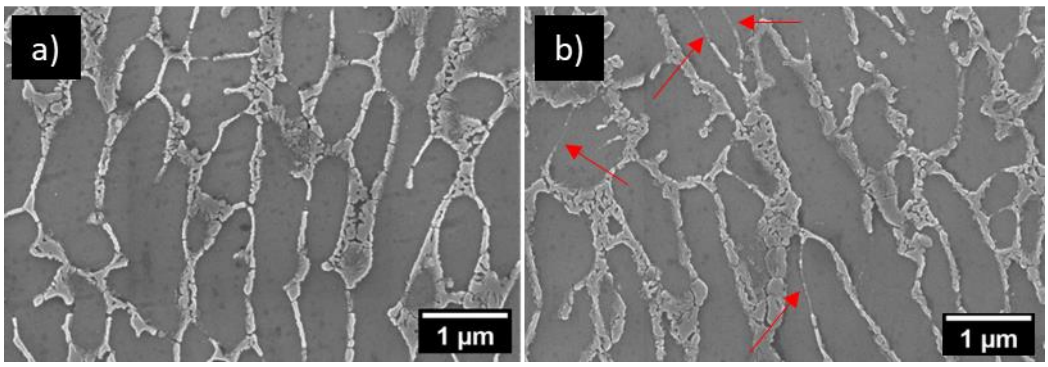

Figure 93: Comparison between CL31 (a) silicon network and AlSr+CL31 silicon network (b). The red arrows highlight the finer silicon phase.

5.3.2.3 Hardness tests

To determine the variation in terms of mechanical properties that the modification of the silicon network caused, hardness tests were performed. The results are represented in Figure 94.

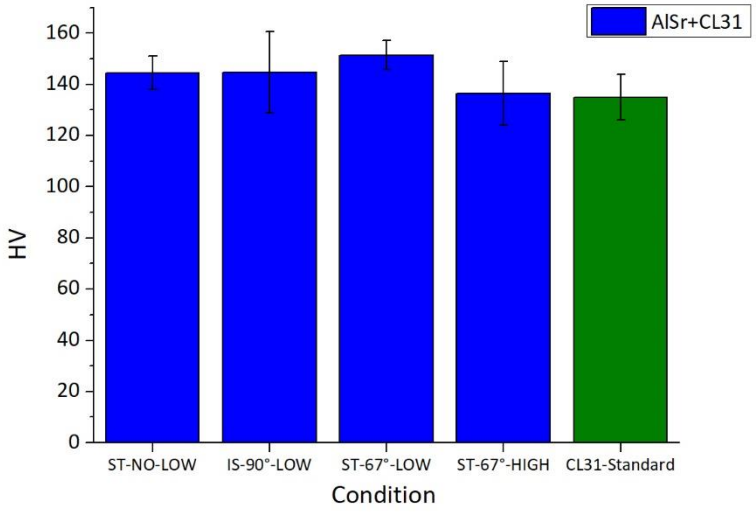

Figure 94: Hardness value of AlSr+CL31 in comparison with CL31.

The hardness in all condition of AlSr+CL31 seemed to be not affected by the porosity difference of the samples. In all conditions the value of hardness of AlSr+CL31 was similar to CL31 one. In this case, probably the slight modification of the silicon network, due to the presence of Sr in the alloy, was not enough to affect the hardness of CL31.

For comparison in Figure 95 are reported the value of hardness of AlSr+CL31 and Al3Er+CL31.

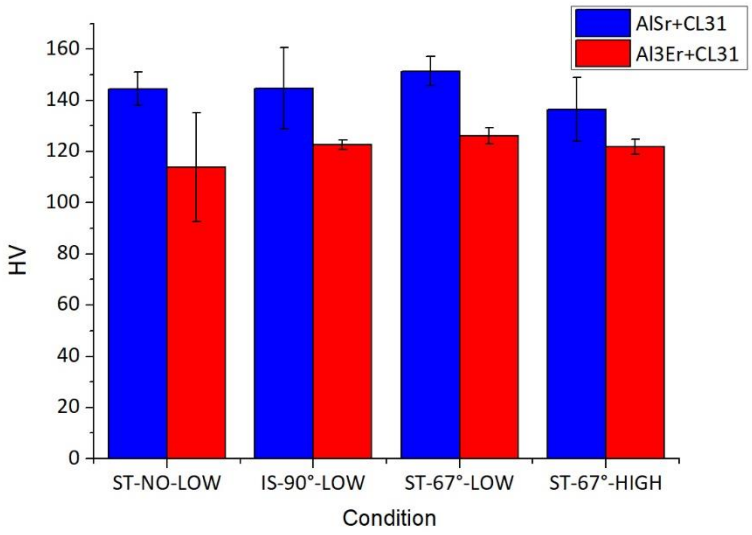

Figure 95: Hardness comparison between samples of AlSr+CL31 and Al3Er+CL31.

It is clear that the hardness of Al3Er+CL31 samples is lower than the AlSr+CL31 one, which it was demonstrated to be very similar to CL31.

Regardless of the poor distribution in the aluminum matrix, the erbium seemed to be the best choice in terms of properties modifier since the effect on the final hardness of CL31 was more evident with respect of Sr.

5.3.2.4 XRD analysis

For the phases identification XRD analyses were performed. The XRD pattern of AlSr+CL31 is reported in Figure 96.

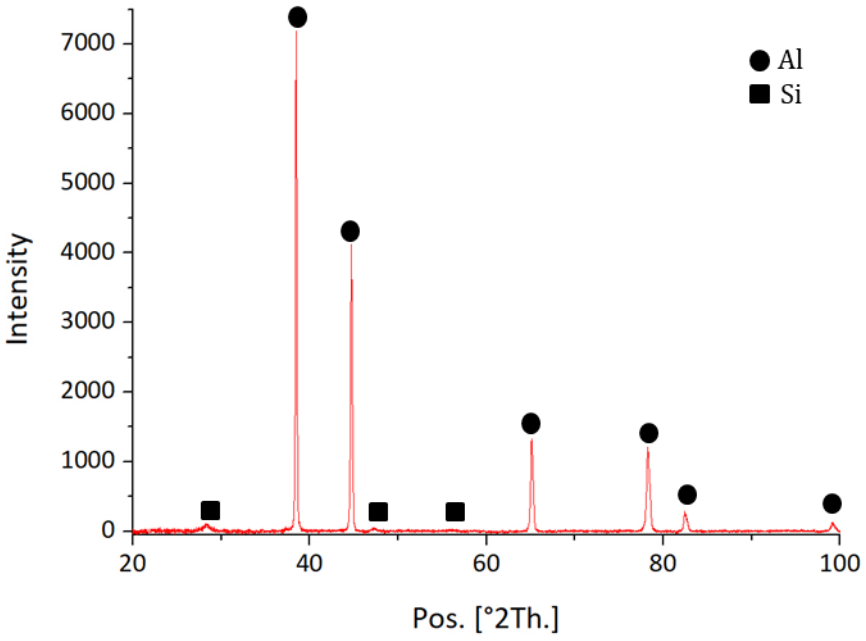

Figure 96: XRD pattern of AlSr+CL31 ST-67°-LOW sample with the identification of the peaks.

Even in this case, the peaks identified are related to α-Al phase and eutectic silicon phase. No peaks related to the presence of Sr were detected. probably due to the same reason already explained in section 5.2.2.3. In fact, the XRD pattern in Figure 96 is equal to one Figure 83, related to Al3Er+CL31. For this reason, al the considerations made for Al3Er+CL31 are valid also for AlSr+CL31.

5.3.2.5 DSC analysis

The results of DSC analysis are shown in Figure 97.

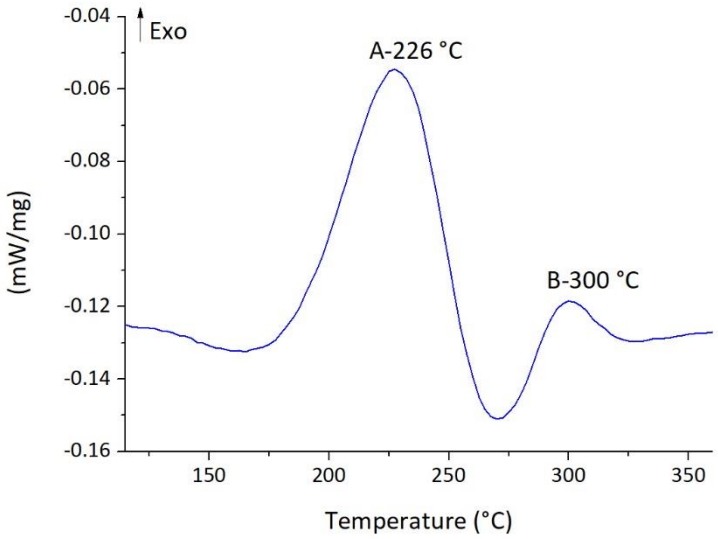

Figure 97: DSC graph of AlSr+CL31.

The graph in Figure 97 is analogous to the one present in Figure 84-b. Two main peak were present with the peak temperature of peak A at 226 °C and the peak temperature of peak B at 300 °C. No further peaks associable with the presence of Sr in the alloy were detected. The same conclusion, already described for Al3Er+CL31, can be drawn, i.e., the presence of the strontium is not enough to promote the formation of a new phase detectable with DSC analysis.

Comparing the curves of Al3Er+CL31 and AlSr+CL31 (Figure 98), it is clear that the curve related to AlSr+CL31 is shifted to lower temperature with the respect to Al3Er+CL31. A possible explanation can be the slight difference in the silicon network. In fact, in the case of AlSr+CL31, the silicon network appeared finer in long-range. For this reason, probably part of the silicon is already in solid solution with the matrix of aluminum and the further fragmentation of the silicon network (peak A) and the precipitation of Mg_2Si (peak B), happened at lower temperatures. However, the observation of the Silicon network was only a qualitative analysis, and no confirmations of this theory can be drawn.

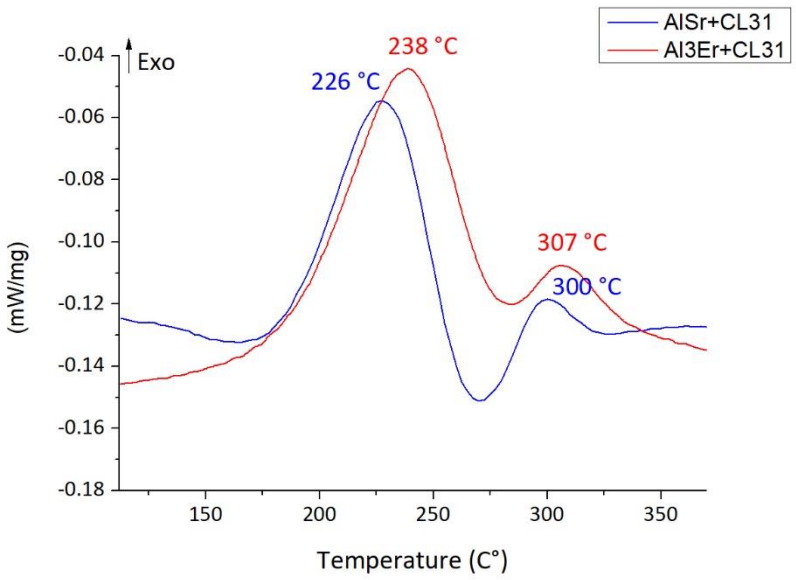

Figure 98: Comparison of DSC curves of AlSr+CL31 and Al3Er+CL31.

Chapter 6

Conclusions

This work aimed to cover the entire process of sample production via AM technology, starting from powder production via gas atomization reaching the production of bulk samples with LPBF technique.

At first, an AlSi10Mg powder was produced with a laboratory-scale gas atomizer. After that, the powder was characterized and compared with a commercial-grade counterpart, in order to determine the differences in terms of properties between a laboratory-scale gas atomized powder and an industrial-scale one. Afterwards, a step of LPBF process parameters optimization was carried out using the SST method , trying to overcome the main criticism of this technique and updating the analysis with an automatic version. After the confirmation of the best process parameters combination, bulk samples were produced with both powders in order to determine densification microstructure and mechanical properties. The last step of the work concerned the improvement of AlSi10Mg in as-built state through modifications of its composition. In this step, the influence of modifying elements such as Er and Sr on the final properties of AlSi10Mg was investigated.

Considering each step of the process described above, the main conclusions can be drawn, divided by main topics. As far as the gas atomization parameters optimization is concerned:

- The process parameters suggested by the gas atomizer manufacturer (PSI) to produce AlSi10Mg powders were correct to guarantee the higher yield in 20-50 μm fraction.
- An increase in atomization pressure from 40 bar to 50 bar did not influence the total amount of 20-50 μm particles.
- The different material of the crucible did not influence the powder characteristics.
- Neither the load influenced the powders characteristics.

According to the powder comparison between CL31 and HM, it can be asserted:

- The main difference between the two powders was in the finer particles amount detected by number PSD. The amount of finer particles of HM was significantly lower than CL31.
- The oxidation level of HM was lower than CL31.
- Due to the lower number of finer particles and the lower oxidation level, HM powders presented a better powder packing than CL31 (lower Hausner ratio).
- In general, the laboratory-scale atomization process allowed to produce a powder perfectly suitable for LPBF and slightly better than CL31.

Considering the optimization of process parameters through the method of SST, the following conclusions can be drawn:

- The SST method is a rapid and material-saving analysis which present some critical points.
- The application of an automatic method (Index Method) applied to the on-top analysis allowed to overcome the main problem of SST due to the operator error.
- The Index Method was validated with a Al4Cu alloy and then applied to CL31, confirming the best combination of laser powder and scan speed suggested by Concept Laser (standard parameters).
- The optimal hatching distance detected the by Index Method revealed that the hatching value of the standard parameter suggested by Concept Laser must be adjusted in order to obtain the best densification of the samples.

Moving on the comparison between the bulk samples of CL31 and HM it has been demonstrated that:

- The density of the HM samples was slightly higher than CL31 ones, probably due to the better packing density.
- No differences between HM and CL31 microstructures were detected.
- The mechanical properties of HM and CL31 samples were strongly comparable. Only the YS of HM was slightly higher than CL31, probably due to the better densification.

Finally, considering the CL31 new compositions with the modifying elements, the following conclusions can be drawn:

- The mechanical mix of CL31 with the modifying elements powders affected the densification in both cases.
- Er was poorly distributed in the aluminum matrix, while the Sr presented a better distribution.
- New phases were not detectable with XRD and DSC analysis probably due to their low content.

This preliminary study on the composition modification did not reveal an evident change in the mechanical properties of AlSi10Mg. The slight changes in hardness with adding Er to the composition suggest a slight change in the mechanical properties, but successive mechanical tests must confirm this. However, the poor distribution of the Er in the AlSi10Mg matrix can be detrimental to the final properties of the components. A better way to improve the distribution is necessary.

References

[1] D. R. Eyers and A. T. Potter, “Computers in Industry Industrial Additive Manufacturing : A manufacturing systems perspective,” vol. 93, pp. 208–218, 2017, doi: 10.1016/j.compind.2017.08.002.

[2] A. Kirchheim, H.-J. Dennig, and L. Zumofen, “Why Education and Training in the Field of Additive Manufacturing is a Necessity,” in *Industrializing Additive Manufacturing - Proceedings of Additive Manufacturing in Products and Applications - AMPA2017*, Springer International Publishing, 2018, pp. 329–336. doi: 10.1007/978-3-319-66866-6_31.

[3] W. E. Frazier, “Metal Additive Manufacturing: A Review”, doi: 10.1007/s11665-014-0958-z.

[4] “Wohlers Report 2019 – Dansk AM Hub.” https://am-hub.dk/wohlers-report-2019/ (accessed Apr. 28, 2022).

[5] I. Gibson, D. Rosen, B. Stucker, and M. Khorasani, “Additive Manufacturing Technologies,” *Additive Manufacturing Technologies*, 2021, doi: 10.1007/978-3-030-56127-7.

[6] “Standard Terminology for Additive Manufacturing Technologies, (Withdrawn 2015).” https://www.astm.org/f2792-12a.html (accessed Apr. 30, 2022).

[7] P. Charalampous, I. Kostavelis, and D. Tzovaras, “Non-destructive quality control methods in additive manufacturing: a survey,” *Rapid Prototyp J*, vol. 26, no. 4, pp. 777–790, May 2020, doi: 10.1108/RPJ-08-2019-0224.

[8] N. Kladovasilakis, P. Charalampous, I. Kostavelis, D. Tzetzis, and · Dimitrios Tzovaras, “Impact of metal additive manufacturing parameters on the powder bed fusion and direct energy deposition processes: a comprehensive review,” vol. 6, pp. 349–365, 2021, doi: 10.1007/s40964-021-00180-8.

[9] A. T. Sutton, C. S. Kriewall, M. C. Leu, and J. W. Newkirk, "Powder characterisation techniques and effects of powder characteristics on part properties in powder-bed fusion processes," *http://dx.doi.org/10.1080/17452759.2016.1250605*, vol. 12, no. 1, pp. 3–29, Jan. 2016, doi: 10.1080/17452759.2016.1250605.

[10] M. Qian, "Metal Powder for Additive Manufacturing," *JOM*, vol. 67, no. 3, 2015, doi: 10.1007/s11837-015-1321-z.

[11] A. Popovich and V. Sufiiarov, "Metal Powder Additive Manufacturing," *New Trends in 3D Printing*, Jul. 2016, doi: 10.5772/63337.

[12] J. Wang, M. Xia, J. Wu, and C. Ge, "Ladle Nozzle Clogging in Vacuum Induction Melting Gas Atomization: Influence of the Melt Viscosity," *Metallurgical and Materials Transactions B: Process Metallurgy and Materials Processing Science*, vol. 53, no. 4, pp. 2386–2397, Aug. 2022, doi: 10.1007/S11663-022-02537-Y/FIGURES/16.

[13] M. A. Smirnov, M. A. Kaplan, and M. A. Sevostyanov, "Receiving finely divided metal powder by inert gas atomization," in *IOP Conference Series: Materials Science and Engineering*, Apr. 2018, vol. 347, no. 1. doi: 10.1088/1757-899X/347/1/012033.

[14] A. Martín, C. M. Cepeda-Jiménez, and M. T. Pérez-Prado, "Gas atomization of γ-TiAl Alloy Powder for Additive Manufacturing," *Adv Eng Mater*, vol. 22, no. 1, Jan. 2020, doi: 10.1002/adem.201900594.

[15] M. J. Tobar, J. M. Amado, J. Montero, and A. Yáñez, "A study on the effects of the use of gas or water atomized AISI 316L steel powder on the corrosion resistance of laser deposited material," in *Physics Procedia*, 2016, vol. 83, pp. 606–612. doi: 10.1016/j.phpro.2016.08.063.

[16] U. Fritsching and V. Uhlenwinkel, "5 Hybrid Gas Atomization for Powder Production." [Online]. Available: www.intechopen.com

[17] R. Tamura *et al.*, "Machine learning-driven optimization in powder manufacturing of Ni-Co based superalloy," *Mater Des*, vol. 198, p. 109290, Jan. 2021, doi: 10.1016/J.MATDES.2020.109290.

[18] E. Urionabarrenetxea, A. Avello, A. Rivas, and J. M. Martín, "Experimental study of the influence of operational and geometric variables on the powders

produced by close-coupled gas atomisation," *Mater Des*, vol. 199, Feb. 2021, doi: 10.1016/j.matdes.2020.109441.

[19] D. Singh and S. Dangwal, "Effects of process parameters on surface morphology of metal powders produced by free fall gas atomization," *J Mater Sci*, vol. 41, no. 12, pp. 3853–3860, Jun. 2006, doi: 10.1007/s10853-006-6652-2.

[20] A. Ünal, "Effect of processing variables on particle size in gas atomization of rapidly solidified aluminium powders," *http://dx.doi.org/10.1179/mst.1987.3.12.1029*, vol. 3, no. 12, pp. 1029–1039, Jan. 2013, doi: 10.1179/MST.1987.3.12.1029.

[21] G. Antipas, "Gas atomization of aluminium melts: Comparison of analytical models," *Metals (Basel)*, vol. 2, no. 2, pp. 202–210, Jun. 2012, doi: 10.3390/met2020202.

[22] K. L. Alvarez *et al.*, "Novel Fe-based amorphous and nanocrystalline powder cores for high-frequency power conversion," *J Magn Magn Mater*, vol. 501, p. 166457, May 2020, doi: 10.1016/J.JMMM.2020.166457.

[23] X. gang Li, Q. Zhu, S. Shu, J. zhong Fan, and S. ming Zhang, "Fine spherical powder production during gas atomization of pressurized melts through melt nozzles with a small inner diameter," *Powder Technol*, vol. 356, pp. 759–768, Nov. 2019, doi: 10.1016/J.POWTEC.2019.09.023.

[24] R. German, *Powder metallurgy and particulate materials processing : the processes, materials, products, properties and applications*. Princeton New Jersey: Metal Powder Industries Federation, 2005. Accessed: Apr. 27, 2022. [Online]. Available: https://books.google.co.in/books?id=04CnAQAACAAJ

[25] J. Ting, M. W. Peretti, and W. B. Eisen, "The effect of wake-closure phenomenon on gas atomization performance," *Materials Science and Engineering A*, vol. 326, no. 1, pp. 110–121, Mar. 2002, doi: 10.1016/S0921-5093(01)01437-X.

[26] R. S. Miller, S. A. Miller, S. D. Savkar, and D. P. Mourer, "Two phase flow model for the close-coupled atomization of metals," *International Journal of*

Powder Metallurgy (Princeton, New Jersey), vol. 32, no. 4, pp. 341–352, Oct. 1996, doi: 10.1016/S0026-0657(97)86668-4.

[27] U. Fritsching and V. Uhlenwinkel, "Hybrid Gas Atomization for Powder Production," in *Powder Metallurgy*, InTech, 2012. doi: 10.5772/35807.

[28] I. E. Anderson, E. M. H. White, and R. Dehoff, "Feedstock powder processing research needs for additive manufacturing development," *Current Opinion in Solid State and Materials Science*, vol. 22, no. 1. Elsevier Ltd, pp. 8–15, Feb. 01, 2018. doi: 10.1016/j.cossms.2018.01.002.

[29] F. Persson, C. N. Hulme, and P. G. Jönsson, "Particle morphology of water atomised iron-carbon powders," *Powder Technol*, vol. 397, Jan. 2022, doi: 10.1016/j.powtec.2021.11.037.

[30] M. Abdelwahed, R. Casati, S. Bengtsson, A. Larsson, M. Riccio, and M. Vedani, "metals Effects of Powder Atomisation on Microstructural and Mechanical Behaviour of L-PBF Processed Steels", doi: 10.3390/met10111474.

[31] R. Li, Y. Shi, Z. Wang, L. Wang, J. Liu, and W. Jiang, "Densification behavior of gas and water atomized 316L stainless steel powder during selective laser melting," *Appl Surf Sci*, vol. 256, no. 13, pp. 4350–4356, Apr. 2010, doi: 10.1016/j.apsusc.2010.02.030.

[32] A. Asgarian, C.-T. Wu, D. Li, and M. Bussmann, "Experimental and Computational Analysis of a Water Spray; Application to Molten Metal Atomization Understanding gas/liquid/solid interaction in tundish metallurgy View project Multiphase Flows andPopulation Balance of Particles View project," 2018. [Online]. Available: https://www.researchgate.net/publication/331346212

[33] H. Zhang *et al.*, "Effects of annealing on high velocity compaction behavior and mechanical properties of iron-base PM alloy," *Powder Technol*, vol. 288, pp. 435–440, Jan. 2016, doi: 10.1016/j.powtec.2015.10.040.

[34] "AP&C Powder Metallurgy | GE Additive." https://www.advancedpowders.com/ (accessed Apr. 24, 2022).

[35] C. F. Yolton and F. H. (Sam, "Conventional titanium powder produc-tion."

[36] V. Sufiiarov, I. Polozov, and E. Borisov, “Additive manufacturing of individual implants from titanium alloy View project Additive manufacturing View project,” 2016. [Online]. Available: https://www.researchgate.net/publication/313467063

[37] D.-G. Ahn, “Directed Energy Deposition (DED) Process: State of the Art,” *International Journal of Precision Engineering and Manufacturing-Green Technology*, vol. 8, pp. 703–742, 123AD, doi: 10.1007/s40684-020-00302-7.

[38] K. A. Lorenz, J. B. Jones, D. I. Wimpenny, and M. R. Jackson, “A REVIEW OF HYBRID MANUFACTURING.”

[39] B. Vayre, F. Vignat, and F. Villeneuve, “Metallic additive manufacturing: State-of-the-art review and prospects,” *Mechanics and Industry*, vol. 13, no. 2, pp. 89–96, 2012, doi: 10.1051/meca/2012003.

[40] Y. Mahmoodkhani *et al.*, “On the measurement of effective powder layer thickness in laser powder-bed fusion additive manufacturing of metals,” *Progress in Additive Manufacturing*, vol. 4, no. 2, pp. 109–116, Jun. 2019, doi: 10.1007/S40964-018-0064-0.

[41] G. M. Mladenov, E. Koleva, L. Koleva, and V. Dzharov, “State of the art of additive manufacturing by selective electron beam melting models View project NATIONAL PROGRAM ‘YOUNG SCIENTISTS AND POSTDOCTRANTS’ View project,” 2016. [Online]. Available: https://www.researchgate.net/publication/307580909

[42] F. I. Azam, A. M. Abdul Rani, K. Altaf, T. V. V. L. N. Rao, and H. A. Zaharin, “An In-Depth Review on Direct Additive Manufacturing of Metals,” in *IOP Conference Series: Materials Science and Engineering*, Mar. 2018, vol. 328, no. 1. doi: 10.1088/1757-899X/328/1/012005.

[43] J. Milberg and M. Sigl, “Electron beam sintering of metal powder,” *Production Engineering*, vol. 2, no. 2, pp. 117–122, Jun. 2008, doi: 10.1007/S11740-008-0088-2.

[44] P. K. Gokuldoss, S. Kolla, J. Eckert, and J. Stampfl, “materials Additive Manufacturing Processes: Selective Laser Melting, Electron Beam Melting and Binder Jetting-Selection Guidelines,” 2017, doi: 10.3390/ma10060672.

[45] "Laser Powder Bed Fusion: tutto quello che c'è da sapere – 3Dnatives." https://www.3dnatives.com/it/laser-powder-bed-fusion-lpbf-050920219/ (accessed May 01, 2022).

[46] R. Verma and G. Kaushal, "State of the art of powder bed fusion additive manufacturing: A review," in *3D Printing and Additive Manufacturing Technologies*, Springer Singapore, 2018, pp. 269–279. doi: 10.1007/978-981-13-0305-0_23.

[47] E. Santecchia, S. Spigarelli, and M. Cabibbo, "Material reuse in laser powder bed fusion: Side effects of the laser—metal powder interaction," *Metals*, vol. 10, no. 3. MDPI AG, Mar. 01, 2020. doi: 10.3390/met10030341.

[48] C. Yan, L. Hao, A. Hussein, P. Young, J. Huang, and W. Zhu, "Microstructure and mechanical properties of aluminium alloy cellular lattice structures manufactured by direct metal laser sintering," *Materials Science and Engineering A*, vol. 628, pp. 238–246, Mar. 2015, doi: 10.1016/j.msea.2015.01.063.

[49] A. M. Khorasani, I. Gibson, J. K. Veetil, and A. H. Ghasemi, "A review of technological improvements in laser-based powder bed fusion of metal printers," *International Journal of Advanced Manufacturing Technology*, vol. 108, no. 1–2, pp. 191–209, May 2020, doi: 10.1007/s00170-020-05361-3.

[50] Y. Al-Meslemi, N. Anwer, and L. Mathieu, "Environmental Performance and Key Characteristics in Additive Manufacturing: A Literature Review," *Procedia CIRP*, vol. 69, pp. 148–153, 2018, doi: 10.1016/J.PROCIR.2017.11.141.

[51] H. Wong, D. Neary, E. Jones, P. Fox, and C. Sutcliffe, "Pilot capability evaluation of a feedback electronic imaging system prototype for in-process monitoring in electron beam additive manufacturing," *International Journal of Advanced Manufacturing Technology*, vol. 100, no. 1–4, pp. 707–720, Jan. 2019, doi: 10.1007/S00170-018-2702-6.

[52] M. Mani *et al.*, "Measurement Science Needs for Real-time Control of Additive Manufacturing Powder Bed Fusion Processes," 2015, doi: 10.6028/NIST.IR.8036.

[53] T. G. Spears and S. A. Gold, “In-process sensing in selective laser melting (SLM) additive manufacturing,” *Integrating Materials and Manufacturing Innovation*, vol. 5, no. 1. Springer Science and Business Media Deutschland GmbH, pp. 16–40, Dec. 01, 2016. doi: 10.1186/s40192-016-0045-4.

[54] T. Kurzynowski, E. Chlebus, B. Kuźnicka, and J. Reiner, “Parameters in selective laser melting for processing metallic powders,” *https://doi.org/10.1117/12.907292*, vol. 8239, pp. 317–322, Feb. 2012, doi: 10.1117/12.907292.

[55] M. Agarwala, D. Bourell, J. Beaman, H. Marcus, and J. Barlow, “Direct selective laser sintering of metals,” *Rapid Prototyp J*, vol. 1, no. 1, pp. 26–36, 1995, doi: 10.1108/13552549510078113/FULL/PDF.

[56] W. M. Steen and J. Mazumder, “Laser material processing: Fourth edition,” *Laser Material Processing: Fourth Edition*, pp. 1–558, 2010, doi: 10.1007/978-1-84996-062-5.

[57] P. Fischer, V. Romano, H. P. Weber, N. P. Karapatis, E. Boillat, and R. Glardon, “Sintering of commercially pure titanium powder with a Nd:YAG laser source,” *Acta Mater*, vol. 51, pp. 1651–1662, 2003, doi: 10.1016/S1359-6454(02)00567-0.

[58] H. Jia, H. Sun, H. Wang, Y. Wu, and H. Wang, “Scanning strategy in selective laser melting (SLM): a review”, doi: 10.1007/s00170-021-06810-3/Published.

[59] F. Trevisan *et al.*, “materials On the Selective Laser Melting (SLM) of the AlSi10Mg Alloy: Process, Microstructure, and Mechanical Properties”, doi: 10.3390/ma10010076.

[60] A. Huxol and F. J. Villmer, “DoE Methods for Parameter Evaluation in Selective Laser Melting,” *IFAC-PapersOnLine*, vol. 52, no. 10, pp. 270–275, Jan. 2019, doi: 10.1016/J.IFACOL.2019.10.041.

[61] P. Wei *et al.*, “The AlSi10Mg samples produced by selective laser melting: single track, densification, microstructure and mechanical behavior,” *Appl Surf Sci*, vol. 408, pp. 38–50, Jun. 2017, doi: 10.1016/J.APSUSC.2017.02.215.

[62] I. Yadroitsev, A. Gusarov, I. Yadroitsava, and I. Smurov, “Single track formation in selective laser melting of metal powders,” *J Mater Process Technol*, vol. 210, no. 12, pp. 1624–1631, 2010, doi: 10.1016/j.jmatprotec.2010.05.010.

[63] A. Aversa *et al.*, “Single scan track analyses on aluminium based powders,” *J Mater Process Technol*, vol. 255, no. December 2017, pp. 17–25, 2018, doi: 10.1016/j.jmatprotec.2017.11.055.

[64] T. H. C. Childs, C. Hauser, and M. Badrossamay, “Mapping and modelling single scan track formation in direct metal selective laser melting,” *CIRP Ann Manuf Technol*, vol. 53, no. 1, pp. 191–194, 2004, doi: 10.1016/S0007-8506(07)60676-3.

[65] S. K. Nayak, S. K. Mishra, C. P. Paul, A. N. Jinoop, and K. S. Bindra, “Effect of energy density on laser powder bed fusion built single tracks and thin wall structures with 100 μm preplaced powder layer thickness,” *Opt Laser Technol*, vol. 125, no. December 2019, p. 106016, 2020, doi: 10.1016/j.optlastec.2019.106016.

[66] F. Bosio *et al.*, “A time-saving and cost-effective method to process alloys by Laser Powder Bed Fusion,” *Mater Des*, vol. 181, p. 107949, 2019, doi: 10.1016/j.matdes.2019.107949.

[67] C. Tore and V. Lindström, “Defect formation and mitigation during laser powder bed fusion of copper.”

[68] C. Zhao *et al.*, “Real-time monitoring of laser powder bed fusion process using high-speed X-ray imaging and diffraction OPEN”, doi: 10.1038/s41598-017-03761-2.

[69] D. Basu, Z. Wu, J. L. L. Meyer, E. Larson, R. Kuo, and A. Rollett, “Entrapped Gas and Process Parameter-Induced Porosity Formation in Additively Manufactured 17-4 PH Stainless Steel”, doi: 10.1007/s11665-021-05695-3.

[70] M. Tang, P. C. Pistorius, and J. L. Beuth, “Prediction of lack-of-fusion porosity for powder bed fusion,” *Addit Manuf*, vol. 14, pp. 39–48, Mar. 2017, doi: 10.1016/J.ADDMA.2016.12.001.

[71] W. Stopyra, K. Gruber, I. Smolina, T. Kurzynowski, and B. Kuźnicka, "Laser powder bed fusion of AA7075 alloy: Influence of process parameters on porosity and hot cracking," *Addit Manuf*, vol. 35, Oct. 2020, doi: 10.1016/J.ADDMA.2020.101270.

[72] H. KYOGOKU and T.-T. IKESHOJI, "A review of metal additive manufacturing technologies: Mechanism of defects formation and simulation of melting and solidification phenomena in laser powder bed fusion process," *Mechanical Engineering Reviews*, vol. 7, no. 1, pp. 19-00182-19–00182, 2020, doi: 10.1299/mer.19-00182.

[73] "UC Santa Barbara UC Santa Barbara Electronic Theses and Dissertations Title A Methodology and Analysis of Inoculation in Additive Aluminum Alloys." [Online]. Available: https://escholarship.org/uc/item/6fg8s2p7

[74] A. Nickel, D. Barnett, G. Link, and F. Prinz, "Residual Stresses in Layered ·Manufacturing".

[75] P. Mercelis and J.-P. Kruth, "Residual stresses in selective laser sintering and selective laser melting", doi: 10.1108/13552540610707013.

[76] M. T. Andani, R. Dehghani, M. Reza Karamooz-Ravari, R. Mirzaeifar, and J. Ni, "A study on the effect of energy input on spatter particles creation during selective laser melting process," *Addit Manuf*, vol. 20, pp. 33–43, 2018, doi: 10.1016/j.addma.2017.12.009.

[77] J. Zhang, B. Song, Q. Wei, D. Bourell, and Y. Shi, "Invited Review A review of selective laser melting of aluminum alloys: Processing, microstructure, property and developing trends," *J Mater Sci Technol*, vol. 35, pp. 270–284, 2019, doi: 10.1016/j.jmst.2018.09.004.

[78] J. C. Williams and E. A. Starke, "Progress in structural materials for aerospace systems," *Acta Mater*, vol. 51, no. 19, pp. 5775–5799, Nov. 2003, doi: 10.1016/J.ACTAMAT.2003.08.023.

[79] S. Fu *et al.*, "Influence of electric field on the quenched-in vacancy and solute clustering during early stage ageing of Al-Cu alloy," *J Mater Sci Technol*, vol. 34, no. 2, pp. 335–343, Feb. 2018, doi: 10.1016/J.JMST.2017.07.020.

[80] L. He, J. Kang, T. Huang, and K. Rong, “The integrated technique for the heat treatment of aluminium-alloy castings: A review,” *Heat Treatment of Metals*, vol. 31, no. 3, pp. 69–72, 2004.

[81] W. Li, K. Yang, S. Yin, X. Yang, Y. Xu, and R. Lupoi, “Solid-state additive manufacturing and repairing by cold spraying: A review,” *J Mater Sci Technol*, vol. 34, no. 3, pp. 440–457, Mar. 2018, doi: 10.1016/J.JMST.2017.09.015.

[82] E. O. Olakanmi, R. F. Cochrane, and K. W. Dalgarno, “A review on selective laser sintering/melting (SLS/SLM) of aluminium alloy powders: Processing, microstructure, and properties,” *Prog Mater Sci*, vol. 74, pp. 401–477, Oct. 2015, doi: 10.1016/J.PMATSCI.2015.03.002.

[83] E. Louvis, P. Fox, and C. J. Sutcliffe, “Selective laser melting of aluminium components,” *J Mater Process Technol*, vol. 211, no. 2, pp. 275–284, Feb. 2011, doi: 10.1016/J.JMATPROTEC.2010.09.019.

[84] Q. Miao *et al.*, “Comparative study of microstructure evaluation and mechanical properties of 4043 aluminum alloy fabricated by wire-based additive manufacturing,” *Mater Des*, vol. 186, Jan. 2020, doi: 10.1016/J.MATDES.2019.108205.

[85] K. Ishfaq, M. Abdullah, and M. A. Mahmood, “A state-of-the-art direct metal laser sintering of Ti6Al4V and AlSi10Mg alloys: Surface roughness, tensile strength, fatigue strength and microstructure,” *Opt Laser Technol*, vol. 143, p. 107366, 2021, doi: 10.1016/j.optlastec.2021.107366.

[86] S. Marola *et al.*, “A comparison of Selective Laser Melting with bulk rapid solidification of AlSi10Mg alloy,” *J Alloys Compd*, vol. 742, pp. 271–279, 2018, doi: 10.1016/j.jallcom.2018.01.309.

[87] “Characterization of spherical AlSi10Mg powder produced by double-nozzle gas atomization using different parameters _ Elsevier Enhanced Reader”.

[88] “Fine spherical powder production during gas atomization of pressurized melts through melt nozzles with a small inner diameter _ Elsevier Enhanced Reader”.

[89] W. bin Im, S. J. Park, Y. C. Yun, and B. C. Kim, “Manufacture of AlSi10Mg Alloy Powder for Powder Bed Fusion(PBF) Process using Gas Atomization Method,” *Journal of Korean Powder Metallurgy Institute*, vol. 28, no. 2, pp. 120–126, Apr. 2021, doi: 10.4150/KPMI.2021.28.2.120.

[90] I. Rosenthal, A. Stern, and N. Frage, “Microstructure and Mechanical Properties of AlSi10Mg Parts Produced by the Laser Beam Additive Manufacturing (AM) Technology”, doi: 10.1007/s13632-014-0168-y.

[91] F. Farrokhi, “Hybrid Laser Welding of Large Steel Structures: An Experimental and Numerical Study.” [Online]. Available: https://www.researchgate.net/publication/325895870

[92] N. T. Aboulkhair, C. Tuck, I. Ashcroft, I. Maskery, and N. M. Everitt, “On the Precipitation Hardening of Selective Laser Melted AlSi10Mg,” *Metall Mater Trans A Phys Metall Mater Sci*, vol. 46, no. 8, pp. 3337–3341, Aug. 2015, doi: 10.1007/S11661-015-2980-7/TABLES/1.

[93] E. A. Jägle *et al.*, “Precipitation Reactions in Age-Hardenable Alloys During Laser Additive Manufacturing,” *JOM*, vol. 68, no. 3, pp. 943–949, Mar. 2016, doi: 10.1007/S11837-015-1764-2/FIGURES/5.

[94] L. Girelli, M. Tocci, M. Gelfi, and A. Pola, “Study of heat treatment parameters for additively manufactured AlSi10Mg in comparison with corresponding cast alloy,” 2018, doi: 10.1016/j.msea.2018.10.026.

[95] N. Takata, H. Kodaira, K. Sekizawa, A. Suzuki, and M. Kobashi, “Change in Microstructure of Selectively Laser Melted AlSi10Mg Alloy with Heat Treatments.”

[96] W. Li *et al.*, “Effect of heat treatment on AlSi10Mg alloy fabricated by selective laser melting: Microstructure evolution, mechanical properties and fracture mechanism,” *Materials Science and Engineering A*, vol. 663, pp. 116–125, Apr. 2016, doi: 10.1016/J.MSEA.2016.03.088.

[97] P. Ma, Y. Jia, K. G. Prashanth, S. Scudino, Z. Yu, and J. Eckert, “Microstructure and phase formation in Al–20Si–5Fe–3Cu–1Mg synthesized by selective laser melting,” *J Alloys Compd*, vol. 657, pp. 430–435, Feb. 2016, doi: 10.1016/J.JALLCOM.2015.10.119.

[98] T. H. Lee and S. J. Hong, “Microstructure and mechanical properties of Al–Si–X alloys fabricated by gas atomization and extrusion process,” *J Alloys Compd*, vol. 487, no. 1–2, pp. 218–224, Nov. 2009, doi: 10.1016/J.JALLCOM.2009.07.108.

[99] A. Aversa *et al.*, “New aluminum alloys specifically designed for laser powder bed fusion: A review,” *Materials*, vol. 12, no. 7, 2019, doi: 10.3390/ma12071007.

[100] L. Jiang, Z. Zhang, Y. Bai, S. Li, and W. Mao, “Study on Sc Microalloying and Strengthening Mechanism of Al-Mg Alloy,” *Crystals (Basel)*, vol. 12, no. 5, May 2022, doi: 10.3390/cryst12050673.

[101] A. B. Spierings, K. Dawson, P. J. Uggowitzer, and K. Wegener, “Influence of SLM scan-speed on microstructure, precipitation of Al3Sc particles and mechanical properties in Sc- and Zr-modified Al-Mg alloys,” *Mater Des*, vol. 140, pp. 134–143, Feb. 2018, doi: 10.1016/J.MATDES.2017.11.053.

[102] D. Gianoglio *et al.*, “Banded microstructures in rapidly solidified Al-3 wt% Er,” *Intermetallics (Barking)*, vol. 119, Apr. 2020, doi: 10.1016/j.intermet.2020.106724.

[103] Y. H. Cho, H. C. Lee, K. H. Oh, and A. K. Dahle, “Effect of strontium and phosphorus on eutectic Al-Si nucleation and formation of β-Al5FeSi in hypoeutectic Al-Si foundry alloys,” *Metall Mater Trans A Phys Metall Mater Sci*, vol. 39, no. 10, pp. 2435–2448, Oct. 2008, doi: 10.1007/S11661-008-9580-8/FIGURES/12.

[104] M. Timpel, N. Wanderka, G. S. Vinod Kumar, and J. Banhart, “Microstructural investigation of Sr-modified Al–15 wt%Si alloys in the range from micrometer to atomic scale,” *Ultramicroscopy*, vol. 111, no. 6, pp. 695–700, May 2011, doi: 10.1016/J.ULTRAMIC.2010.12.023.

[105] S. Haro-Rodríguez, R. E. Goytia-Reyes, D. K. Dwivedi, V. H. Baltazar-Hernández, H. Flores-Zúñiga, and M. J. Pérez-López, “On influence of Ti and Sr on microstructure, mechanical properties and quality index of cast eutectic Al–Si–Mg alloy,” *Mater Des*, vol. 32, no. 4, pp. 1865–1871, Apr. 2011, doi: 10.1016/J.MATDES.2010.12.012.

[106] Z. Zhang, J. Frenzel, K. Neuking, and G. Eggeler, “On the reaction between NiTi melts and crucible graphite during vacuum induction melting of NiTi shape memory alloys,” *Acta Mater*, vol. 53, no. 14, pp. 3971–3985, Aug. 2005, doi: 10.1016/J.ACTAMAT.2005.05.004.

[107] “Standard Guide for Characterizing Properties of Metal Powders Used for Additive Manufacturing Processes 1”, doi: 10.1520/F3049-14R21.

[108] “Standard Test Methods for Flow Rate of Metal Powders Using the Carney Funnel 1 2. Referenced Documents 2.1 ASTM Standards: 2 B213 Test Methods for Flow Rate of Metal Powders Using the Hall Flowmeter Funnel B215 Practices for Sampling Metal Powders B243 Terminology of Powder Metallurgy B855 Test Method for Volumetric Flow Rate of Metal Powders Using the Arnold Meter and Hall Flowmeter”, doi: 10.1520/B0964-16.

[109] “Standard Test Method for Tap Density of Metal Powders and Compounds 1”, doi: 10.1520/B0527-22.

[110] “Designation: E8/E8M − 21 Standard Test Methods for Tension Testing of Metallic Materials 1”, doi: 10.1520/E0008_E0008M-21.

[111] F. Marinucci, A. Aversa, D. Manfredi, M. Lombardi, and P. Fino, “Evaluation of a Laboratory-Scale Gas-Atomized AlSi10Mg Powder and a Commercial-Grade Counterpart for Laser Powder Bed Fusion Processing,” *Materials*, vol. 15, no. 21, p. 7565, Oct. 2022, doi: 10.3390/ma15217565.

[112] S. E. Brika, M. Letenneur, C. A. Dion, and V. Brailovski, “Influence of particle morphology and size distribution on the powder flowability and laser powder bed fusion manufacturability of Ti-6Al-4V alloy,” *Addit Manuf*, vol. 31, Jan. 2020, doi: 10.1016/J.ADDMA.2019.100929.

[113] H. G. Coe and S. Pasebani, “Use of bimodal particle size distribution in selective laser melting of 316L stainless steel,” *Journal of Manufacturing and Materials Processing*, vol. 4, no. 1, Mar. 2020, doi: 10.3390/jmmp4010008.

[114] Z. Cai, R. Wang, C. Zhang, C. Peng, L. Xie, and L. Wang, “Characterization of Rapidly Solidified Al-27 Si Hypereutectic Alloy: Effect of Solidification Condition”, doi: 10.1007/s11665-015-1386-4.

[115] A. Raza *et al.*, "Degradation of AlSi10Mg powder during laser based powder bed fusion processing," *Mater Des*, vol. 198, Jan. 2021, doi: 10.1016/j.matdes.2020.109358.

[116] C. L. A. Leung, S. Marussi, M. Towrie, R. C. Atwood, P. J. Withers, and P. D. Lee, "The effect of powder oxidation on defect formation in laser additive manufacturing," *Acta Mater*, vol. 166, pp. 294–305, Mar. 2019, doi: 10.1016/J.ACTAMAT.2018.12.027.

[117] A. Martucci *et al.*, "An automatic on top analysis of single scan tracks to evaluate the laser powder bed fusion building parameters," *Materials*, vol. 14, no. 18, Sep. 2021, doi: 10.3390/ma14185171.

[118] K. Kempen, L. Thijs, J. van Humbeeck, and J. P. Kruth, "Mechanical Properties of AlSi10Mg Produced by Selective Laser Melting," in *Physics Procedia*, 2012, vol. 39, pp. 439–446. doi: 10.1016/j.phpro.2012.10.059.

[119] B. Chen, Y. Yao, X. Song, C. Tan, L. Cao, and J. Feng, "Microstructure and mechanical properties of additive manufacturing AlSi10Mg alloy using direct metal deposition," *Ferroelectrics*, vol. 523, no. 1, pp. 153–166, Jan. 2018, doi: 10.1080/00150193.2018.1392147.

[120] P. Xing, B. Gao, Y. Zhuang, K. Liu, and G. Tu, "Effect of erbium on properties and microstructure of Al-Si eutectic alloy," *Journal of Rare Earths*, vol. 28, no. 6, pp. 927–930, 2010, doi: 10.1016/S1002-0721(09)60222-2.

[121] A. Iturrioz, E. Gil, M. M. Petite, F. Garciandia, A. M. Mancisidor, and M. San Sebastian, "Selective laser melting of AlSi10Mg alloy: influence of heat treatment condition on mechanical properties and microstructure," *Welding in the World*, vol. 62, no. 4, pp. 885–892, Jun. 2018, doi: 10.1007/S40194-018-0592-8/TABLES/5.

[122] J. Fiocchi, A. Tuissi, and C. A. Biffi, "Heat treatment of aluminium alloys produced by laser powder bed fusion: A review," *Materials and Design*, vol. 204. Elsevier Ltd, Jun. 01, 2021. doi: 10.1016/j.matdes.2021.109651.

[123] J. Fiocchi, A. Tuissi, P. Bassani, and C. A. Biffi, "Low temperature annealing dedicated to AlSi10Mg selective laser melting products," *J Alloys Compd*,

vol. 695, pp. 3402–3409, Feb. 2017, doi: 10.1016/J.JALLCOM.2016.12.019.

[124] B. B. Stunová, “Strontium As a Structure Modifier for Non-binary Al-Si Alloy,” vol. 52, no. 4, 2012, doi: 10.6890.2590.